United States Nuclear Regulatory Commission

*Protecting People and the Environment*

NUREG/CR-7014
PNNL-19026

# Processes, Properties, and Conditions Controlling In Situ Bioremediation of Uranium in Shallow, Alluvial Aquifers

Office of Nuclear Regulatory Research

United States Nuclear Regulatory Commission

*Protecting People and the Environment*

NUREG/CR-7014
PNNL-19026

# Processes, Properties, and Conditions Controlling In Situ Bioremediation of Uranium in Shallow, Alluvial Aquifers

Manuscript Completed: March 2010
Date Published: July 2010

Prepared by
S.B. Yabusaki, Y. Fang, S.R. Waichler, and P.E. Long

Pacific Northwest National Laboratory
902 Battelle Boulevard
Richland, WA 99352

M. Fuhrmann, NRC Project Manager

NRC Job Code N6648

Office of Nuclear Regulatory Research

Abstract

Uranium can be removed from groundwater by adding an electron donor to the subsurface that stimulates growth of native bacteria, generating conditions that result in precipitation of uranium. The long-term efficacy of this technology is unproven. Numerical modeling results for uranium bioremediation in a shallow, alluvial aquifer are provided to establish a broad framework for understanding processes associated with bioremediation of uranium and to bound conditions under which bioremediation could succeed in the long-term and conditions under which it is likely to fail. The models are benchmarked against experiments conducted at the Rifle, Colorado site. Sensitivity analysis of model parameters were conducted, examining: alternatives to the acetate electron donor (lactate and ethanol), oxygen and nitrate terminal electron acceptors, multiphase flow, density and gas entrapment processes, and hypothetical flood events. Sensitivity of simulated aqueous U(VI) concentrations to process model parameters suggest that groundwater flow rate, uranium bioreduction rate, and sulfate bioreduction parameters exert the most impact on bioremediation effectiveness. The simulated scenarios are used to assess potential performance issues for site conditions and other bioremediation approaches.

# Table of Contents

Contents……...v
List of Figures…….vii
List of Tables……...ix
Executive Summary…….xi
Acknowledgements…….xiii

1 Introduction ..... 1.1

1.1 Purpose and Background ..... 1.1
1.2 Key Results ..... 1.2
1.3 Report Scope ..... 1.4

2 Bioremediation Studies at the Old Rifle IFRC site ..... 2.1

2.1 Site Description ..... 2.1
*2.1.1 Site Conditions ..... 2.3*
2.2 Bioremediation at the Rifle IFRC site ..... 2.4
2.3 Reactive Transport Modeling Studies ..... 2.6
*2.3.1 Biologically Mediated Reactions, Yabusaki et al. (2007) ..... 2.6*
*2.3.2 Abiotic Reaction Processes, Fang et al. (2009) ..... 2.7*
2.4 Conceptual Process Model ..... 2.9

3 Model Specification ..... 3.1

3.1 Hydrologic Model ..... 3.1
*3.1.1 Gas Entrapment ..... 3.4*
*3.1.2 Transport ..... 3.4*
*3.1.3 Solution Procedure ..... 3.5*
*3.1.4 Hydrologic Modeling Parameters ..... 3.6*
3.2 Biogeochemical Model ..... 3.7
*3.2.1 Biologically Mediated Reactions ..... 3.7*
*3.2.2 Abiotic Reactions ..... 3.9*
*3.2.3 Biogeochemical Model Calibration ..... 3.14*
3.3 Numerical Model Specification ..... 3.15
3.4 Sensitivity Analyses ..... 3.16
*3.4.1 Baseline ..... 3.17*
*3.4.2 Parameter Selection ..... 3.19*
*3.4.3 Hydrologic Model ..... 3.19*
*3.4.4 Biologically Mediated Reaction Model ..... 3.21*
*3.4.5 Geochemical Reaction Model ..... 3.23*

4 Modeling Scenarios ..... 4.1

4.1 Additional Electron Acceptors ..... 4.1
4.2 Additional Electron Donors ..... 4.3
4.3 Two-Dimensional Baseline ..... 4.6
*4.3.1 Hydrologic Conditions ..... 4.6*
*4.3.2 Injectate Density Effects ..... 4.13*
*4.3.3 Seasonal Water Table Fluctuation ..... 4.18*
*4.3.4 Flood Case Scenario ..... 4.23*

5 Summary and Conclusions ..... 5.1

5.1 One-Dimensional Reactive Transport ..... 5.2
*5.1.1 Sensitivity Analyses ..... 5.2*
*5.1.2 Terminal Electron Accepting Processes (TEAPs) ..... 5.3*

*5.1.3 Electron Donors* ..... *5.4*
5.2 Two-Dimensional Variably Saturated Flow and Reactive Transport ..... 5.5
*5.2.1 Injectate Density* ..... *5.5*
*5.2.2 Gas Entrapment* ..... *5.6*
*5.2.3 Flood Events* ..... *5.7*
5.3 Closing Comments and Next Steps for Reactive Transport Modeling of Uranium Bioremediation ..... 5.8
6 References ..... 6.1
Appendix A ..... A.1

# Table of Figures

**Figure 2.1**. Excavated exposure of subsurface above water table (left) and typical lithology (right) from Rifle Site. .....2.2

**Figure 2.2.** Rifle IFRC site with the location of the well layout (inset) for the 2007 Winchester / 2008 Big Rusty Experiments circled. .....2.3

**Figure 2.3.** Uranium aqueous speciation assuming Rifle groundwater chemistry. .....2.8

**Figure 3.1.** One-dimensional and two-dimensional modeling domains. Red vertical lines indicate upgradient (U-wells), injection gallery, and downgradient (D-wells) well locations. The one-dimensional model domain is 11.5 m long with the upgradient boundary at the injection gallery (X=28 m). Ponding at the ground surface for the flood scenario in the two-dimensional model domain is between X=20 and X=40 m. .....3.16

**Figure 3.2.** Simulated and observed acetate (left) and U(VI) (right) in monitoring well row 1 (2.5 m downgradient), row 2 (5.0 m downgradient), and row 3 (8.5 m downgradient).....3.18

**Figure 3.3.** Temporal aqueous Fe(II) (left) and sulfate (right) at 2.5m (top), 5.0m (center) and 8.5 m (bottom) downgradient from injection gallery.....3.18

**Figure 3.4.** Aqueous uranium sensitivity to flow rates 2.5 m (diamonds), 5.0 m (squares), and 8.5 m (triangles) downgradient from the injection gallery. .....3.20

**Figure 3.5.** Aqueous uranium sensitivity to porosity 2.5 m (diamonds), 5.0 m (squares), and 8.5 m (triangles) downgradient from the injection gallery. .....3.21

**Figure 3.6.** Aqueous uranium sensitivity to U(VI) bioreduction rate 2.5 m (diamonds), 5.0 m (squares), and 8.5 m (triangles) downgradient from the injection gallery. .....3.22

**Figure 3.7.** Aqueous uranium sensitivity to sulfate bioreduction rate 2.5 m (diamonds), 5.0 m (squares), and 8.5 m (triangles) downgradient from the injection gallery. .....3.22

**Figure 3.8.** Aqueous uranium sensitivity to pH 2.5 m (diamonds), 5.0 m (squares), and 8.5 m (triangles) downgradient from the injection gallery. .....3.23

**Figure 3.9.** Aqueous uranium sensitivity to site density for uranium surface complexation 2.5 m (diamonds), 5.0 m (squares), and 8.5 m (triangles) downgradient from the injection gallery.3.24

**Figure 3.10.** Aqueous uranium sensitivity to initial U(VI) concentration 2.5 m (diamonds), 5.0 m (squares), and 8.5 m (triangles) downgradient from the injection gallery. .....3.25

**Figure 4.1.** Dissolved oxygen (top) and aqueous U(VI) (bottom) during acetate biostimulation in downgradient monitoring row 1 (2.5 m), row 2 (5.0 m), and row 3 (8.5 m). .....4.2

**Figure 4.2.** Nitrate (top) and U(VI) (bottom) during acetate biostimulation in downgradient monitoring row 1 (2.5 m), row 2 (5.0 m), and row 3 (8.5 m). .....4.3

**Figure 4.3.** Lactate electron donor simulation: lactate (top) and U(VI) (bottom) concentrations in downgradient monitoring rows 1 (2.5 m), 2 (5.0 m), and 3 (8.5 m) .....4.5

**Figure 4.4.** Ethanol electron donor simulation: ethanol (top) and U(VI) (bottom) concentrations in downgradient monitoring rows 1 (2.5 m), 2 (5.0 m), and 3 (8.5 m). .....4.6

**Figure 4.5**. Rifle IFRC water table elevation during seasonal rise and fall. .....4.7

**Figure 4.6.** Comparison of simulated bromide concentrations with field observations in the downgradient monitoring well rows 2.5 m (D-02g and D-03), 5.0 m (D-06g and D-07), and 8.5 m (D-10g and D-11) downgradient from the injection gallery wells. The "g" designation for wells refers to the deepest sampling depth in the well. Note that soon after the increase in acetate concentrations on day 38 (see Table 3.10), uneven metering of amendment to the

injection wells and changes in the groundwater flow direction resulted in some of the bromide not being accounted for in the downgradient monitoring wells. .....4.8

**Figure 4.7.** Simulated spatial distributions of acetate 20, 30, 40, and 50 days after start of biostimulation. Note that the injection gallery is located at X=28 m and the last row of monitoring wells is at X=36.5 m. .....4.9

**Figure 4.8**. Simulated baseline aqueous U(VI) concentration distributions for day 20 to 100 of the biostimulation. .....4.10

**Figure 4.9.** Simulated baseline $UO_2$(s) concentration distributions for day 20 to 100 of the biostimulation. .....4.10

**Figure 4.10.** Simulated baseline aqueous Fe(II) concentration distributions for day 20 to 100 of the biostimulation. .....4.11

**Figure 4.11.** Simulated baseline aqueous sulfate concentration distributions for day 20 to 100 of the biostimulation. .....4.12

**Figure 4.12**. Simulated baseline FeS(s) concentration distributions for day 20 to 100 of the biostimulation. .....4.12

**Figure 4.13.** Acetate (top) and bromide (bottom) concentration as a function of depth on October 1, 2003. .....4.13

**Figure 4.14.** Density (top) and viscosity (bottom) variation with sodium acetate (blue) and sodium bromide (red) in solution.....4.14

**Figure 4.15.** Simulated 2003 field experiment illustrating the potential for acetate stratification.4.14

**Figure 4.16.** Cross-well mixing scheme with standard (left) and reversed (right) pumping directions. Two 2-channel peristaltic pumps are run throughout the period of injection with daily reversals. Cross-well mixing consists of two tubes, one to deep and one to shallow depths. .....4.15

**Figure 4.17.** Simulated acetate concentrations at 0 to 120 days after the initiation of biostimulation on July 20, 2008. Note that the injection gallery is located at X=28 m and the last row of monitoring wells is at X=36.5 m. .....4.16

**Figure 4.18.** Simulated variation of acetate concentrations with depth after 30 and 60 days of the baseline (corresponding to times with injection of 50 and 150 mM acetate, respectively), and after 60 days that included a hypothetical 300 mM acetate injection from day 38.....4.17

**Figure 4.19.** May 2002 to January 2004 Rifle water table elevation, U(VI) concentrations, and dissolved oxygen in upgradient wells B-01, B-02, and B-03. .....4.18

**Figure 4.20.** Simulated dissolved oxygen and aqueous saturation for six dates in 2008: April 15, June 3, July 17, September 11, November 9, and December 21. Note that the 2008 Big Rusty experimental plot lies between X=125 and X=140. .....4.19

**Figure 4.21.** Simulated dissolved oxygen after 10 days from the start of biostimulation.....4.20

**Figure 4.22.** Comparison of simulated acetate after 10 days of biostimulation for the baseline (top) and the gas entrapment case (bottom). .....4.20

**Figure 4.23.** Comparison of simulated aqueous U(VI) after 10 days of biostimulation for the baseline (top) and the gas entrapment case (bottom).....4.21

**Figure 4.24.** Comparison of simulated aqueous Fe(II) after 10 days of biostimulation for the baseline (top) and the gas entrapment case (bottom).....4.22

**Figure 4.25.** Simulated sulfate after 10 days of biostimulation with gas entrapment. .....4.22

**Figure 4.26.** Simulated aqueous saturations during the 7 day flood and 21 days following the flood. .....4.25

**Figure 4.27.** Simulated hydraulic head during the 7 day flood and subsequent 21 days. .....4.25

**Figure 4.28.** Simulated flood water tracer during the 7 day flood and the following 21 days. .....4.26

**Figure 4.29.** Simulated aqueous oxygen during the 7-day flood and the following 21 days. .....4.26

**Figure 4.30.** Comparison of baseline and flood scenario at day 5 for U(VI), acetate, $UO_2$(s), and aqueous sulfide. .....4.27

**Figure 4.31.** Comparison of injected tracer at 20, 30, 40, and 50 days after start of biostimulation for baseline (left) and flood scenario (right). .....4.28

**Figure 4.32.** Simulated dissolved oxygen concentrations at 20, 30, 40, 50, 60, 70, 80, and 100 days after initiation of acetate biostimulation. .....4.29

**Figure 4.33.** Comparison of simulated acetate concentrations at 20, 30, 40, and 50 days after start of biostimulation for baseline (left) and flood (right) scenarios. .....4.29

**Figure 4.34.** Comparison of simulated aqueous U(VI) concentrations at 20, 30, 40, and 50 days after start of biostimulation for baseline (left) and flood (right) scenarios. .....4.30

**Figure 4.35.** Comparison of simulated $UO_2$(s) concentrations at 20, 30, 40, and 50 days after start of biostimulation for baseline (left) and flood (right) scenarios. .....4.30

**Figure 4.36.** Comparison of simulated aqueous Fe(II) concentrations at 20, 30, 40, and 50 days after start of biostimulation for baseline (left) and flood (right) scenario. .....4.31

**Figure 4.37.** Comparison of simulated aqueous sulfate concentrations at 60, 70, 80, and 100 days after start of biostimulation for baseline (left) and flood (right) scenario. .....4.32

**Figure A.1**. Time-dependent aqueous uranium sensitivity to flow rate at 2.5 m (row 1), 5.0 m (row 2), and 8.5 m (row 3). .....A.1

**Figure A.2**. Time-dependent aqueous uranium sensitivity to porosity at 2.5 m (row 1), 5.0 m (row 2), and 8.5 m (row 3). .....A.1

**Figure A.3**. Time-dependent aqueous uranium sensitivity to dispersivity at 2.5 m (row 1), 5.0 m (row 2), and 8.5 m (row 3) .....A.2

**Figure A.4**. Time-dependent aqueous uranium sensitivity to initial SRB biomass at 2.5 m (row 1), 5.0 m (row 2), and 8.5 m (row 3). .....A.2

**Figure A.5**. Time-dependent aqueous uranium sensitivity to initial SRB biomass decay at 2.5 m (row 1), 5.0 m (row 2), and 8.5 m (row 3). .....A.3

**Figure A.6**. Time-dependent aqueous uranium sensitivity to uranium bioreduction rate at 2.5 m (row 1), 5.0 m (row 2), and 8.5 m (row 3). .....A.3

**Figure A.7**. Time-dependent aqueous uranium sensitivity to sulfate bioreduction rate at 2.5 m (row 1), 5.0 m (row 2), and 8.5 m (row 3). .....A.4

**Figure A.8**. Time-dependent aqueous uranium sensitivity to initial aqueous uranium concentration at 2.5 m (row 1), 5.0 m (row 2), and 8.5 m (row 3). .....A.4

**Figure A.9**. Time-dependent aqueous uranium sensitivity to uranium surface complexation site density at 2.5 m (row 1), 5.0 m (row 2), and 8.5 m (row 3). .....A.5

**Figure A.10**. Time-dependent aqueous uranium sensitivity to pH at 2.5 m (row 1), 5.0 m (row 2), and 8.5 m (row 3). .....A.5

# Tables

**Table 2.1.** Hydrologic parameters and water chemistry for the Rifle IFRC alluvial aquifer. .....2.4
**Table 3.1.** Parameters for hydrologic modeling and transport .....3.7
**Table 3.2**. U(VI) surface complexation reactions. .....3.10
**Table 3.3.** Uranium species and their formation constants. .....3.11
**Table 3.4.** $Fe^{2+}$ surface complexation reactions. .....3.11
**Table 3.5.** Modeled mineral reactions. .....3.12
**Table 3.6.** Equilibrium reactions in the reaction network. .....3.13
**Table 3.7.** Values for rate law parameters. .....3.14
**Table 3.8.** 2008 Big Rusty schedule of amendment concentrations. .....3.15
**Table 3.9.** Perturbation of model parameters for sensitivity analyses. .....3.19

# Processes, Properties and Conditions Controlling *In Situ* Bioremediation of Uranium in Shallow, Alluvial Aquifers

## *Executive Summary*

Proposed use of bioremediation for *in situ* treatment of uranium plumes in shallow alluvial aquifers drives the need to develop the understanding and the ability to assess such proposals and guide their implementation. To a large degree, the efficacy of uranium immobilization via engineered biostimulation will be site-specific. Hydrologic and biogeochemical processes, in the context of the site conditions and contaminant disposition, will control the uranium behavior. In this study, numerical modeling results for uranium bioremediation in a shallow, alluvial aquifer are provided to establish a broad framework for understanding processes associated with bioremediation of uranium and to bound conditions under which bioremediation could succeed in the long-term and conditions under which it is likely to fail.

The baseline process models and parameterizations are based on work conducted at the Rifle Integrated Field Research Challenge (IFRC) site, supported by the Climate and Environmental Sciences Division of the Office of Biological and Environmental Research at the U.S. Department of Energy Office of Science. At this former uranium mill tailings site, laboratory-supported field studies have demonstrated that indigenous dissimilatory metal-reducing bacteria, stimulated using acetate as an electron donor, can reduce soluble hexavalent uranium [U(VI)] to immobile solid-phase U(IV). This biologically mediated reduction of U(VI) can decrease concentrations of U(VI) in the shallow unconfined aquifer below relevant standards. Groundwater concentrations of U(VI) are lowest during the initial 30 to 40 days of biostimulation when iron reduction dominates. This is followed by a transition to dominantly sulfate-reducing conditions, which is accompanied by enrichment in sulfate-reducing bacteria and increasing concentrations of U(VI) in groundwater.

Observations from field biostimulation experiments have been successfully reproduced using numerical simulations of biogeochemical reactive transport based on the conceptual model that emerged from this research. The current study extends the Rifle IFRC modeling baseline to consider process model parameter sensitivity analyses; lactate and ethanol electron donors; oxygen and nitrate terminal electron acceptors; multiphase flow, density and gas entrapment processes; and hypothetical flood scenarios. These simulations are used to illustrate and develop insights for potential issues in the 1) site-specific characterization of processes, properties, and conditions controlling uranium behavior and 2) site-specific design of *in situ* uranium bioremediation.

Key results from field experiments and from modeling of uranium bioremediation in the shallow, alluvial aquifer are summarized with a focus on coupled process interactions. Sensitivity of the simulated aqueous U(VI) concentrations to process model parameters suggest that groundwater

flow rate, uranium bioreduction rate, and sulfate bioreduction parameters exert the most impact on bioremediation effectiveness. Flow rate affects the *in situ* concentration of injected amendments, the availability of reactants, and the transport of the electron donor and the aqueous reaction byproducts, which all play contributing roles in uranium bioremediation. The intrinsic uranium bioreduction rate has a direct impact on the magnitude of the aqueous uranium concentrations (i.e., higher intrinsic reaction rate results in higher uranium removal from groundwater). Once sulfate reducing bacteria begin to dominate the microbial community, higher sulfate bioreduction reaction rates lead to higher aqueous U(VI) concentrations. In this case, the increase in bicarbonate from acetate oxidation favors the formation of uranium-carbonate species with less affinity for the mineral surfaces.

Dissolved oxygen and nitrate are important oxidizers that can potentially degrade the performance of engineered bioremediation. To create redox conditions most conducive to uranium bioreduction and U(IV) stability, the simulations demonstrate that additional electron donor will be necessary to drive the terminal electron accepting processes (TEAPs) that will reduce/remove oxygen and nitrate in groundwater. The additional electron donor needed to achieve these conditions may be relatively small, but the TEAP kinetics needs to be characterized at a given site prior to full-scale deployment.

A key issue for uranium bioremediation is the stability of solid-phase reduction products, including U(IV). Stability must be ensured either by natural conditions in the aquifer similar to those observed at the Rifle IFRC or by maintaining reducing conditions through periodic injections of electron donors. The injection frequency will depend on site-specific conditions which must be carefully evaluated for successful application of this technology.

The modeling scenarios with lactate and ethanol identified how the stoichiometry of the TEAP reactions specific to these electron donors can result in increased consumption of electron donor and increased production of TEAP products. In cases where the amendment density is greater than the ambient groundwater density (e.g., for acetate, lactate), electron donor can potentially sink and accumulate near the aquifer bottom. This can be avoided with judicious design of electron donor concentrations and cross-well mixing.

Wetting events (e.g., seasonal water table rise, recharge, flooding) that result in the saturation of previously unsaturated pores can trap gas with near-atmospheric compositions, leading to enhanced dissolved oxygen in groundwater. The modeling results show that flooding by surface ponding can significantly disrupt the distribution of electron donor and increase dissolved oxygen deep in an aquifer. The potential for interfering with bioremediation progress and/or reoxidizing reduced uranium suggests careful evaluation of the risk presented by flood events.

Overall results from these numerical modeling studies illustrate their value for uranium bioremediation design and the importance of documenting site-specific processes and rates including disruptive events such as floods, before, during, and after bioremediation.

# Acknowledgments

The authors would like to acknowledge Mike Wilkins and Signe Wurstner for their helpful comments and suggestions in the development of this document. This document benefited significantly from the thorough and thoughtful review provided by Mark Fuhrmann, Joe Kanney, Wendy Reed and Tom Nicholson.

# 1 Introduction

## 1.1 Purpose and Background

Cleanup of uranium contamination in groundwater using bioremediation was first proposed in the early 1990's by Derek Lovley and coworkers (Lovley et al., 1991). Their approach, based on laboratory experiments, was to use catalysis of dissimilatory metal reduction by microorganisms to reduce the soluble U(VI) form of uranium to the relatively insoluble U(IV) form. The concept is that amendment of acetate electron donor *in situ* results in the reduction of aqueous U(VI) to sparingly-soluble U(IV), in the form of uraninite ($UO_2$) mineral. The uraninite becomes attached to solid surfaces in the aquifer sediments. Field experiments to test the efficacy of this process were not performed until 2002 (Anderson et al., 2003). Since those initial experiments, a significant amount of field-scale and lab-scale experimentation has been performed to investigate a broad range of processes associated with electron donor amendment and microbial U(VI) reduction (Vrionis et al., 2005; Wu et al., 2006).

Remediation practitioners noted results from these field studies (Anderson et al., 2003; Vrionis et al., 2005; Wu et al., 2006) and the potential cost savings for clients if uranium bioremediation could be successfully applied. This led to applications proposing its use to regulatory agencies, including the U.S. Nuclear Regulatory Commission (NRC). To address this situation, the NRC first identified the overall technical basis for assessing uranium bioremediation (Long et al., 2008), which included a description of controlling processes, design considerations, and performance indicators that should be a part of the monitoring and modeling approach.

Underlying this seemingly straightforward bioremediation principle is the knowledge that uranium exhibits a wide range of behavior that is sensitive to site-specific processes, properties and conditions. Aqueous complexation of uranium with major ions (e.g., calcium, bicarbonate) can significantly alter uranium affinity for mineral surfaces and availability for bioreduction (Brooks et al., 2003). These processes are in turn affected by the pH, carbonate chemistry including mineral reactions, and cation exchange processes. The biostimulation that accomplishes uranium bioreduction also introduces a dynamic component to the aforementioned behaviors: increases in pH, alkalinity, exchangeable cations, and highly reactive reduction products. Furthermore, the microbial community is also responding to the biostimulation and evolving in ways that may eventually impact the efficacy of uranium bioremediation. Mineral reactions induced by these changes can potentially provide a basis for long-term stabilization of uranium. This is important because the reduction of U(VI) is known to be reversible in laboratory experiments (Abdelouas et al., 1999; Komlos et al., 2008a; Komlos et al., 2008b; Moon et al., 2007; Moon et al., 2009; Sani et al., 2005; Senko et al., 2002), hence the oxidation of U(IV) could resolubilize uranium and possibly defeat the objective of bioremediation.

However, if bioremediation of uranium can be successfully deployed, it is extremely attractive because extraction methods such as pump and treat can require unacceptably long time periods (i.e., decades) to satisfy the 30 μg/L Maximum Concentration Limit for drinking water (EPA,

2000). Moreover, at many uranium-contaminated sites, groundwater concentrations of uranium are not naturally attenuating at rates predicted by modeling with constant uranium distribution coefficients, $K_d$s (Yabusaki et al., 2008). Long time frames for natural attenuation are also not acceptable in most regulatory situations and hence a method that would accelerate attenuation of uranium and maintain low groundwater concentrations in the long term would be welcome as long as it could be shown to be protective of the public health and safety.

In the present study, numerical modeling results for uranium bioremediation in a shallow, alluvial aquifer are provided to establish a broad framework for understanding processes associated with the bioremediation of uranium and to bound conditions under which bioremediation could succeed in the long-term and conditions under which it is likely to fail. The baseline process models and parameterizations are based on work conducted at the Rifle Integrated Field Research Challenge site, supported by the U.S. Department of Energy, Office of Science, Biological and Environmental Research (BER), Environmental Remediation Sciences Program (ERSP). This former Uranium Mill Tailings Remedial Action (UMTRA) site in Rifle, Colorado has proven to be a useful test bed for field-scale electron donor amendment experiments for examining bioremediation of uranium in alluvial aquifers. Both field and modeling studies have been conducted in this research program and experimental results have been successfully reproduced using reactive transport models (Fang et al., 2009; Yabusaki et al., 2007).

While the modeling presented here is based on a specific uranium-contaminated site, the current study goes beyond the baseline for that site to consider model parameter sensitivity analyses; alternatives to the acetate electron donor (lactate and ethanol); oxygen and nitrate terminal electron acceptors; multiphase flow, density and gas entrapment processes; and hypothetical flood events. The simulated scenarios are used to assess potential performance issues for other site conditions and other bioremediation approaches. This document thus provides regulators and practitioners with information to better address potential issues in 1) site-specific characterization of processes, properties, and conditions controlling uranium behavior and 2) site-specific design of *in situ* uranium bioremediation. Furthermore, performance predictions for proposed bioremediation can be compared against those obtained for this site. Since the hypothetical scenarios include processes, properties and conditions that have not actually been tested under field conditions, prescriptive application of the results presented here would be inappropriate. Instead, numerical model outcomes in this report are best used to assess the completeness of processes used to predict bioremediation outcomes and to assess the relative impacts of uncertainty in specific parameters.

## 1.2 Key Results

Key results from field experiments and from modeling of uranium bioremediation in an alluvial aquifer are as follows:

- If bioremediation is designed to treat uranium transported via groundwater flow, the system must be able to immobilize uranium at a rate greater than or equal to the influx of uranium for its design life or until upgradient uranium is sufficiently depleted. Otherwise, concentrations of uranium in the treatment zone will eventually rebound to upgradient levels. Evidence for significant abiotic uranium reduction in the field has yet to be observed at the Rifle Site. Consequently, continual or pulsed electron donor amendment, application of slow-release electron donor, and/or alternative immobilization approaches may be required.

- If an entire uranium plume is treated, continual electron donor amendment may not be as important. Instead, the rate of remobilization must be well understood. Under Rifle groundwater conditions, this rate may be low. Under more oxic conditions the remobilization rate is likely to be higher, although direct measurement of such rates under aquifer conditions are only now becoming available.

- Biostimulation can significantly alter the local biogeochemistry in ways that affect the near-term and long-term abiotic controls on uranium behavior. In particular, increases in Fe(II), sulfide, and bicarbonate lead to solid-phase reactions that affect uranium surface complexation, uranium co-precipitation, and availability of electron donors for additional bioreduction.

- In this study, parameter sensitivity analyses with our numerical process models suggest that groundwater flow rate, uranium bioreduction rate, and sulfate bioreduction parameters exert the most impact on bioremediation effectiveness. Additional numerical experiments are warranted to determine how these parameters interact and if the same conclusions would be derived from more extreme ranges of properties.

- The presence of oxygen and nitrate can complicate uranium bioremediation. They are both oxidants with respect to the Fe(II), U(IV), and sulfide bioreduction products associated with uranium bioremediation. In particular, the nitrite intermediate product in the nitrate terminal electron accepting process (TEAP) is a strong oxidant (Moon et al., 2009), and must also be addressed for U(VI) bioreduction to be effective. Consequently, additional electron donor will be necessary to drive the TEAPs for oxygen, nitrate, and nitrite reduction/removal from groundwater to establish redox conditions most conducive to uranium bioreduction and U(IV) stability. The additional electron donor needed to achieve these conditions may be relatively small, but the TEAP kinetics needs to be characterized prior to full-scale deployment of a bioremediation design.

- Lactate and ethanol are possible electron donors for uranium bioremediation (Shelobolina et al., 2008). In both cases, acetate is an intermediate oxidation byproduct of the TEAP reactions. This allows retention of the existing acetate oxidizing TEAP reactions and rate laws, supplemented with the necessary lactate and ethanol reactions to model the required sequence of reactions. In this study, the simulated results for ethanol and lactate are very

similar but, in comparison to the acetate baseline, there is considerably more electron donor consumption. The TEAP reactions specific to these electron donors also result in increased production of TEAP products (e.g., bicarbonate).

- In cases where the amendment density is greater than the ambient groundwater density, there is potential for the delivery and mixing of the electron donor in the aquifer to be adversely impacted. Acetate and lactate are denser than groundwater, which can lead to higher concentrations of electron donor near the base of the aquifer. It was shown that the electron donor concentrations and cross-well mixing of amendments with groundwater are important considerations in the bioremediation design. Density impacts are minimized with increases in mixing, groundwater velocity, subsurface heterogeneity, and anisotropy.

- In this study, it was shown that wetting events (e.g., seasonal water table rise, recharge) that saturate previously unsaturated pores may trap gas with atmospheric levels of oxygen. The oxygen gas can partition to the aqueous phase and diffuse through the groundwater. The magnitude of enhanced oxygenation depends on sediment texture, vadose zone soil gas composition, and the magnitude, frequency, and duration of water table fluctuations. Concerns arising from elevated oxygen near the water table include 1) re-oxidation and remobilization of reduced uranium are possible, 2) treatment capacity may be lost precisely where elevated groundwater uranium concentrations are commonly found (i.e., near the water table), 3) key microorganisms during bioremediation are not very tolerant of high oxygen levels, and 4) additional electron donor will be needed to achieve anaerobic conditions.

- Because uranium-contaminated alluvial aquifers are commonly located on floodplains, the disruptive scenario studied was a one-week long flood. Hydrologic impacts can negatively impact amendment delivery and dissolved oxygen can be driven deep into alluvial aquifers at levels near saturation with atmospheric oxygen. The enhanced dissolved oxygen is an additional terminal electron acceptor that requires additional electron donor for removal. While the additional amendment required to remove dissolved oxygen is small compared to typical biostimulation concentrations, a post-biostimulation flood event could reoxidize and remobilize previously bioreduced uranium. Thus, it is important to document site-specific flood impacts, before, during, and after bioremediation.

## 1.3 Report Scope

The main body of this report begins with Section 2.0 Bioremediation Studies at the Old Rifle IFRC site, which describes the Rifle IFRC site hydrology, geochemistry, and contaminant history and summarizes previous modeling studies at the site. This section includes a description of the conceptual model for uranium bioremediation at the site. The hydrologic model and biogeochemical reaction network are then described in Section 3.0, Model Specification.

Included in this section is the description of the baseline specification of the modeled system including the sensitivity of aqueous uranium concentrations to physical, geochemical, and biological process model parameters. Section 4.0, Modeling Scenarios, begins with one-dimensional simulations that investigate the impact of additional electron acceptors and electron donors on bioremediation. The two-dimensional scenarios target the impacts of density-dependent behavior of the injected amendment, seasonal water table fluctuations, and flooding events. The narrative part of the report ends with Section 5.0, Summary and Conclusions, which discusses results from the modeling scenarios with implications for deployment and research needs. This section provides a synopsis of the report, highlighting implications of the modeling results for shallow alluvial sites under consideration for *in situ* uranium bioremediation.

# 2 Bioremediation Studies at the Old Rifle IFRC site

## 2.1 Site Description

The Old Rifle IFRC site is a former Uranium Mill Tailings Remedial Action (UMTRA) site in Rifle, Colorado on a flood plain of the Colorado River. The flood plain is 750 m in length along the river shore and 250 m at the widest point. The unconfined aquifer is contaminated by residual uranium leached from now-removed mill tailings (Anderson et al., 2003; Vrionis et al., 2005), which percolated through a 4 m thick vadose zone to the water table, where it was transported laterally through the aquifer via groundwater flow. The uranium migrates through the subsurface as hexavalent U(VI), exceeding the UMTRA regulatory standard of 44 μg/L (EPA, 1998) throughout the experimental site, with maximum concentrations ca. 300 μg/L. Groundwater moves primarily in the topmost hydrostratigraphic unit of the unconfined aquifer, a sandy-gravel, gravelly-sand alluvium with an average saturated thickness of 2.4 m in the vicinity of the experimental plot. Grain size for the gravels range from pebbles to cobbles (Wentworth scale). This permeable layer is underlain by a relatively impermeable silty shale from the weathered Wasatch formation (DOE, 1999). The alluvium is approximately 6 m thick, including 2 m of clay fill, with the average water table occurring at 4 m depth (Figure 2.1) The clay fill was installed after the mill tailings and contaminated soil were removed during cleanup operations under the UMTRA program.

The field plot for the current study was installed in 2007 in an untreated part of the Rifle IFRC site about 35 m southeast from the original 2002/2003 experimental field plot. The new plot comprises an injection gallery of 10 fully penetrating and screened wells, and 3 upgradient and 12 downgradient monitoring wells (Figure 2.2). The 12 downgradient monitoring wells were arranged in 3 rows, 2.5, 5.0, and 8.5 m from the injection gallery, oriented to capture transport along the predominant groundwater flow direction. Two of the upgradient wells, U-01 and U-02, were 4 m from the injection gallery, while the central upgradient well, U-03, was 8 m from the injection gallery. Despite seasonal water table dynamics that change the saturated thickness of the aquifer, the groundwater flows predominantly to the south-southwest toward the Colorado River. More detailed descriptions of the well network and injection system can be found in Fang et al. (2009) and more detailed descriptions of the site can be found in DOE (1999).

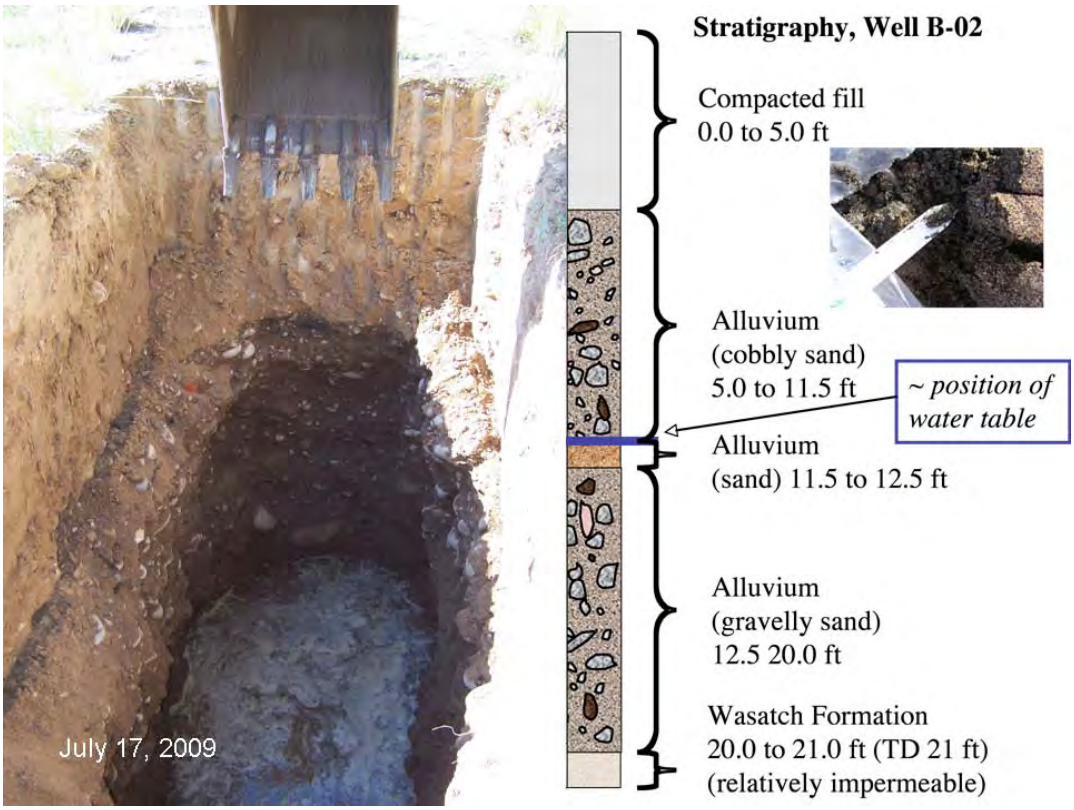


**Figure 2.1**. Excavated exposure of subsurface above water table (left) and typical lithology (right) from Rifle Site.

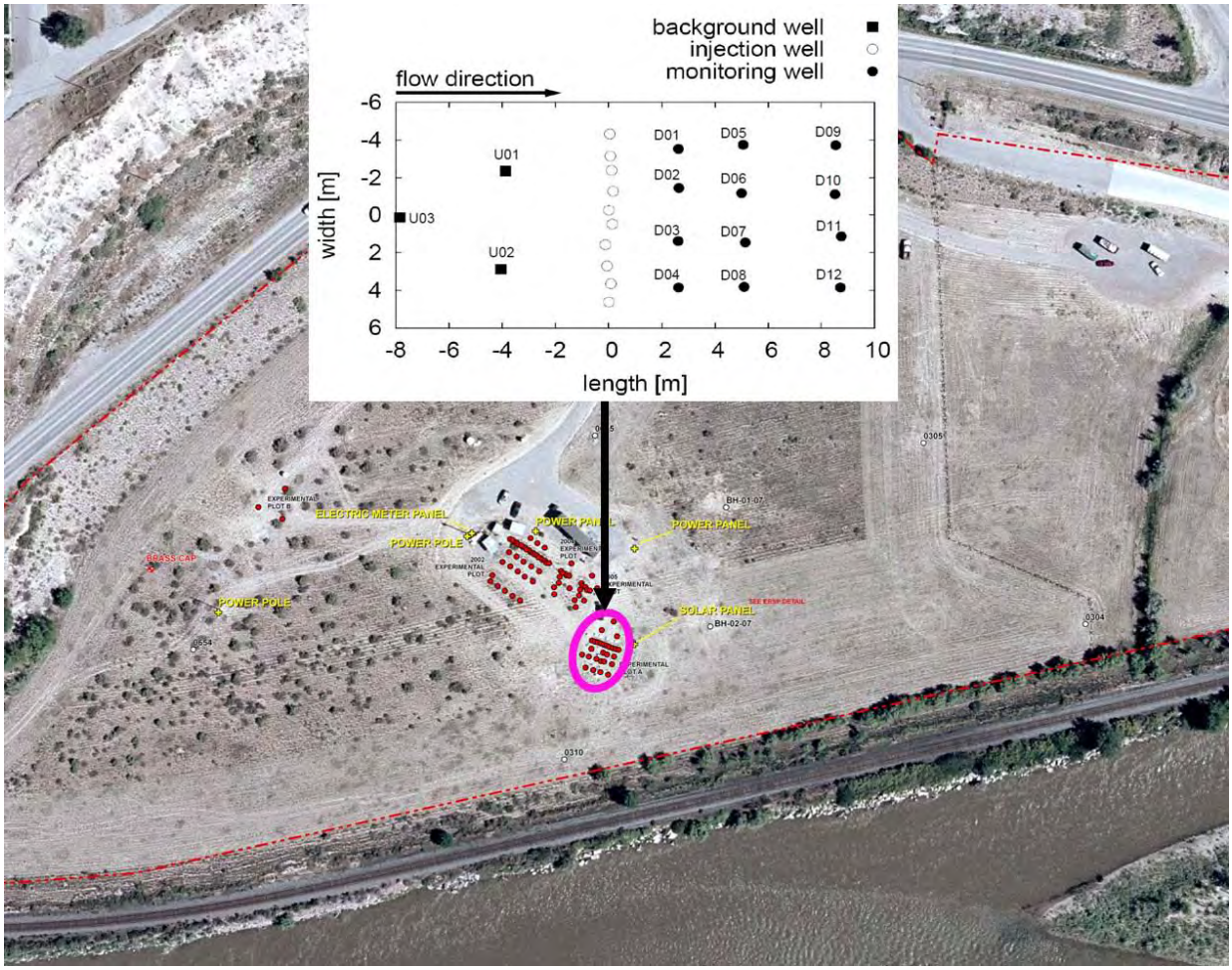


**Figure 2.2.** Rifle IFRC site with the location of the well layout (inset) for the 2007 Winchester / 2008 Big Rusty Experiments circled.

### 2.1.1 Site Conditions

This study began with the identification of a set of baseline process models and associated parameters from the current state of knowledge provided by the DOE ERSP Rifle IFRC project. In particular, we are using characterization data from the 2008 acetate biostimulation field experiment. Based on analyses of groundwater samples at the site, the aquifer is characterized by very low dissolved oxygen (<0.2 ppm), although higher measurements are observed near the water table and during elevated water table conditions in late spring. Nitrate concentrations are also very low (<0.2 ppm). The low nitrate concentrations are consistent with iron reducing conditions indicated by the presence of Fe(II) in solution and low Eh (<250 mV) at circumneutral pH. The parameters with observed ranges describing the hydrology and water chemistry at the site are summarized in Table 2.1.

**Table 2.1.** Hydrologic parameters and water chemistry for the Rifle IFRC alluvial aquifer.

| **Hydrologic Parameters** | |
|---|---|
| Saturated Thickness | 2.4 to 3.4 m |
| Hydraulic Conductivity | 5 to 20 m/d |
| Porosity | 0.15 to 0.35 |
| Pore Velocity | 0.3 to 0.5 m/d |
| **Water Chemistry** | |
| Uranium | ~0.7 – 1.5 μM |
| pH | ~7.0 – 7.2 |
| Alkalinity | ~7-10 meq/L |
| Eh | -150 to 240 mV |
| Dissolved Oxygen | 3 to 20 μM |
| Fe(II) | 15 to 50 μM |
| Nitrate | 2 to 3 μM |
| Sulfate | 8 to 11 mM |
| Sulfide | 0.03 to 0.5 μM |

## 2.2 Bioremediation at the Rifle IFRC site

In 2002, a series of uranium bioremediation field experiments began at the Old Rifle UMTRA site in Western Colorado (subsequently referred to as the Rifle IFRC site). The principle of direct enzymatic reduction of mobile hexavalent uranium [U(VI)] that these field experiments were based on was identified more than 10 years earlier by (Lovley et al., 1991) and Gorby and Lovley (1992) who suggested that dissimilatory metal-reducing bacteria grown with acetate as an electron donor could be used to immobilize U(VI) as precipitated U(IV) mineral. In particular, the 2002 and 2003 biostimulation field experiments, which were performed in the same field plot at the Rifle IFRC site (Anderson et al., 2003; Vrionis et al., 2005), demonstrated that U(VI) concentrations in the shallow unconfined aquifer could be lowered below relevant standards by stimulating indigenous dissimilatory metal reducing bacteria with acetate as the electron donor. The removal of U(VI) from solution was coincident with a decrease in Fe(III) minerals, an accumulation of aqueous Fe(II), and an enrichment of members of the *Geobacteraceae*, which led to the attribution of uranium bioreduction to iron-reducing *Geobacter* species. The greatest enrichment of members of the *Geobacteraceae* in sediments was correlated to the highest ratio of U(IV) to total uranium. This was followed by a sulfate-reducing phase characterized by the simultaneous observance of sulfide, depleted Fe(III), and 16S rDNA sequences most closely related to members of the *Desulfobacterales*. The transition to dominant sulfate-reducing conditions, as evidenced by a decrease in sulfate concentrations after 45 days of acetate amendment in 2002, was accompanied by a partial rebound in U(VI) groundwater concentrations (Anderson et al., 2003). The field observations, including downgradient sediment cores with elevated U(IV), were consistent with previous laboratory studies where 1) the stimulation of

acetate-oxidizing metal reducing bacteria (i.e., *Geobacter sp*.) concomitantly reduced and immobilized aqueous U(VI) (Finneran et al., 2002; Holmes et al., 2002), and 2) acetate-oxidizing sulfate reducing bacteria were not as effective at U(VI) immobilization (Lovley et al., 1993; Ortiz-Bernad et al., 2004).

In the summer of 2007, the "Winchester" field experiment was designed to test the feasibility of proteomic sampling and analysis during acetate biostimulation ofdissimilatory metal-reducers, without initiating significant sulfate reduction. A relatively short 31-day biostimulation experiment was designed to maintain iron-reducing conditions and test the impact of a 7-day interruption of continuous acetate injection on the response of the system biogeochemistry. The initial mixing of amendment between injection wells was controlled by continuous cross-well mixing using peristaltic pumps to transfer liquid between injection wells at three depths in each of the 10 gallery wells.

Biostimulation clearly alters solid phase mineralogy during field experiments at the Rifle site. It is the biologically mediated transfer of electrons to solid-phase Fe(III) that provides the energy for cell maintenance, activity, and growth in Fe(III)-reducing bacteria (FeRB). Fe(III) mineral sources are abundant in Rifle sediments and Fe does not appear to be limiting based on column experiments using Rifle sediments in which Fe reduction continued throughout an experiment that ran for more than 200 days (Komlos et al., 2008b). During sulfate reduction (typically the dominant process after about 30 to 40 days), a combination of calcite and iron sulfide are thought to be volumetrically the most important precipitates. Lesser amounts of elemental sulfur and siderite have also been observed in sediment from column experiments and from the subsurface, post-biostimulation sampling. Reduced uranium [U(IV)] also becomes part of the solid phase, most likely as a low abundance surface coating or decoration on existing grains. It may also be incorporated into calcite. Laboratory experiments with relatively high concentrations of uranium have produced both cell-associated and extra-cellular nanoparticulate uraninite (e.g., Suzuki et al. 2005). While it is attractive to assume this as the form of U(IV) in the subsurface during *in situ* bioremediation and this is the from used in the modeling results reported in this document, it is challenging to actually determine the solid phase chemistry of U(IV) in sediments retrieved from the subsurface at the Rifle site. This is because of the low uranium concentrations in Rifle sediments, which limit our ability to use spectroscopy or microscopy to analyze uranium phases or phases that incorporate uranium. This limitation is being addressed on Rifle sediments via column and *in situ* experiments. EXAFS and XANES obtained on such systems to date suggest that sorbed U(IV) may be more important than uraninite (Bargar et al., 2008). Factors governing the formation of sorbed U(IV) versus uraninite are not well understood and it is not known if sorbed U(IV) is cell-associated or adsorbed to mineral surfaces. Currently, rates of uraninite dissolution are being measured *in situ* at the Rifle site (Bargar et al., 2009a; Bargar et al., 2009b) and this work will likely be extended to include cell-associated U(IV) in the future.

## 2.3 Reactive Transport Modeling Studies

### 2.3.1 Biologically Mediated Reactions, Yabusaki et al. (2007)

A reactive transport modeling study by Yabusaki et al. (2007) analyzed data from the 2002 and 2003 field experiments and characterized the principal flow, transport and biological processes controlling uranium mobility during the experiments. Data from the 2002 field experiment were used to identify the dominant transport and biological processes controlling uranium mobility during biostimulation, and determine field-scale parameters for these modeled processes. Under the very low dissolved oxygen and nitrate conditions in the Rifle IFRC groundwater, the biostimulation was assumed to quickly proceed to iron reduction with negligible consumption of electron donor by the oxygen and nitrate TEAPs. Microbial community composition and function from Anderson et al. (2003) provided insight on the differentiation of the metabolic capability associated with specific community members related to uranium immobilization. A simple process model conceptualization with three TEAPs and two distinct immobile microbial populations was chosen to build an understanding of the dominant behaviors of the bulk system observed in the field at the Rifle IFRC site.

Acetate injection initially stimulates the growth of members of the *Geobacteraceae*, resulting in the reduction of Fe(III), concurrent with removal of U(VI) from groundwater. The second phase of the conceptual model of biologically mediated reactions is sulfate-reduction. In this case, the TEAP reaction for sulfate reduction was associated with immobile sulfate-reducing organisms. The stoichiometry in these irreversible reactions, which include the yield of an immobile biomass, are energetics-based (Rittmann and McCarty, 2001) under the assumption of a biomass molecular formula of $C_5H_7O_2N$ and an energy-transfer efficiency value of 0.6. In these three TEAP reactions, the biomass is nominally attributed to iron-reducing microbial communities that are known to be dominated by *Geobacter* spp. Goethite, one of the iron oxides identified at the site by Mössbauer spectroscopy (Komlos et al., 2008b), was used as an Fe(III) oxide terminal electron acceptor. Uranyl was used as the terminal electron acceptor in the uranium reduction reaction, while the ammonium ion, $NH_4^+$ was considered to be non-limiting. The coupled process simulation approach was able to establish a quantitative characterization of the principal flow, transport, and reaction processes based on the 2002 field experiment that could be applied without modification to describe the 2003 field experiment.

The decline of acetate concentrations coincided with the onset of sulfate reduction as evidenced by the concomitant decrease in sulfate concentrations and detection of sulfide. The eventual depletion of acetate occurs due to several factors: 1) in the postulated reaction stoichiometry, one mole of acetate reacts with 0.924 moles of sulfate [versus 4.8 moles of Fe(III) and 6.2 moles of U(VI) in the iron and uranium TEAPs, respectively], 2) sulfate concentrations are approximately three times the initial acetate concentrations in the groundwater, and 3) the sulfate bioreduction rate is relatively rapid. This results in an acetate-limited sulfate bioreduction reaction that significantly contributes to the nearly complete consumption of acetate toward the end of the biostimulation period.

Vrionis et al. (2005) provided geochemical evidence suggesting that Fe(III), U(VI), and sulfate reduction could simultaneously occur during acetate biostimulation in the field. This observation was bolstered by the presence of members of both the *Geobacteraceae* and *Desulfobacterales* in the associated sediment sample. Accordingly, a rate law was developed for the Fe(III) TEAP that allowed the activity of FeRB to continue after the onset of sulfate reduction. In this case, the rise in aqueous U(VI) observed during sulfate reduction was attributed to the lower activity of FeRB competing with sulfate-reducing bacteria (SRB) for the electron donor, acetate. Thus, the onset of sulfate reduction is not an intrinsic limit on the Fe(III) mineral that can be utilized as a terminal electron acceptor. In systems where acetate is not limiting, it is possible that the FeRB would be able to utilize significantly more Fe(III) after the onset of sulfate reduction, albeit less efficiently. This behavior is consistent with observations of low concentration sulfate column experiments performed with sediments from the Rifle IFRC site (Moon et al., 2007).

### 2.3.2 Abiotic Reaction Processes, Fang et al. (2009)

The Rifle biostimulation modeling study by Yabusaki et al. (2007), which focused on microbially-mediated TEAPs, allowed early progress under a simple conceptualization of the reaction network. Clearly, a combination of hydrologic, geochemical, and biological factors control the effectiveness of the uranium immobilization, making it a challenge to reliably predict important behaviors during and after bioremediation. An important consideration is the impact of changes in the geochemical environment induced by the acetate-mediated biostimulation. Of interest is the abiotic response (e.g., mineral precipitation and dissolution, aqueous and surface complexation) to the products of the TEAP reactions: bicarbonate, U(IV), Fe(II) and sulfide. Of the millimolar concentrations of Fe(II) and sulfide produced by the respective TEAPs during biostimulation, only micromolar concentrations are found in solution. Thus, nearly all of the bioreduced products of the biostimulation are strongly associated with the solid phases. These reduced phases may play an important role in long-term stabilization of immobilized uranium. The inclusion of abiotic chemistry in the modeled reaction network is also necessary to account for changes in solution chemistry (e.g., pH, alkalinity, and calcium) that nominally control uranium speciation and mobility. Uranium has a broad range of mobility that is dependent on the redox state of the dissolved uranium, ambient water chemistry, and the surface reactivity of the subsurface sediments (Curtis et al., 2004; Davis et al., 2006; Davis and Kent, 1990; Davis et al., 2004).

<u>Uranium Surface Complexation</u>. Surface complexation is an important process in attenuating the mobility of uranium in the subsurface environment (Moyes et al., 2000; Pabalan et al., 1996). Under the ambient pH and alkalinity found in the groundwater at the Rifle IFRC site, a significant fraction of the U(VI) (principally as uranyl and uranyl carbonate) would be expected to adsorb to the sediments via surface complexation. Zheng et al. (2003) and Fox et al. (2006) provided experimental evidence of the strong influence of calcium on the sorption of U(VI), through competition of the aqueous complex $Ca_2UO_2(CO_3)_3$ (Figure 2.3) with the iron surface complexes.

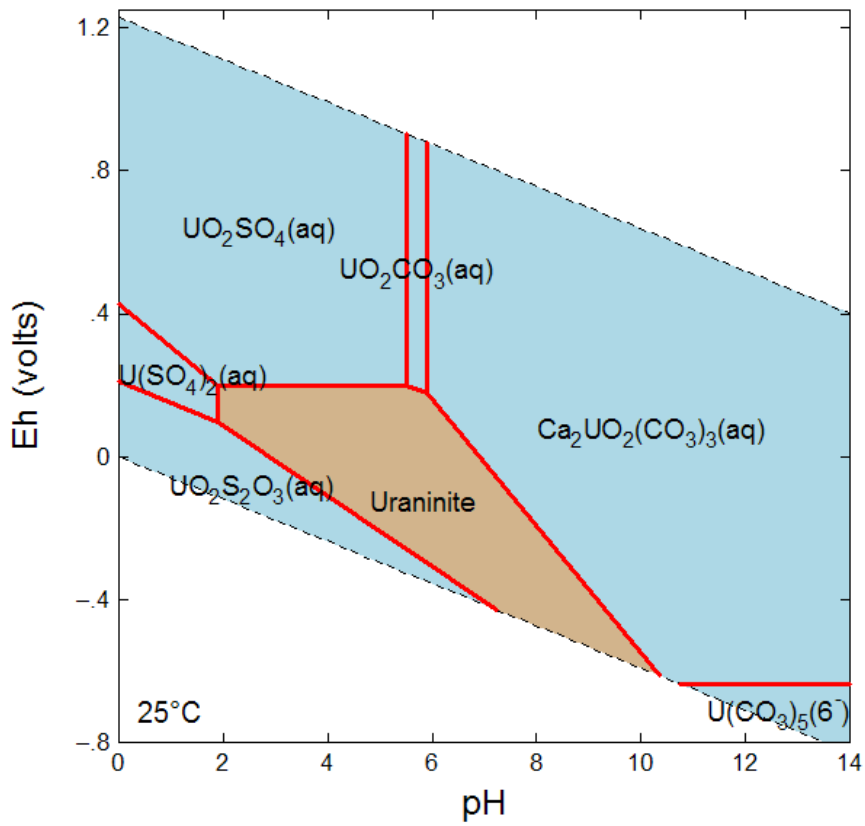


**Figure 2.3.** Uranium aqueous speciation assuming Rifle groundwater chemistry.

<u>Phyllosilicate Iron Reduction</u>. Until recently, it was commonly assumed that Fe(III)-oxides and oxyhydroxides were the principal terminal electron acceptor for iron reduction (Roden and Zachara, 1996). Under this conceptual process model, the biologically mediated reductive dissolution of Fe(III)-oxides liberates millimolar concentrations of $Fe^{++}$, which must quickly be associated with the aquifer solids to agree with the observed micromolar $Fe^{++}$ concentrations. This required a particularly strong $Fe^{++}$ surface complexation model that had difficulty reproducing the aqueous $Fe^{++}$ dynamics observed during the iron-reducing phase. The preferential bioreduction of phyllosilicate Fe(III) over Fe(III)-oxides was recently identified in Rifle IFRC laboratory studies by Komlos et al.(2008b). This finding permitted an important refinement to the conceptual model of processes and properties controlling uranium mobility during biostimulation. In this case, the higher rate of microbial reduction of phyllosilicate iron accounts for ~90% of the bioreduced iron, with the remainder attributed to the reduction of iron oxides and oxyhydroxides. In the phyllosilicate Fe(III) TEAP, the biogenic Fe(II) largely remains in the layer silicate structure. With less $Fe^{++}$ entering solution, the representation of $Fe^{++}$ dynamics was significantly improved. Thus, the reactive transport model now accounts for parallel Fe(III) TEAPs for oxides/oxyhydroxides and phyllosilicates.

Sulfate Reduction. The impact of the SRB becomes more noticeable after ~30 days of acetate amendment, when the abundance of this group increases sufficiently to collectively remove a large fraction of the ~9 millimolar sulfate present in the groundwater. At this point, the SRB are outcompeting the FeRB for acetate. For each mole of acetate oxidized in the sulfate TEAP reaction, approximately 1 mole of sulfide and 2 moles of bicarbonate are produced. Observed solution concentrations of sulfide and bicarbonate during sulfate reduction, while elevated, represent a very small fraction of these TEAP products. In the model, calcite, iron sulfide, and elemental sulfur are predicted to be the principal sinks for the bicarbonate and sulfide removed from solution. Over longer periods of biostimulation, the volume fraction of these secondary minerals could be sufficient to alter the aquifer permeability (Englert et al., 2009; Li et al., 2009). Higher abundance of these reduced oxidation state sulfur phases is correlated with longer-term post-biostimulation uranium removal. During sulfate bioreduction, the elevated bicarbonate concentrations and the net increase in pH from the mineral reactions are favorable conditions for uranium desorption. This behavior is accounted for in the uranium surface complexation model and is responsible, in part, for the higher (but still less than influent) uranium concentrations predicted during sulfate reduction.

Mineral Reactions. Based on the background geochemical conditions and the products of the principal TEAP reactions, calcite, siderite, iron sulfide, and elemental sulfur were added to the reaction network with rates as a function of the saturation state. An important sulfide sink was the inclusion of the reaction of goethite with sulfide that produced elemental sulfur and Fe(II).

## 2.4 Conceptual Process Model

The integration of the abiotic chemistry with the TEAPs in the modeling allows for more accurate representation of the impact of biostimulation products on uranium behavior. pH and alkalinity, for example, have strong impacts on uranium mobility; yet, the aqueous concentrations of bicarbonate and other TEAP reaction products (e.g., Fe(II), sulfide) are more than an order of magnitude smaller than what was produced. This underscores the importance of accurately representing the solid phase reactions (e.g., mineral reactions for carbonates, iron sulfides; iron and uranium surface complexation) that control the pH, Eh, alkalinity, and aqueous components of interest. Many of the secondary minerals that form during biostimulation can also contribute to longer-term post-biostimulation stabilization of reduced phases.

The resulting conceptual process model has the FeRB and SRB simultaneously active during biostimulation with the acetate electron donor. Initially, the FeRB are much more active leading to relatively rapid reduction of the Fe(III) mineral terminal electron acceptor and the concomitant reduction of the trace concentrations of the U(VI) electron acceptor. Only a small fraction of the biogenic Fe(II) is found in solution; the bulk is reduced in place in the layer silicates or sorbed to mineral surfaces. The SRB activity is linked to their biomass, which is initially low. Compounded by a relatively slow intrinsic growth rate, conversion of the sulfate terminal

electron acceptor during the first 4 to 5 weeks of biostimulation is negligible. In general, acetate consumption during this period is relatively low, ~0.5 mM or about 10-20% of what is available. This excess acetate allows the acetate electron donor to migrate further downgradient, resulting in a larger zone of metal reduction.

As the SRB biomass steadily increases, the rate of the sulfate TEAP increases commensurately until sulfate reduction is the dominant biologically mediated process. High ambient sulfate concentrations (~8-10 mM), high stoichiometric acetate consumption (~8 times the FeRB stoichiometry), and now high sulfate TEAP reaction rates result in significant depletion of the acetate electron donor. Important consequences of the predominance of sulfate reduction include 1) less acetate available for FeRB, 2) production of significant quantities of bicarbonate and sulfide, and 3) slight net increase in pH primarily from sulfide – Fe(III) mineral reactions. Each of these impacts can limit the net removal of U(VI) from the groundwater. In the Monod rate law, lower acetate concentrations will depress the TEAP rates including U(VI) bioreduction. Elevated bicarbonate concentrations lead to the formation of higher concentrations of aqueous U(VI)-carbonate complexes and the precipitation of carbonate minerals. Sulfide reacts with Fe(II) to precipitate iron sulfides. Sulfide reaction with Fe(III) minerals results in the formation of elemental sulfur and additional Fe(II). In the uranium surface complexation model, removal of U(VI) from groundwater via bioreduction, increase in alkalinity, and pH increase, all favor U(VI) desorption. U(VI) bioreduction is still occurring but the net impact of the sulfate reduction is a net increase in aqueous U(VI) concentrations compared to the earlier period when Fe(III) reduction was predominate. These U(VI) concentrations are still lower than the influent U(VI) entering the treatment zone. As long as FeRB are active with sufficient acetate and U(VI) available, uranium bioreduction will continue. Under these conditions and in the absence of other U(VI) sources, there will be a progressive removal of U(VI) from groundwater with distance from the injection gallery.

# 3 Model Specification

## 3.1 Hydrologic Model

The variably saturated flow conditions at many shallow alluvial aquifers are amenable to a single-phase, constant-density Richard's equation (Bear and Bahmat, 1991) modeling approach. However, for the conditions being investigated in this particular modeling study at the Rifle IFRC site, we use a fully coupled two-phase (liquid and gas) formulation with variable density. The active gas phase was necessary to account for the gas entrapment mechanism in the seasonal water table fluctuation and the flood scenarios, whereas the variable density formulation was necessary to account for amendment injectate that was denser than the groundwater. The STOMP simulator (White and Oostrom, 2006) that we use for the modeling of the Rifle variably saturated flow and gas entrapment in this study is based on Equations 3.1 to 3.4.

The water mass conservation equation, shown in Equation 3.1, equates the time rate of change of water mass within a control volume with the flux of water mass crossing the control volume surface. In the STOMP simulator, water exists in the diffusive pore space as liquid water in the aqueous phase and water vapor in the gas phase. Water transport occurs by advection through the aqueous and gas phases and by diffusion-dispersion through the gas phase. Flow of fluid phases is computed from Darcy's Law. Transport of phase components is computed from a modified form of Fick's law, where a combined diffusion-dispersion coefficient replaces the classical Fickian diffusion coefficient. Equation 3.1 includes an osmotic flux term, which accounts for the flow of aqueous fluid by osmotic pressure for simulations with coupled salt transport.

$$\frac{\partial}{\partial t}\left[\sum_{\gamma=l,g}\left(n_D \omega_\gamma^w \rho_\gamma s_\gamma\right)\right] = -\sum_{\gamma=l,g}\left(\nabla \mathbf{F}_\gamma^w + \nabla \mathbf{J}_\gamma^w\right) - \nabla \mathbf{F}_l^S + \dot{m}^w \tag{3.1}$$

where,

$$\mathbf{F}_\gamma^w = -\frac{\omega_\gamma^w \rho_\gamma k_{r\gamma} \mathbf{k}}{\mu_\gamma}\left(\nabla P_\gamma + \rho_\gamma g \mathbf{z}_g\right) \quad for\ \gamma = \ell, g$$

$$\mathbf{J}_\gamma^w = -\tau_\gamma n_D \rho_\gamma s_\gamma \frac{M^w}{M_\gamma} D_\gamma^w \nabla \chi_\gamma^w \quad for\ \gamma = \ell, g$$

$$\mathbf{F}_\ell^S = D_\ell^S \nabla S_\ell$$

The air mass conservation equation, shown in Equation 3.2 equates the time rate of change of the air mass within a control volume with the flux of air mass crossing the control volume surface. In

the STOMP simulator, air exists in the diffusive pore space as a component of the gas phase and dissolved in the aqueous phase. Air transport occurs by advection and diffusion-dispersion through the aqueous and gas phases. Flow of fluid phases is computed from Darcy's Law. Transport of phase components is computed from a modified form of Fick's law, where a combined diffusion-dispersion coefficient replaces the classical Fickian diffusion coefficient.

$$\frac{\partial}{\partial t}\left[\sum_{\gamma=\ell,g}\left(n_D\,\omega_\gamma^a\,\rho_\gamma\,s_\gamma\right)\right] = -\sum_{\gamma=\ell,g}\left(\nabla\,\mathbf{F}_\gamma^a + \nabla\,\mathbf{J}_\gamma^a\right) + \dot{m}^a \tag{3.2}$$

where,

$$\mathbf{F}_\gamma^a = -\frac{\omega_\gamma^a\,\rho_\gamma\,k_{r\gamma}\,\mathbf{k}}{\mu_\gamma}\left(\nabla\,P_\gamma + \rho_\gamma\,g\,\mathbf{z}_g\right)\ \ for\ \gamma=\ell,g$$

$$\mathbf{J}_\gamma^a = -\tau_\gamma\,n_D\,\rho_\gamma\,s_\gamma\,\frac{M^a}{M_\gamma}\,D_\gamma^a\,\nabla\,\chi_\gamma^a\ \ for\ \gamma=\ell,g$$

$\mathbf{F}_l^S$ = osmotic flux of the aqueous phase

$\mathbf{F}_\gamma^{\mathrm{w}}$ = advective flux of water in phase $\gamma$

$\mathbf{F}_\gamma^{\mathrm{a}}$ = advective flux of air in phase $\gamma$

$\mathbf{J}_\gamma^{\mathrm{w}}$ = diffusive – dispersive flux of water for phase $\gamma$

$\mathbf{J}_\gamma^{\mathrm{a}}$ = diffusive – dispersive flux of air for phase $\gamma$

$n_D$ = diffusive porosity

$\omega_\gamma^w$ = mass fraction of water in phase $\gamma$

$\omega_\gamma^a$ = mass fraction of air in phase $\gamma$

$\rho_\gamma$ = density for phase $\gamma$

$s_\gamma$ = saturation of phase $\gamma$

$\dot{m}^w$ = mass source rate of water

$\dot{m}^a$ = mass source rate of air

$k_{r\gamma}$ = fluid relative permeability of phase $\gamma$

$k$ = intrinsic permeability tensor

$\mu_\gamma$ = kinematic viscosity of phase $\gamma$

$P_\gamma$ = pressure of phase $\gamma$

$g$ = acceleration of gravity

$z_g$ = unit gravitational direction vector

$\tau_\gamma$ = phase tortuosity for phase $\gamma$

$M^w$ = molecular weight of water

$M^a$ = molecular weight of air

$M_\gamma$ = molecular weight of phase $\gamma$

$D_\gamma^w$ = diffusion coefficient of water in phase $\gamma$

$D_\gamma^a$ = diffusion coefficient of air in phase $\gamma$

$\chi_\gamma^w$ = mole fraction of water in phase $\gamma$

$\chi_\gamma^a$ = mole fraction of air in phase $\gamma$

$D_l^S$ = salt diffusion coefficient for liquid phase

$S_l$ = salt concentration in liquid phase

### 3.1.1 Gas Entrapment

We use the hysteretic saturation function of Kaluarachchi and Parker (1992) to account for entrapped gas as a component in otherwise saturated pores. Gas entrapment during aqueous-phase imbibition depends on the aqueous saturation and current saturation path. Gas effective residual saturations are computed using an empirical relationship developed by Land (1968) for aqueous-NAPL systems. In this simplified hysteretic model for aqueous-gas systems, gas can be trapped or free, where free gas refers to continuous volumes which advect freely and trapped gas refers to discontinuous ganglia of gas occluded within the aqueous phase. Occluded gas is assumed to be immobile. In hysteretic systems, the residual saturation is independent of capillary pressure. The effective trapped gas saturation is computed according to Equation 3.3, which recognizes that entrapped gas cannot exceed the gas present. Land's parameter for gas-aqueous interfaces, $L_g$, is $\frac{1}{{}^{i}\bar{s}_{g_r}} - 1$, where ${}^{i}\bar{s}_{g_r}$ is the maximum effective residual gas saturation.

$$\bar{s}_{g_{tl}} = \min\left\{\left[\frac{1-\bar{s}_l^{\min}}{1+L_g\left(1-\bar{s}_l^{\min}\right)} - \frac{1-\tilde{s}_l}{1+L_g\left(1-\tilde{s}_l\right)}\right], \bar{s}_g\right\} \quad \text{, for } \tilde{s}_l > \bar{s}_l^{\min} \tag{3.3}$$

where $\bar{s}_{g_{tl}}$ = effective gas saturation trapped by aqueous phase

$\bar{s}_l^{\min}$ = minimum effective aqueous saturation

$\tilde{s}_l$ = apparent aqueous saturation = $\bar{s}_l + \bar{s}_{g_{tl}}$

$\bar{s}_l = \frac{s_l - s_m}{1 - s_m}$

$s_l$ = actual aqueous saturation

$s_m$ = actual irreducible aqueous saturation

$\bar{s}_g$ = effective gas saturation

$L_g$ = Land's parameter for gas-aqueous interfaces

${}^{i}\bar{s}_{g_r}$ = maximum effective residual gas saturation.

### 3.1.2 Transport

Transport occurs through liquid and gas phases with Darcy's Law calculation of the advective velocity. The solute conservation equation, shown in Equation 3.4, equates the time rate of change of solute within a control volume with the flux of solute crossing the control volume surface. In the STOMP simulator, solute is partitioned among the fluid and solid phases through equilibrium and kinetic reactions. Solute transport occurs by advection and diffusion-dispersion through the aqueous phase and gas phase.

$$\frac{\partial C^i}{\partial t} = -\sum_{\gamma=l,g}\left(\nabla\left[C_\gamma^i \mathbf{V}_\gamma\right]\right) + \dot{m}^{C^i} - \dot{R}^{C^i} C^i + \sum_{\gamma=l,g}\left(\nabla\left[\left(\tau_\gamma s_\gamma n_D D_\gamma^{C^i} + s_\gamma n_D \mathbf{D}_{h_\gamma}\right)\nabla C_\gamma^i\right]\right) \tag{3.4}$$

where,

$$\mathbf{V}_\gamma = -\frac{k_{r\gamma}\,\mathbf{k}}{\mu_\gamma}\left(\nabla P_\gamma + \rho_\gamma\, g\, \mathbf{z}_g\right) \quad for\ \gamma = \ell, g$$

$\mathbf{V}_\gamma$ = Darcy flux of phase $\gamma$

$C^i$ = concentration of component i

$C_\gamma^i$ = concentration of component i in phase $\gamma$

$n_D$ = diffusive porosity

$\rho_\gamma$ = density for phase $\gamma$

$s_\gamma$ = saturation of phase $\gamma$

$\dot{m}^{C^i}$ = mass source rate of component i

$\dot{R}^{C^i}$ = solute decay rate constant

$k_{r\gamma}$ = fluid relative permeability of phase $\gamma$

$k$ = intrinsic permeability tensor

$\mu_\gamma$ = kinematic viscosity of phase $\gamma$

$P_\gamma$ = pressure of phase $\gamma$

$g$ = acceleration of gravity

$z_g$ = unit gravitational direction vector

$\tau_\gamma$ = phase tortuosity for phase $\gamma$

$D_\gamma^{C^i}$ = diffusion coefficient of component i in phase $\gamma$

$D_{h_\gamma}$ = diffusion coefficient of air in phase $\gamma$

### 3.1.3 Solution Procedure

The STOMP simulator has been developed by the Pacific Northwest National Laboratory to predict thermal and hydrological flow and reactive transport in variably saturated subsurface environments. It is a fully functional, multiphase, multi-component reservoir code used extensively in environmental and gas/$CO_2$ modeling applications. STOMP solves nonlinear

partial differential equations for the conservation equations, with reactive transport occurring over mobile phases. The nonlinear equations describing mass and/or energy conservation are discretized spatially on structured orthogonal grids using the integral finite difference approach, and temporally using first-order backward Euler differencing. The nonlinearities from the constitutive equations that relate the primary and secondary variables are resolved using Newton-Raphson iteration. The global implicit solution of the algebraic system of equations uses a preconditioned conjugate gradient sparse matrix solver (BiCGstab with block-jacobi ILU preconditioning).

After solution of the flow equations, the hydrologic transport equations are solved using a TVD (total variation diminishing) scheme. The coupled hydrologic transport and mixed geochemical reaction systems are solved using an operator splitting approach with no iteration between the transport and reaction systems. The chemistry module ECKEChem (Equilibrium-Conservation-Kinetic-Equation Chemistry) solves mass balance equations, mass action equations, and kinetic equations simultaneously using the Newton-Raphson approach. The simulator has several different operational modes, i.e., different source code depending on the solved governing equations (e.g., water mass, air mass, dissolved-oil mass, oil mass, salt mass, thermal energy).

### 3.1.4 Hydrologic Modeling Parameters

Liquid phase boundary conditions for the hydrologic model are based on observed upgradient and downgradient water levels. The gas phase boundary condition at the ground surface is atmospheric pressure. It should be noted that the elevation of the Rifle IFRC site is 5300 feet above mean sea level and the pressure is nominally 0.8224 atmospheres. This non-standard atmospheric pressure was taken into account for the calculation of dissolved oxygen in equilibrium with the gas phases.

Bromide tracer was included in the acetate amendment that was released into the Rifle aquifer. The hydraulic conductivity, porosity, and dispersivity for the 2008 experiment have been calibrated based on observations of bromide tracer migration. The unsaturated flow parameters are based on the Brooks-Corey saturation functions (Brooks and Corey, 1966) and were developed for the Rifle aquifer materials. The hydrologic modeling parameters of the site are summarized in Table 3.1. Initial and boundary conditions are based on measured concentrations of chemical components and water quality (e.g., pH, Eh, alkalinity). Initial sorbed U(VI) partitioning is calculated by using the uranium surface complexation model to equilibrate with measured aqueous U(VI) concentrations.

**Table 3.1.** Parameters for hydrologic modeling and transport

| Hydrologic Parameter | Value |
|---|---|
| Air Entry Pressure Head | 1.00925 cm |
| Pore-Size Distribution Index | 0.257979 |
| Residual Saturation | 0.0712 |
| Saturated Hydraulic Conductivity | 8 m/d |
| Effective Porosity | 0.10 |
| Dispersivity | 0.4 m |

## 3.2 Biogeochemical Model

### 3.2.1 Biologically Mediated Reactions

The biologically mediated reactions and rate laws are based on acetate as the electron donor, three principal terminal electron acceptors (Fe(III) mineral, U(VI), and sulfate), and two functional microbial groups (FeRB and SRB).

For the FeRB (ostensibly *Geobacter* spp.), two parallel competing TEAP reactions are used to catalyze the conversion of Fe(III) mineral to Fe(II). The first uses goethite as the nominal Fe(III) oxide/oxyhydroxide terminal electron acceptor, whereas the second parallel reaction uses phyllosilicate Fe(III), identified by Komlos et al. (2008b) as the principal source for bioavailable Fe(III).

<u>Fe(III) oxide TEAP</u>

$$0.125CH_3COO^- + FeOOH(s) + 1.875H^+ = Fe^{++} + 1.5H_2O + 0.25HCO_3^- \quad (3.5)$$

<u>Phyllosilicate Fe(III) TEAP</u>

$$0.125\ CH_3COO^- + Fe(III)(ls) + 0.5H_2O = 0.25HCO_3^- + 0.9\ Fe(II)(ls) + 0.1\ Fe^{++} + 1.125H^+ \quad (3.6)$$

Based on the low biomass yield for *Geobacter* reported by Mahadevan et al. (2006), catabolic stoichiometry is assumed for both the oxide and phyllosilicate Fe(III) TEAP reactions.

For the bioreduction of U(VI) in groundwater, uranyl ($UO_2^{++}$) is used as the terminal electron acceptor in the TEAP reaction, which is also mediated by the FeRB microbial population (i.e., *Geobacter* spp.).

<u>U(VI) TEAP</u>

$$0.1250CH_3COO^- + 0.3538H_2O + 0.0113NH_4^+ + 0.3875UO_2^{++} = 0.0113BM_FeRB + 0.855H^+ + 0.1938HCO_3^- + 0.3875UO_2(s) \quad (3.7)$$

Note that the abiotic uranium aqueous and surface complexation reaction model (described in section 3.2.2) requires 22 U(VI) aqueous species in addition to uranyl. As uranyl is consumed in the biologically mediated TEAP reaction, all other U(VI) species will diminish due to the assumption that all aqueous complexation reactions for uranium are fast reactions.

The TEAP reaction for sulfate reduction (Equation 3.8) is associated with an attached population of sulfate-reducing bacteria (SRB):

<u>Sulfate TEAP</u>

$$0.125CH_3COO^- + 0.0057H^+ + 0.0038NH_4^+ + 0.1155SO_4^{--} = 0.0038BM_SRB + 0.0114H_2O + 0.231HCO_3^- + 0.1155HS^- \quad (3.8)$$

The stoichiometries in Equations 3.7 and 3.8 which include the yield of an immobile biomass of 0.17 g cells/g acetate and 0.058 g cells/g acetate, respectively, are energetics-based (Rittmann and McCarty, 2001) under the assumption of a biomass molecular formula of $C_5H_7O_2N$ and an energy transfer efficiency value of 0.6.

**Rate Law for Biologically Mediated Reactions**. A recent conceptual model update has both functional microbial groups, FeRB and SRB, present and active during the initial period of biostimulation. In this case, the initial reaction rate of the sulfate TEAP is slow, reflecting the lower abundance and slower growth rate of the SRB. Sulfate reduction during this early period is negligible and the initial groundwater observations are dominated by elevated aqueous Fe(II) and conversion of aqueous U(VI) to insoluble U(IV) catalyzed by the FeRB. As SRB biomass increases, the bulk sulfate TEAP reaction rate increases and after ca. 30 days of acetate amendment, sulfate reduction becomes the dominant TEAP and consumer of acetate.

The kinetics of the microbially mediated TEAP reactions is of the Monod type with thermodynamic control for all the TEAP reactions. In conjunction with the four biologically mediated reduction reactions (i.e., phyllosilicate Fe(III), oxide Fe(III), U(VI), and sulfate), the acetate consumption rate, $R_C^{bio}$, can be identified as:

$$R_C^{bio} = -\sum_{eA}^{N_{eA}} \mu_{m,eA} s_C B \left( \frac{C_C}{K_{s,C} + C_C} \right) \left( \frac{C_{eA}}{K_{s,eA} + C_{eA}} \right) f\left(\Delta G_r\right) \tag{3.9}$$

where $N_{eA}$ = number of terminal electron acceptors
$s_C$ = stoichiometric coefficient of acetate in the TEAP reaction
$C_c$ = acetate concentration
$B$ = biomass concentration of microorganism mediating the TEAP reaction
$C_{eA}$ = terminal electron acceptor concentration
$\mu_{m,eA}$ = acetate oxidation rate for the terminal electron acceptor
$K_{s,C}$ = half-saturation coefficient for acetate
$K_{s,eA}$ = half-saturation coefficient for the terminal electron acceptor
$f(\Delta G_r)$ = $1 - \exp[(\Delta G_r - \Delta G_{\min})/RT]$
$\Delta G_r$ = free energy change of the corresponding TEAP reaction
$\Delta G_{\min}$ = minimum free energy change required to drive ATP Synthesis
$R$ = gas constant
$T$ = absolute temperature.

In the updated model for the baseline system, the three TEAPs of interest (Fe(III), U(VI), and sulfate) are simultaneously active but only the sulfate TEAP reaction rate depends on the amount of biomass. In this case, the SRB biomass is initially low such that the sulfate TEAP, while active, is nearly imperceptible. As the SRB biomass slowly grows, the TEAP reaction rate increases commensurately. A first-order decay model (dB/dt = -B) is used to describe the loss of SRB biomass. Eventually, after 4 to 5 weeks, the net growth of SRB biomass is sufficient for sulfate reduction to become the dominant TEAP reaction and principal consumer of acetate.

In the case of Fe(III)-oxide bioreduction, the terminal electron acceptor is a solid phase so we replace the second Monod term with the available surface hydroxyl site density in equivalent molarity. This is based on the assumption that the reactivity of the Fe(III) oxide/oxyhydroxide terminal electron acceptor is reduced by Fe(II) surface complexation (Liu et al., 2001; Urrutia et al., 1999). For phyllosilicate Fe(III) reduction, the second Monod term is eliminated and the rate law simplifies to second order kinetics limited by the bioavailability of phyllosilicate Fe(III). For the U(VI) TEAP, $C_{eA}$ in the Monod expression is total aqueous U(VI) without the calcium-uranyl-carbonate complexes because they have been shown to be thermodynamically inhibited for bioreduction (Brooks et al., 2003) .

### 3.2.2 Abiotic Reactions

In addition to the biologically mediated reactions, the modeled biogeochemical reaction network includes uranium aqueous and surface speciation reactions, Fe(II) aqueous and sorption reactions, mineral dissolution and precipitation and other aqueous complexation reactions.

**Surface Complexation.** The uranium surface complexation model (Table 3.2) was developed from batch experiments with Rifle sediments performed over a relevant range of pH, alkalinity, and uranium concentrations. The generalized composite surface complexation approach (Davis et al., 1998; Davis et al., 2004; Waite et al., 2000) that was used considered two sorption reactions with three different sites—0.01% very strong sites (>SSOH), 0.1% strong sites (>SOH), and 99.89% weak sites (>WOH)—which are defined by their relative binding strength for U(VI), assuming a total site density of 3.84 μmoles $m^{-2}$ of hydroxyl groups and a surface area of 4.256 $m^2g^{-1}$. Stability constants for the six surface complexation reactions were parameterized from batch experiment data.

**Table 3.2**. U(VI) surface complexation reactions.

| **Surface Species** | |
|---|---|
| Reaction | logK (estimated) |
| $SSOH + UO_2^{2+} = SSOUO_2^{+} + H^{+}$ | 12.28 |
| $SOH + UO_2^{2+} = SOUO_2^{+} + H^{+}$ | 6.95 |
| $WOH + UO_2^{2+} = WOUO_2^{+} + H^{+}$ | 2.74 |
| $SSOH + UO_2^{2+} + H_2O = SSOUOOH + 2H^{+}$ | 0.033 |
| $SOH + UO_2^{2+} + H_2O = SOUOOH + 2H^{+}$ | -2.12 |
| $WOH + UO_2^{2+} + H_2O = WOUOOH + 2H^{+}$ | -5.01 |
| SSOH denoting very strong binding sites: 0.01% of total sites | |
| SOH denoting strong binding sites: 0.1% of total sites | |
| WOH denoting weak binding sites: 99.89% of total sites | |

The model system is based on 22 aqueous uranium complexation reactions (including Ca-$UO_2$-$CO_3$ ternary complexes) (Table 3.3). The primary benefit from this level of detail in uranium modeling is to more accurately represent the sensitivity of U(VI) mobility to changes in alkalinity, pH, and uranium concentrations. These are all well-known abiotic consequences of *in situ* biostimulation.

**Table 3.3.** Uranium species and their formation constants.

| Aqueous Species | |
|---|---|
| Reaction | logK (I = 0) [(a)] |
| $UO_2^{2+} + H_2O = UO_2OH+ + H^+$ | -5.25 |
| $UO_2^{2+} + 2H_2O = UO_2(OH)_{2(aq)} + 2H^+$ | -12.15 |
| $UO_2^{2+} + 3H_2O = UO_2(OH)_3^- + 3H^+$ | -20.25 |
| $UO_2^{2+} + 4H_2O = UO_2(OH)_4^{2-} + 4H^+$ | -32.40 |
| $2UO_2^{2+} + H_2O = (UO_2)_2OH^{3+} + H^+$ | -2.70 |
| $2UO_2^{2+} + 2H_2O = (UO_2)_2(OH)_2^{2+} + 2H^+$ | -5.62 |
| $3UO_2^{2+} + 4H_2O = (UO_2)_3(OH)_4^{2+} + 4H^+$ | -11.90 |
| $3UO_2^{2+} + 5H_2O = (UO_2)_3(OH)_5^+ + 5H^+$ | -15.55 |
| $3UO_2^{2+} + 7H_2O = (UO_2)_3(OH)_7^- + 7H^+$ | -32.20 |
| $4UO_2^{2+} + 7H_2O = (UO_2)_4(OH)_7^+ + 7H^+$ | -21.90 |
| $UO_2^{2+} + CO_3^{2-} = UO_2CO_{3(aq)}$ | 9.94 |
| $UO_2^{2+} + 2CO_3^{2-} = UO_2(CO_3)_2^{2-}$ | 16.61 |
| $UO_2^{2+} + 3CO_3^{2-} = UO_2(CO_3)_3^{4-}$ | 21.84 |
| $3UO_2^{2+} + 6CO_3^{2-} = (UO_2)_3(CO_3)_6^{6-}$ | 54.00 |
| $2UO_2^{2+} + CO_3^{2-} + 3H_2O = (UO_2)_2CO_3(OH)_3^- + 3H^+$ | -0.85 |
| $3UO_2^{2+} + CO_3^{--} + 3H_2O = (UO_2)_3CO_3(OH)_3^+ + 3H^+$ | 0.66 |
| $UO_2^{2+} + Cl^- = UO_2Cl^+$ | 0.17 |
| $Ca^{2+} + UO_2^{2+} + 3CO_3^{2-} = CaUO_2(CO_3)_3^{2-}$ | 25.40 [(b)] |
| $2Ca^{2+} + UO_2^{2+} + 3CO_3^{2-} = Ca_2UO_2(CO_3)_3^0(aq)$ | 30.55 [(b)] |
| $UO_2^{2+} + 2Cl^- = UO_2Cl2(aq)$ | -1.10 |
| $UO_2^{2+} + SO_4^{2-} = UO_2(SO_4)aq$ | 3.15 |
| $UO_2^{2+} + 2SO_4^{2-} = UO_2(SO_4)_2^{2-}$ | 4.14 |

(a) Values from Guillaumont et al.(2003), unless otherwise indicated.
(b) Bernhard et al.(2001).

A general, non-electrostatic surface complexation approach (Table 3.4) similar to the uranium surface complexation model proposed by Davis et al. (2004) was used to model Fe(II) sorption.

**Table 3.4.** $Fe^{2+}$ surface complexation reactions.

| Surface Species | |
|---|---|
| Reaction | logK (estimated) |
| $>FeOH + H^+ = >FeOH_2^+$ | 7.47 |
| $>FeOH = >FeO^- + H^+$ | -9.51 |
| $>FeOH + Fe^{2+} = >FeOFe^+ + H^+$ | -5.00 |
| $>FeOH + Fe^{2+} + H_2O = >FeOFeOH + 2H^+$ | -11.96 |

This approach may be the most appropriate for complex field applications since it is difficult to characterize surface charging behavior of non-ideal natural mineral phases (Davis et al., 1998). Note that the abiotic reduction of adsorbed uranyl by adsorbed Fe(II) was not included in the reaction network. While there have been observations of abiotic uranium reduction in the literature (Liger et al., 1999; Regenspurg et al., 2009; Scott et al., 2005), they usually involve model minerals and/or electron shuttles (e.g., AQDS). Reduced natural sediments in the absence of microbial activity, apparently are recalcitrant to reduction of adsorbed U(VI) (Jeon et al., 2005; Ortiz-Bernad et al., 2004). This is consistent with biostimulation events at the Rifle IFRC site where there has been no observation of abiotic reduction of U(VI). Furthermore, a recent field experiment at the Rifle IFRC site that specifically targeted abiotic U(VI) reduction via Fe(II) amendment also showed negligible U(VI) conversion.

**Mineral Reactions.** As mentioned in Section 2.3.2 the TEAP reactions can generate 1-2 orders of magnitude more bicarbonate, Fe(II), and sulfide than is measured in solution. Thus, solid phase reactions are important for accurately representing the water chemistry, which ultimately controls uranium behavior. Table 3.5 includes all abiotic mineral reactions in the reaction network. These reactions also have relevance for pore space reduction via mineral precipitation.

**Table 3.5.** Modeled mineral reactions.

$Ca^{2+} + HCO_3^- = Calcite(s) + H^+$
$Fe^{2+} + HCO_3^- = Siderite(s) + H^+$
$Fe^{2+} + HS^- = FeS(s) + H^+$
$2FeOOH + HS^- + 5H^+ = 2Fe^{2+} + S^0 + 4H_2O$

The principal sink for excess carbonate is the precipitation of calcite, which is predicted to account for the bulk of secondary mineral volume fraction. Iron sulfides are predicted to form in significant amounts during the sulfate reduction phase; however, the $Fe^{++}$ that is available from the bioreduction of Fe(III) mineral is limiting. An important reaction that facilitates the removal of sulfide from solution and the production of FeS(s) is the abiotic oxidation of dissolved sulfide by goethite (Canfield, 1989; Pyzik and Sommer, 1981; Zopfi et al., 2008) (Table 3.5). In this reaction elemental sulfur is precipitated and additional $Fe^{2+}$ is produced. This reaction is consistent with recent column studies of acetate biostimulation in Rifle sediments that have identified significant elemental sulfur abundance during sulfate reduction. The rate law used for this reaction is

$$R = k\,[FeOOH]\,[HS^-], \tag{3.10}$$

where k is the rate constant, [FeOOH] and $[HS^-]$ are species concentrations of FeOOH and $HS^-$, respectively. All other mineral reactions use the following rate formulations that are a function of the saturation state (Hunter et al., 1998):

$$R_i = \begin{cases} k_i(\Omega_i - 1) & \text{for } \Omega_i \geq 1 \\ k_{-i}[Q_i](\Omega_i - 1) & \text{for } \Omega_i < 1 \end{cases} \tag{3.11}$$

where *i* represents the i-th mineral phase, $R_i$ is the rate of the reaction, $k_i$ is the mineral precipitation rate constant [$ML^{-3}T^{-1}$], $k_{-i}$ is the mineral dissolution rate constant [$T^{-1}$], $Q_i$ is the concentration of the i-th mineral phase [$ML^{-3}$], and $\Omega_i$ is the saturation index of the i-th mineral phase.

In general, the abiotic, non-uranium, aqueous reactions involving the primary components of interest ($H^+$, $NH_4^+$, $Na^+$, $K^+$, $Ca^{2+}$, $Mg^{2+}$, $Fe^{2+}$, $Cl^-$, $HS^-$, $CO_3^{2-}$, $SO_4^{2-}$, $CH_3COO^-$) are modeled as equilibrium reactions with thermodynamics from the EQ3/6 database (Table 3.6).

**Table 3.6.** Equilibrium reactions in the reaction network.

| Equilibrium Reactions | |
|---|---|
| Reaction | LogK |
| $CH_3COO^- + H^+ = CH_3COOH$ | 4.76 |
| $Ca^{2+} + H_2O = CaOH^+ + H^+$ | -12.60 |
| $Ca^{2+} + CH_3COO^- = CaCH_3COO^+$ | 1.18 |
| $Ca^{2+} + CO_3^{2-} + H^+ = CaHCO_3^+$ | 11.33 |
| $Ca^{2+} + CO_3^{2-} = CaCO_3$ | 3.15 |
| $Ca^{2+} + SO_4^{2-} = CaSO_4$ | 2.31 |
| $CO_3^{2-} + 2H^+ = H_2CO_3$ | 16.68 |
| $CO_3^{2-} + H^+ = HCO_3$- | 10.33 |
| $Fe^{2+} + H_2O = FeOH^+ + H^+$ | -9.50 |
| $CH_3COO^- + Fe^{2+} = FeCH_3COO^+$ | 1.82 |
| $Fe^{2+} + CO_3^{2-} + H^+ = FeHCO_3^+$ | 12.33 |
| $Fe^{2+} + CO_3^{2-} = FeCO_3(aq)$ | 5.50 |
| $Fe^{2+} + 2CO_3^{2-} = Fe(CO_3)_2^{2-}$ | 7.10 |
| $Fe^{2+} + SO_4^{2-} = FeSO_4$ | 2.25 |
| $Fe^{2+} + Cl^- = FeCl^+$ | 0.90 |
| $Fe^{2+} + 2HS^- = Fe(HS)_2(aq)$ | 8.95 |
| $Fe^{2+} + 3HS^- = Fe(HS)_3^-$ | 10.99 |
| $HS^- + H^+ = H_2S(aq)$ | 6.99 |
| $HS^- = H^+ + S^{2-}$ | -12.92 |
| $K^+ + SO_4^{2-} = KSO_4^-$ | 0.85 |
| $Mg^{2+} + H_2O = MgOH^+ + H^+$ | -11.79 |
| $CH_3COO^- + Mg^{2+} = MgCH_3COO^+$ | 1.14 |
| $CO_3^{2-} + Mg^{2+} + H^+ = MgHCO_3^+$ | 11.40 |
| $CO_3^{2-} + Mg^{2+} = MgCO_3(aq)$ | 2.98 |

| | |
|---|---|
| $Mg^{2+} + SO_4^{2-} = MgSO_4(aq)$ | 2.25 |
| $Na^+ + CH_3COO^- = NaCH_3COO$ | -0.18 |
| $Na^+ + CO_3^{2-} + H^+ = NaHCO_3(aq)$ | 10.08 |
| $CO_3^{2-} + Na^+ = NaCO_3^-$ | 1.27 |
| $Na^+ + SO_4^{2-} = NaSO_4^-$ | 0.70 |
| $NH_4^+ = NH_3(aq) + H^+$ | -9.25 |
| $NH_4^+ + SO_4^{2-} = NH_4SO_4^-$ | 1.11 |
| $SO_4^{2-} + H^+ = HSO_4^-$ | 1.99 |
| $H_2O = OH^- + H^+$ | -14.00 |

### 3.2.3 Biogeochemical Model Calibration

The calibration of the biogeochemical reaction model is based on the estimation of rate law parameters for the biologically mediated reactions and the abiotic mineral reactions. A single set of these rate parameters has been determined to best represent all the large-scale field biostimulation experiments performed at the Rifle IFRC site (2002, 2003, 2007, and 2008).

Using spatial and temporal distributions of measured acetate, Fe(II), sulfate, U(VI), and pH, calibration included reaction network parameters for the TEAPs, Fe(II) sorption, precipitation of carbonate minerals and iron sulfide, and dissolution of goethite by sulfide. A stepwise approach was used to calibrate reaction parameters in the transport modeling framework. The TEAPs were used as a starting point. We assumed that during the early iron reduction period, acetate consumption is attributed to the predominant FeRB population. The maximum Fe(III) and sulfate bioreduction rates and the initial SRB biomass and decay rates were calibrated to match observed data. Fe(II) sorption, and secondary mineral reaction parameters were then fitted iteratively to match aqueous Fe(II), sulfide, alkalinity and pH. Uranium in the system is at trace concentrations compared to other species, so it does not significantly impact the major ion chemistry. Its full speciation was included in the reaction network once other reaction parameters were fixed. All calibrated parameters are summarized in Table 3.7.

**Table 3.7.** Values for rate law parameters.

| Parameter | Value |
|---|---|
| Precipitation rate constant for calcite | $1.644\times10^{-7}$ $Md^{-1}$ |
| Dissolution rate constant for calcite | $1.37\times10^{-6}$ $d^{-1}$ |
| Precipitation rate constant for siderite | $1.37\times10^{-6}$ $Md^{-1}$ |
| Dissolution rate constant for siderite | $1.37\times10^{-7}$ $d^{-1}$ |
| Precipitation rate constant for FeS(s) | $5.11\times10^{-6}$ $Md^{-1}$ |
| Dissolution rate constant for FeS(s) | $6.85\times10^{-6}$ $d^{-1}$ |
| Dissolution rate constant of goethite by sulfide | 20.8 $d^{-1}$ |
| Rate constant for phyllosilicate iron bioreduction | 0.075 $Md^{-1}$ |
| Rate constant for FeOOH bioreduction | 0.016 $d^{-1}$ |
| Half-Saturation for acetate | $5.0\times10^{-4}$ M |

| | |
|---|---|
| Initial amount of SRB | 0.003 μM |
| Rate constant for sulfate bioreduction | 90 $d^{-1}$ |
| Half-Saturation for sulfate bioreduction | $10^{-5}$ M |
| Rate constant for U(VI) conversion by FeRB | $2.5\times10^{-6}$ $Md^{-1}$ |
| Half-Saturation for U(VI) conversion by FeRB | $10^{-7}$ M |
| SRB decay rate | 0.015 $d^{-1}$ |

## 3.3 Numerical Model Specification

The baseline for this study is the 2008 biostimulation field experiment at the Rifle IFRC site nicknamed Big Rusty. This was the second biostimulation experiment performed in this particular experimental plot (Figure 2.2). In this case, a fairly long and complex acetate injection took place (Table 3.8). The operation of the injection gallery was designed to achieve a 10:1 dilution of the initial acetate and bromide injectate. 14 days of injecting groundwater mixed with acetate and bromide amendment targeting a field concentration of 5 mM were followed by 9 days of groundwater injection without amendment, then followed by another 14 days of injection of the initial amendment, before finishing with 59 days of enhanced acetate injection targeting 15 mM acetate field concentrations.

**Table 3.8.** 2008 Big Rusty schedule of amendment concentrations.

| START DAY | START DATE | END DAY | END DATE | ACETATE /BROMIDE CONCENTRATION IN TANK |
|---|---|---|---|---|
| 0 | 7/20/2008 | 14 | 8/3/2008 | 50 mM / 13 mM |
| 15 | 8/4/2008 | 23 | 8/12/2008 | 0 mM / 0 mM |
| 24 | 8/13/2008 | 37 | 8/26/2008 | 50 mM / 13 mM |
| 38 | 8/27/2008 | 53 | 9/11/2008 | 150 mM / 13 mM |
| 57 | 9/15/2008 | 72 | 9/30/2008 | 150 mM / 13 mM |
| 73 | 10/1/2008 | 89 | 10/16/2008 | 150 mM / 13 mM |
| 90 | 10/17/2008 | 96 | 10/23/2008 | 150 mM / 13 mM |

For the one-dimensional, saturated reactive transport simulations, the injection gallery was modeled as the upgradient boundary (Figure 3.1). At this boundary, the injectate was assumed to be completely mixed over the saturated thickness and injection gallery width. Boundary conditions for Fe(II), sulfate, and U(VI) were interpolated from field measurements at upgradient wells. The initial conditions for pH, carbonate, $Ca^{2+}$, $Mg^{2+}$, $K^{+}$ and $Na^{+}$ are based on field measurements. $Na^{+}$ was also included in the injectate as the cation component in the acetate and bromide salts. The downgradient domain was discretized with 120 uniform 0.1-m-long grid cells.

The maximum time step for the simulation was 0.25 d, with automatic time step reduction and expansion based on numerical convergence criteria. The simulation period began with the initial acetate biostimulation on July 20, 2008.

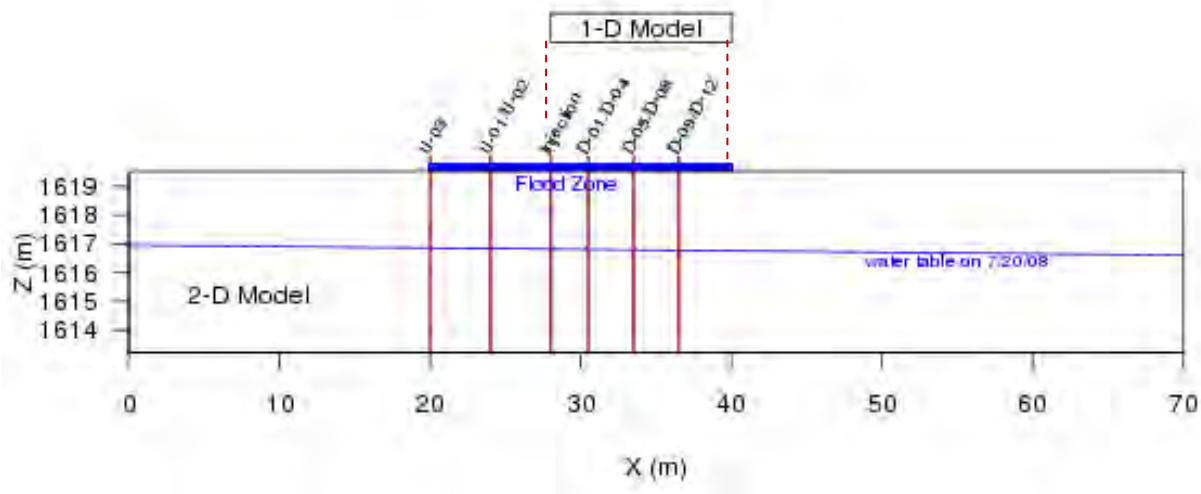


**Figure 3.1.** One-dimensional and two-dimensional modeling domains. Red vertical lines indicate upgradient (U-wells), injection gallery, and downgradient (D-wells) well locations. The one-dimensional model domain is 11.5 m long with the upgradient boundary at the injection gallery (X=28 m). Ponding at the ground surface for the flood scenario in the two-dimensional model domain is between X=20 and X=40 m.

For the baseline two-dimensional, variably saturated flow and reactive transport simulations, the vertical cross-sectional domain size is 70 m wide by 6.3 m deep (Figure 3.1). The lateral extent of the domain was significantly increased over the one-dimensional domain to accommodate the impact of the flood event on the boundary conditions. The grid size in the lateral dimension ranged from 0.25 m around the injection well to 5 m near the boundary far from the injection. The grid size in the vertical direction ranged from 0.1 m to 0.25 m. Other than the injection of acetate, sodium and bromide, which are treated as source terms in the saturated zone 28 m from the influent boundary, the initial and boundary conditions for other species are the same as those for the one-dimensional system. The simulation time step was 0.0001 hr with an acceleration factor of 1.25, and a maximum time step of 0.1 d. For the flood scenario, initial and upstream boundary conditions for dissolved oxygen were obtained from a simulation of oxygen transport that included bioreduction of oxygen using natural organic carbon as the electron donor.

## 3.4 Sensitivity Analyses

Analyses were performed targeting the sensitivity of simulated aqueous uranium concentrations to parameters in the physical, microbiological, and geochemical process models from the baseline conceptualization. Assuming that the process models are valid, the identification of the most sensitive parameters can help guide where additional care and effort in characterization activities might be warranted. For the purpose of initially identifying the sensitivity of simulation

results to model parameters, we used a one-dimensional model domain for the multicomponent biogeochemical reactive transport simulations. The first 52 days of the 2008 biostimulation experiment at the Rifle IFRC site were used as the baseline for analyzing and comparing the results of the scenarios for this study. Although biostimulation continued well beyond this time, accurate accounting of the acetate mass could not be maintained due to problems in the uniform metering of the acetate to the injection wells and changes in the groundwater flow direction.

The baseline hydraulic conductivity, porosity, and dispersivity were calibrated with downgradient monitoring well observations of bromide tracer that were injected with the acetate electron donor. The set of baseline reaction modeling parameters were developed using observations from the 2002, 2003, 2007, and 2008 biostimulation field experiments. Initial and boundary conditions for hydrology and geochemistry were based on observations from upgradient and downgradient monitoring wells.

### 3.4.1 Baseline

For the sensitivity analyses, the baseline for comparison is the application of the one-dimensional reactive transport model to the 2008 biostimulation experiment. During this experiment, water chemistry was monitored in 12 downgradient wells arranged in three rows of four wells each, 2.5 m, 5.0 m, and 8.5 m from the injection well gallery (Figure 2.2). In Figure 3.2, simulated acetate and U(VI) are plotted with observations from the monitoring well network. The modeled acetate generally reflects the pulsed loading (Table 3.8) delivered to the injection wells and compares more favorably with the observations over the first 30 days than the following 30 days. With the initiation of biostimulation, the bioreduction of U(VI) immediately begins to lower U(VI) concentrations. U(VI) removal from groundwater continues to increase over the first 30 days before leveling off and diminishing slightly in the next 30 days (Figure 3.2). Fe(II) gradually increases over the first 20 days, reflecting Fe(III) bioreduction, before slightly diminishing over the following 40 days (Figure 3.3). Sulfate bioreduction is not discernible until about 30 days into the biostimulation, after which sulfate concentrations begin to decrease. In general, the dynamics of aqueous Fe(II) and U(VI) are only subtly correlated with the variable acetate pulses. This moderated behavior is due, in part, to surface complexation processes, which provide a short-term restoring force for concentration changes in these aqueous components. U(VI) desorption accounts for the rise in U(VI) from day 40 to day 50, whereas the subsequent decrease in U(VI) reflects enhanced bioreduction resulting from the tripling of the acetate concentrations on day 38. Most of the sulfide becomes associated with the solid phase in subsidiary reactions with $Fe^{2+}$ (precipitating FeS) and goethite (resulting in precipitation of elemental sulfur). The significance of the sulfate reduction phase is that aqueous U(VI) concentrations increased during this period.

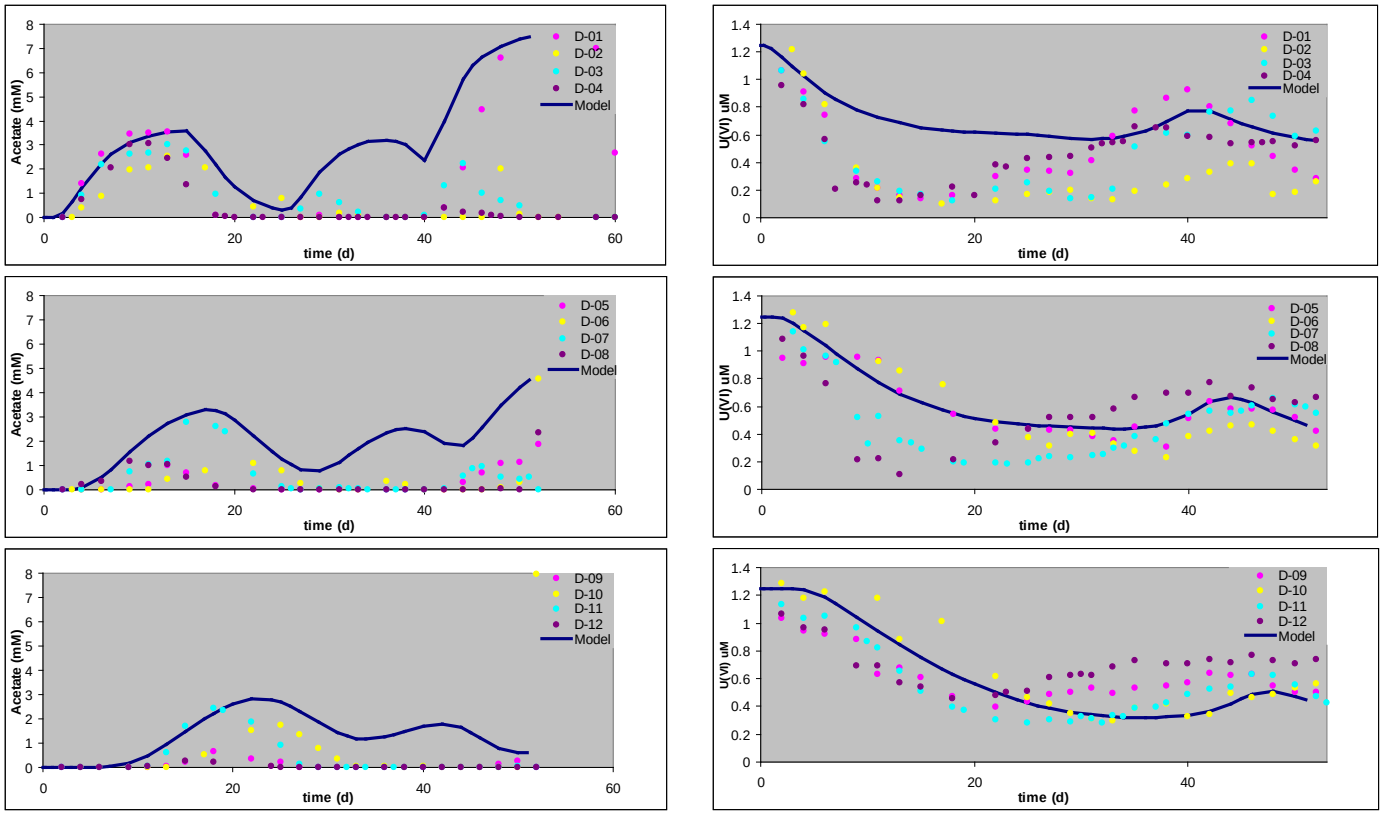


**Figure 3.2.** Simulated and observed acetate (left) and U(VI) (right) in monitoring well row 1 (2.5 m downgradient), row 2 (5.0 m downgradient), and row 3 (8.5 m downgradient).

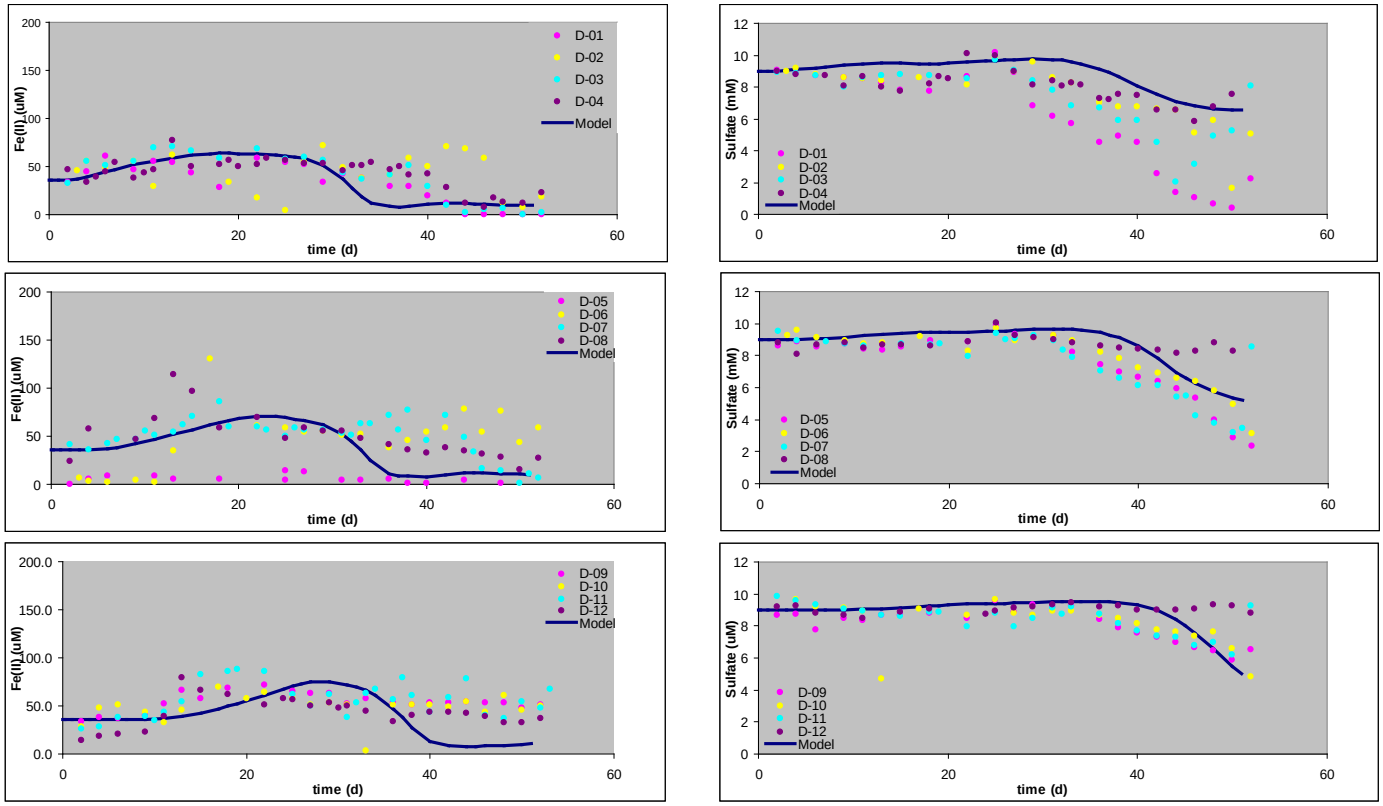


**Figure 3.3.** Temporal aqueous Fe(II) (left) and sulfate (right) at 2.5m (top), 5.0m (center) and 8.5 m (bottom) downgradient from injection gallery

### 3.4.2 Parameter Selection

The deviation of aqueous uranium behavior from the simulated baseline behavior was used as the indicator of sensitivity to a model parameter. Selected parameters (Table 3.9) were individually perturbed to identify sensitivity. The physical process modeling parameters tested were flow rate, porosity, and dispersivity; the microbiological process modeling parameters tested were the initial sulfate biomass, uranium bioreduction rate, sulfate bioreduction rate, and biomass decay rate; and geochemical process modeling parameters tested were initial aqueous uranium, surface complexation site density, and pH. In general, the sensitivity analyses involved adding and subtracting 15% from the calibrated baseline values. The exceptions were pH, porosity and dispersivity, which used end member values observed at the Rifle IFRC site. The complete set of plots for the sensitivity analyses can be found in Appendix A. Those that are reproduced in this section represent the most sensitive model parameters with respect to predicted aqueous uranium concentrations.

**Table 3.9.** Perturbation of model parameters for sensitivity analyses.

| Model Parameter | Low Value | High Value |
|---|---|---|
| Flow rate | $0.067 m^3/m^2/d$ | $0.091 m^3/m^2/d$ |
| Porosity | 0.1 | 0.1725 |
| Dispersivity | 0.4 m | 0.70 m |
| Initial Sulfate Biomass | $2.55 \times 10^{-9}$ mol/L | $3.45 \times 10^{-9}$ mol/L |
| U bioreduction rate | 2.125E-6 mol/d | 2.875E-6 mol/d |
| Sulfate bioreduction rate | 76.5 1/d | 103.5 1/d |
| Biomass decay rate | 0.01275 1/d | 0.01725 1/d |
| Initial U(VI) | 2.295E-6 mol/L | 3.105E-6 mol/L |
| pH | 6.8 | 7.4 |
| Site density | $3.264 \mu mol/m^2$ | $4.416 \mu mol/m^2$ |

### 3.4.3 Hydrologic Model

Results of the sensitivity analyses are shown in Figures 3.4 through 3.10. In the case of the U(VI) TEAP, the intrinsic rate has a direct impact on the magnitude of the aqueous uranium concentrations (i.e., higher intrinsic rate results in higher uranium removal from groundwater). Of the hydrologic parameters that were tested, the perturbations in the flow rate had the largest impacts on the predicted aqueous uranium concentrations (Figure 3.4). This is because the flow rate affects 1) the influx of groundwater, which controls the *in situ* concentration of injected amendments; 2) the supply of chemical components in the influent groundwater, which controls the availability of reactants; and 3) the transport of the electron donor and the aqueous byproducts of reactions.

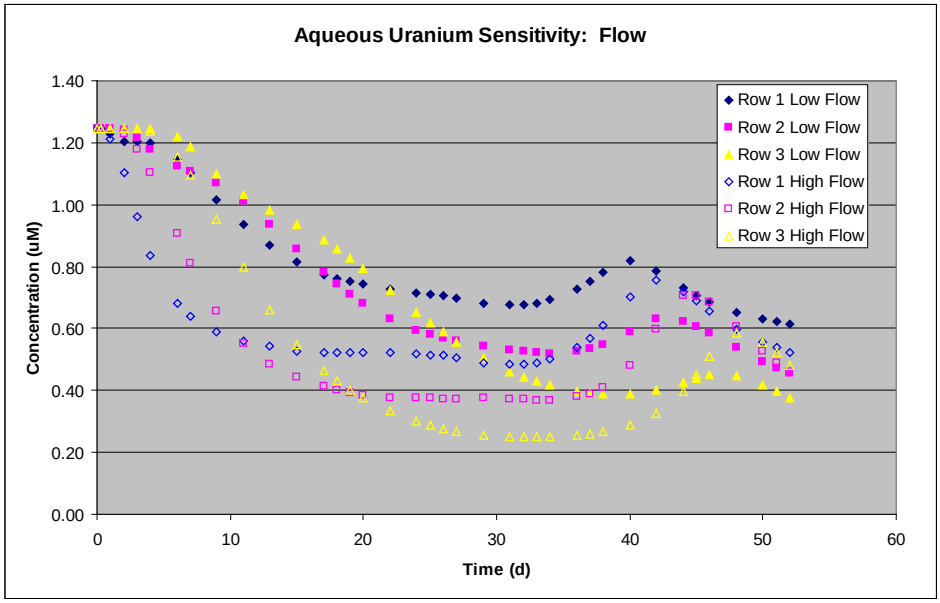


**Figure 3.4.** Aqueous uranium sensitivity to flow rates 2.5 m (diamonds), 5.0 m (squares), and 8.5 m (triangles) downgradient from the injection gallery.

For biostimulation in advection-dominant systems, the porosity affects the timing of acetate arrival at downgradient locations. While the impact of porosity perturbation on aqueous uranium concentrations is considerably smaller than that of the flow rate, it is instructive to understand the interplay of transport rates and TEAP reaction rates that determine the location and magnitude of the mobile TEAP reactants and products. For example, as advection decreases with higher porosity, there is increased residence time which equates to more time for acetate reaction. This can result in more TEAP products nearer the acetate injection point, which can be associated with increased rates of uranium bioreduction (Figure 3.5). Dispersivity (not shown here) was the least sensitive of the hydrologic model parameters tested with respect to the aqueous uranium concentrations. This reflects the advection-dominant nature of the reactive transport problem being simulated.

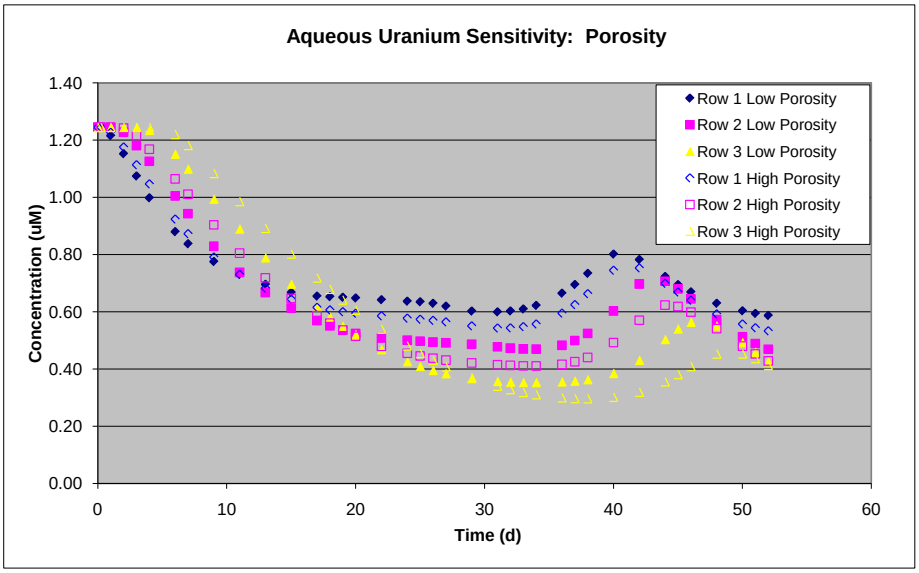


**Figure 3.5.** Aqueous uranium sensitivity to porosity 2.5 m (diamonds), 5.0 m (squares), and 8.5 m (triangles) downgradient from the injection gallery.

### 3.4.4 Biologically Mediated Reaction Model

Of the sensitivity analyses performed with the biologically mediated reaction model parameters, the simulated aqueous uranium concentrations were most sensitive to the uranium bioreduction rate. This was reflected by a deviation that grows over time between the low and high rate cases (Figure 3.6).

The deviation between the simulated aqueous uranium for low and high sulfate bioreduction cases, on the other hand, is nonexistent for the first 30 days, when Fe(III) reduction is dominant. Then as sulfate reduction becomes the dominant TEAP, the high and low sulfate bioreduction rate cases deviate significantly. The high rate result exhibits a rebound in simulated aqueous uranium concentrations that is 10 days earlier and larger than the low rate case (Figure 3.7).

The simulated aqueous uranium concentrations were generally insensitive to the perturbation of the other parameters in the sulfate TEAP rate law: initial SRB biomass and decay rate of the SRB biomass. While these parameters are important to the timing of the succession of the sulfate TEAP, 15% perturbations were not sufficient to significantly affect aqueous U(VI) concentrations.

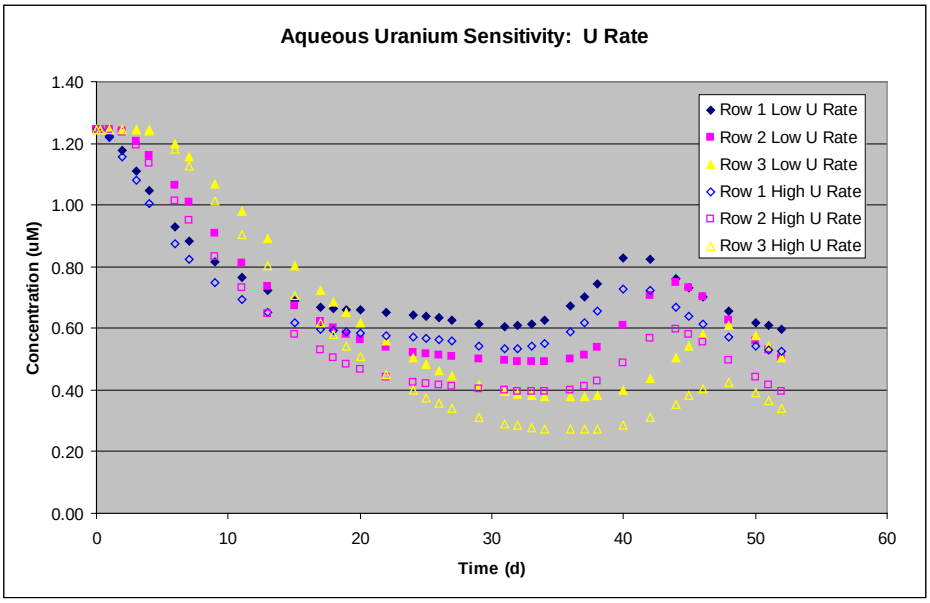


**Figure 3.6.** Aqueous uranium sensitivity to U(VI) bioreduction rate 2.5 m (diamonds), 5.0 m (squares), and 8.5 m (triangles) downgradient from the injection gallery.

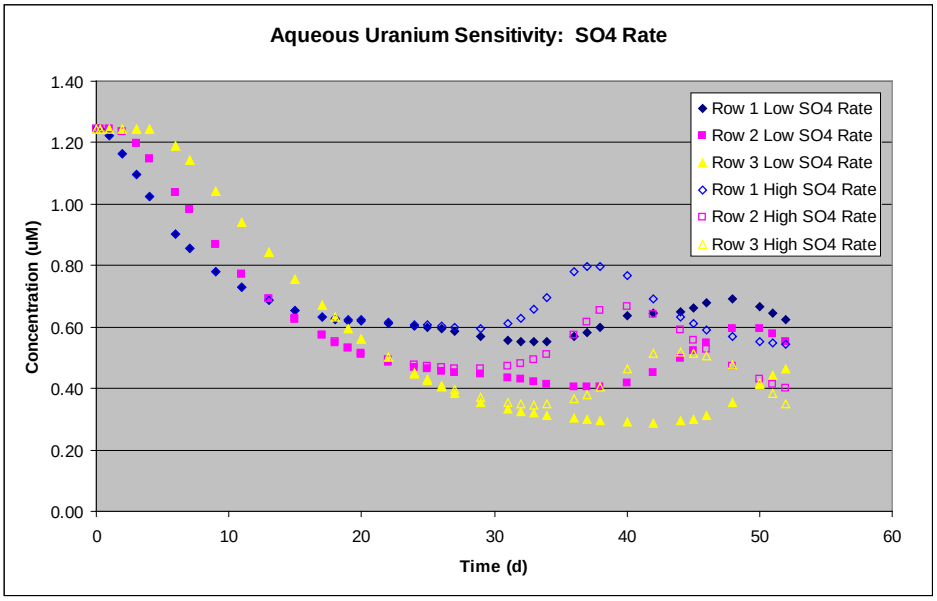


**Figure 3.7.** Aqueous uranium sensitivity to sulfate bioreduction rate 2.5 m (diamonds), 5.0 m (squares), and 8.5 m (triangles) downgradient from the injection gallery.

### 3.4.5 Geochemical Reaction Model

The principal geochemical control on aqueous uranium concentrations is through the uranium surface complexation model. Of the geochemical conditions tested in the sensitivity analyses, the largest differences in aqueous uranium concentrations were seen between the end member cases with pHs of 6.8 and 7.4 (Figure 3.8). This is not a large pH range yet deviations between the cases are initially large and become smaller with time before getting large again after sulfate reduction becomes dominant. Deviations during sulfate reduction for simulated days 40 to 50, grow larger with distance from the injection gallery. Under ambient Rifle aquifer water chemistry, the uranium surface complexation model responds to higher pH (e.g., slight elevation due to sulfide-goethite reaction) with higher aqueous U(VI) concentrations. Since the sensitivity analysis perturbed the initial pH, the higher pH case is associated with higher initial aqueous uranium concentrations. During sulfate reduction, increases in bicarbonate and pH result in U(VI) desorption. The magnitude of this desorption event is sensitive to the initial pH: the high pH case results in lower aqueous uranium concentrations during sulfate reduction because there is less U(VI) partitioned to the solid phase. Conversely, the lower initial pH case results in higher adsorbed uranium concentrations that can partition to the aqueous phase during the desorption event associated with the height of sulfate reduction.

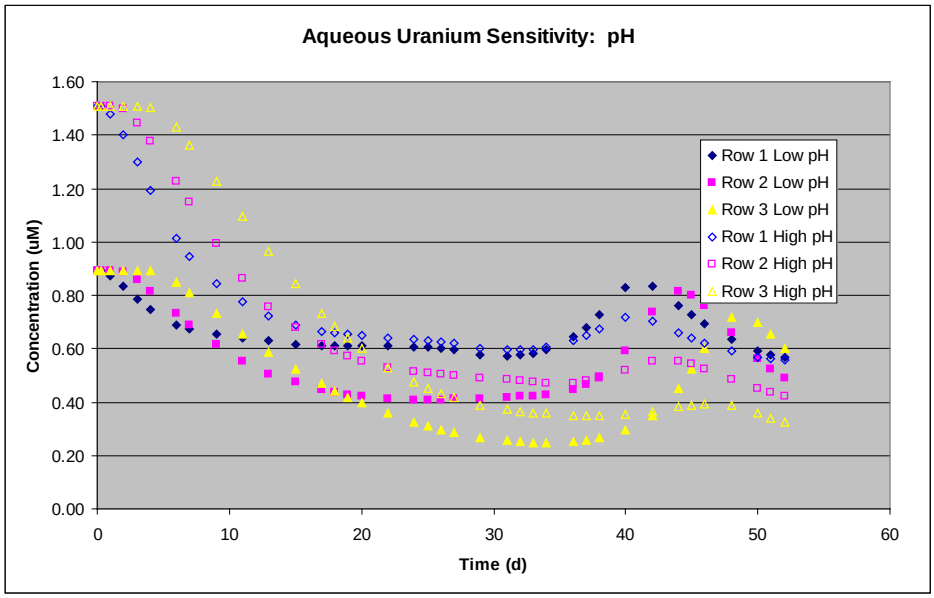


**Figure 3.8.** Aqueous uranium sensitivity to pH 2.5 m (diamonds), 5.0 m (squares), and 8.5 m (triangles) downgradient from the injection gallery.

A similar but smaller sensitivity is exhibited by the perturbation of uranium surface complexation site density (Figure 3.9). In this case the most significant deviation is in the initial aqueous uranium concentrations, where the low site density is associated with higher aqueous uranium concentrations. The two cases generally coalesce from day 20 to 40 before a very minor crossover, whereupon the high site densities have more uranium to desorb, elevating the aqueous uranium concentrations.

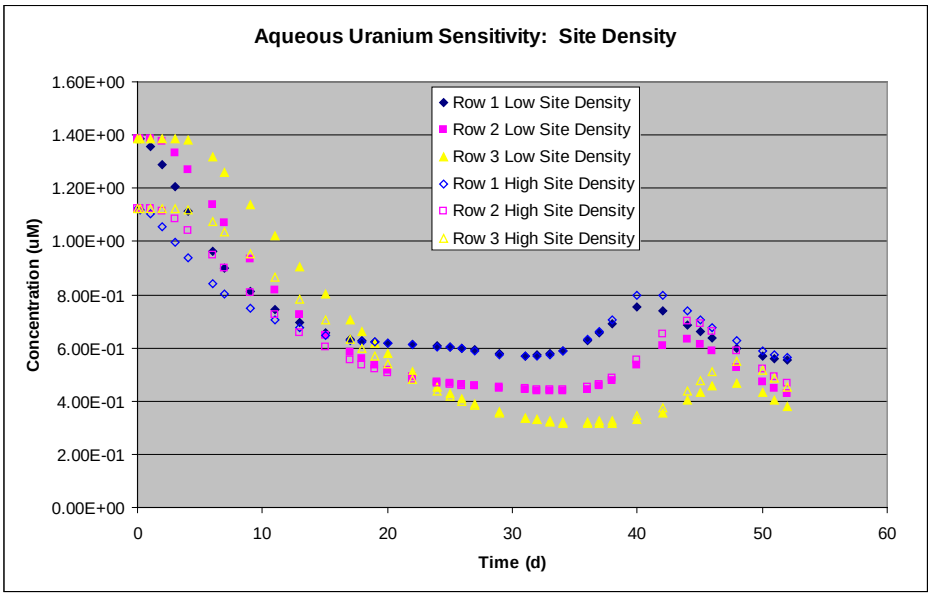


**Figure 3.9.** Aqueous uranium sensitivity to site density for uranium surface complexation 2.5 m (diamonds), 5.0 m (squares), and 8.5 m (triangles) downgradient from the injection gallery.

As with the two previous geochemical conditions, the sensitivity to the initial aqueous uranium concentration is largest at time zero (Figure 3.10). However, unlike the other geochemical conditions, the system eventually responds to the influent uranium boundary condition and the high and low cases coalesce at day 30 in the first row, day 40 in the second row, and day 50 in the third row.

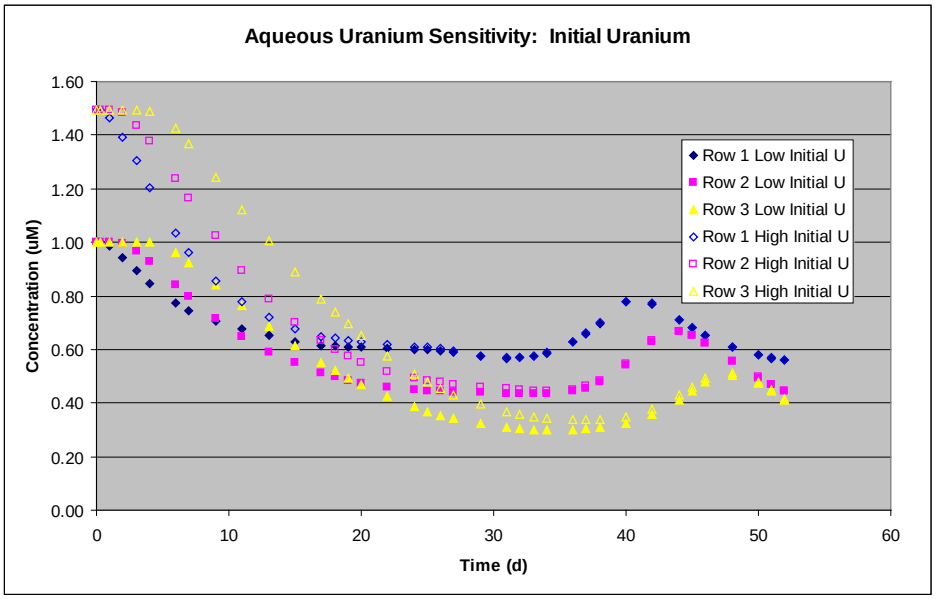


**Figure 3.10.** Aqueous uranium sensitivity to initial U(VI) concentration 2.5 m (diamonds), 5.0 m (squares), and 8.5 m (triangles) downgradient from the injection gallery.

# 4 Modeling Scenarios

## 4.1 Additional Electron Acceptors

The groundwater at the Rifle IFRC site is sufficiently low in dissolved oxygen (~0.2 mg/L) and nitrate (~0.2 mg/L) that these species are not included in the biogeochemical reaction network. However, other sites may have one or both of these components present in the groundwater. Accordingly, we added these two TEAPs to the simulation capability to address scenarios where oxygen and/or nitrate may be present. The stoichiometry of these reactions is based on the assumption of a biomass molecular formula of $C_5H_7O_2N$, the presence of an $O_2$-reducing microorganism, and an energy transfer efficiency value of 0.6 (Rittman and McCarty 2001). For acetate electron donor, the oxygen TEAP reaction is:

$$0.125\ CH_3COO^- + 0.02904\ NH_4^+ + 0.10481\ O_2 = 0.02904\ BM_O_2 + 0.00885H^+ + 0.08711H_2O + 0.10481HCO_3^- \quad (4.1)$$

Similar assumptions can be made for the presence of nitrate-reducing bacteria such that the nitrate TEAP reaction is:

$$0.125\ CH_3COO^- + 0.01329\ NH_4^+ + 0.36713\ NO_3^- = 0.01329\ BM_NO_3 + 0.07185\ H^+ + 0.03986H_2O + 0.18357HCO_3^- + 0.36713NO_2^- \quad (4.2)$$

Nitrite, an intermediate product of nitrate reduction has been shown to be a more efficient oxidizer of uraninite than nitrate (Wan et al., 2005). Accordingly, we also include the corresponding nitrite reaction:

$$0.125\ CH_3COO^- + 0.18565H^+ + 0.1128H_2O + 0.13832NO_2^- = 0.00851BM_NO_2 + 0.20747HCO_3^- + 0.12981NH4^+ \quad (4.3)$$

Since we have not calibrated the rates for these reactions at the Rifle IFRC site, we assumed a simple rate law

$$\begin{aligned} R&=k[Ac][O_2] \\ R&=k[Ac][NO_3^-] \\ R&=k[Ac][NO_2^-] \end{aligned} \quad (4.4)$$

where k=2000/d/M.

Figure 4.1 shows the hypothetical behavior of the oxygen and U(VI) TEAPs using the 2008 Big Rusty experiment baseline model under the assumption of a background level of dissolved oxygen near saturation with atmospheric oxygen, 250 umol/L. Dissolved oxygen is essentially depleted during each of the two 2-week periods of 5 mM acetate biostimulation. The rebound in oxygen after two weeks is due to the 9-day interruption in amendment delivery that separated the two 2-week biostimulation periods. As modeled in this scenario, the impact of the dissolved oxygen on U(VI) and other TEAP processes is minimal as they are indistinguishable from the baseline results.

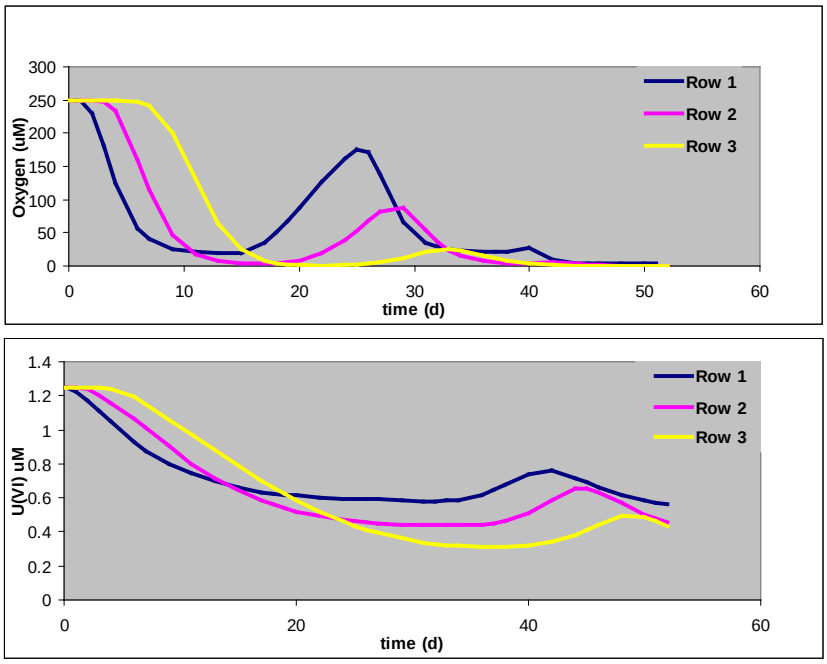


**Figure 4.1.** Dissolved oxygen (top) and aqueous U(VI) (bottom) during acetate biostimulation in downgradient monitoring row 1 (2.5 m), row 2 (5.0 m), and row 3 (8.5 m).

Similarly, the hypothetical inclusion of the nitrate TEAP into the 2008 Big Rusty baseline model was performed with an initial nitrate concentration of 130 µmol/L, which has been observed in another alluvial aquifer of interest. In this case, the stoichiometric conversion of nitrate per mole of acetate consumed is 3 times that of oxygen (Equation 4.1 and 4.2). This results in a relatively faster depletion of nitrate (Figure 4.2). As with the dissolved oxygen case, the U(VI) and other TEAP processes are essentially identical to the baseline.

In both cases, acetate was non-limiting as the removal of oxygen and nitrate was generally complete. The stoichiometry suggests that 0.3 mM acetate is necessary to remove oxygen, whereas 0.044 mM acetate is necessary to remove nitrate. While the overall impact of oxygen and nitrate to the uranium bioremediation appears to be minimal, the continuous influx of oxidizers into the treatment zone can be detrimental to the stability of immobilized uranium and must be addressed.

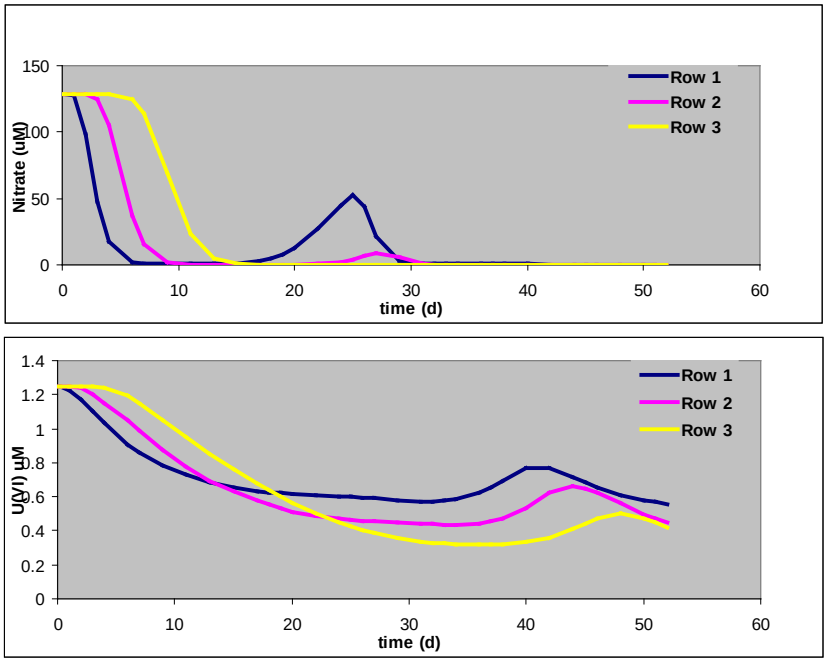


**Figure 4.2.** Nitrate (top) and U(VI) (bottom) during acetate biostimulation in downgradient monitoring row 1 (2.5 m), row 2 (5.0 m), and row 3 (8.5 m).

## 4.2 Additional Electron Donors

At the Rifle IFRC site, only acetate has been used as the electron donor for large-scale field experiments. Lactate and ethanol are other possible electron donors that have been used at other sites (e.g., Wu et al. 2005). We added lactate and ethanol reactions for our primary TEAPs once again following the Rittman and McCarty approach described earlier.

<u>Lactate + sulfate</u>:

$$0.25\ CH_3CHOHCOO^- + 0.01562\ NH_4^+ + 0.08595\ SO_4^{--} = 0.01562\ BM_lac + 0.25\ CH_3COO^- + 0.10157\ H^+ + 0.04686\ H_2O + 0.17190\ HCO_3^- + 0.08595\ HS^- \quad (4.5)$$

<u>Lactate + uranium</u>:

$$0.25\ CH_3CHOHCOO^- + 0.24084\ H_2O + 0.01994\ NH_4^+ + 0.30065\ UO_2^{++} = 0.01994\ BM_iron + 0.25\ CH_3COO^- + 0.77156H^+ + 0.15032\ HCO_3^- + 0.30065\ UO_2(s) \quad (4.6)$$

Lactate + phyllosilicate iron:

$$0.25\ CH_3CHOHCOO^- + Fe(III)(ls) + 0.5\ H_2O = 0.25\ CH_3COO^- + 0.25\ HCO_3^- + 1.25\ H^+ + 0.9\ Fe(II)(ls) + 0.1\ Fe^{++} \quad (4.7)$$

Ethanol + sulfate:

$$0.25\ CH_3CH_2OH + 0.0568HCO_3^- + 0.0923SO_4^{--} = 0.25CH_3COO^- + 0.1009H^+ + 0.267H_2O + 0.0923HS^- + 0.0114SO_4RM_cell \quad (4.8)$$

Ethanol + uranium:

$$0.25\ CH_3CH_2OH + 0.2161\ H_2O + 0.47\ UO_2(CO3)_2^{--} = 0.25\ CH_3COO^- + 0.0026\ DRM3_cell + 0.2370\ H^+ + 0.9270\ HCO_3^- + 0.47\ UO_2(s) \quad (4.9)$$

Ethanol + phyllosilicate iron:

$$CH_3CH_2OH + 4\ Fe(III) + 7\ H^+ = CH_3COO^- + 3.6\ Fe(II)(ls) + 0.4\ Fe(II)(aq) + 7\ H_2O \quad (4.10)$$

Note that acetate is a product of all these reactions, which allows all the acetate baseline TEAP reactions to continue to be used in these analyses, albeit as subsidiary reactions dependent on lactate and ethanol oxidation. In the absence of rates for these TEAPs with sediments and groundwater from the Rifle IFRC site, we assume the same rate laws and parameters that were used in the baseline acetate-mediated TEAPs. In these simulations of the hypothetical inclusion of lactate and ethanol, we assumed the target electron donor concentrations were the same as the acetate in the baseline (5 mM and 15 mM).

For the lactate electron donor simulation, lactate is seen to be depleted relatively quickly and the second 5 mM pulse is not evident (Figure 4.3). Lactate does reappear after the electron donor concentration was tripled (day 38) but is completely consumed prior to reaching the third row of monitoring wells. U(VI) is bioreduced more slowly, appears to be mildly responsive to the electron donor pulses, and does not have an obvious increase during sulfate reduction as is seen in the baseline.

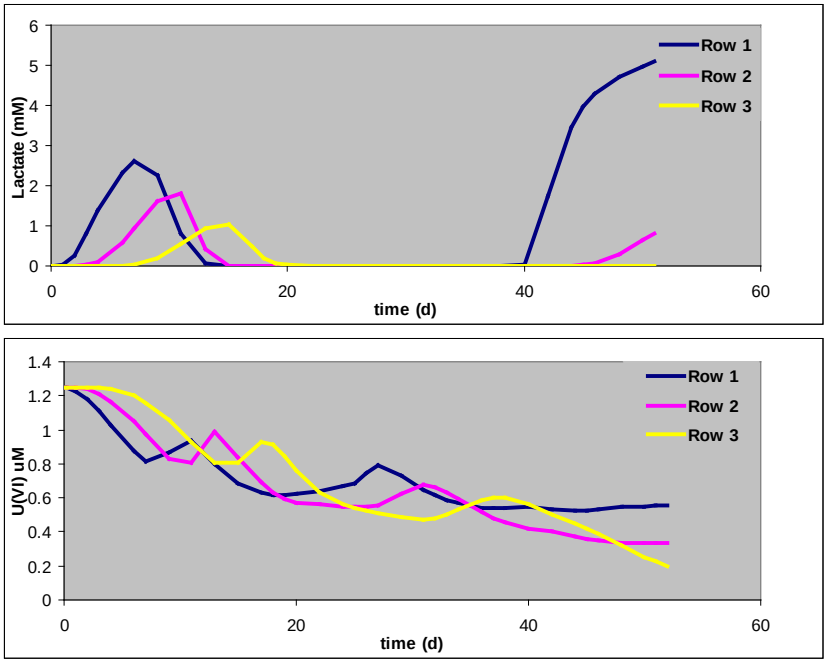


**Figure 4.3.** Lactate electron donor simulation: lactate (top) and U(VI) (bottom) concentrations in downgradient monitoring rows 1 (2.5 m), 2 (5.0 m), and 3 (8.5 m)

Similar to the lactate simulation, the hypothetical biostimulation with ethanol leads to generally complete consumption of ethanol in 2 to 3 weeks before appearing again after day 38 when the electron donor loading was tripled (Figure 4.4). After an initial decline over the first 2 to 3 weeks, the U(VI) in this case bottoms out and rebounds slightly. It should be mentioned that differences in the simulated TEAP behaviors from the baseline are strictly due to differences in reaction stoichiometries that are unique to each electron donor. This explanation is possible only because the same rate laws and parameters as the baseline are being used.

Finally, it should be noted that these results are based on reactions from the literature with hypothetical rates. Thus, the simulated field behavior based on these reactions and rates have not been confirmed through field observations. We use these simulations to identify that other electron donor – electron acceptor – microorganism combinations are possible and the expectation is that the resulting behavior will differ from the acetate biostimulation behavior.

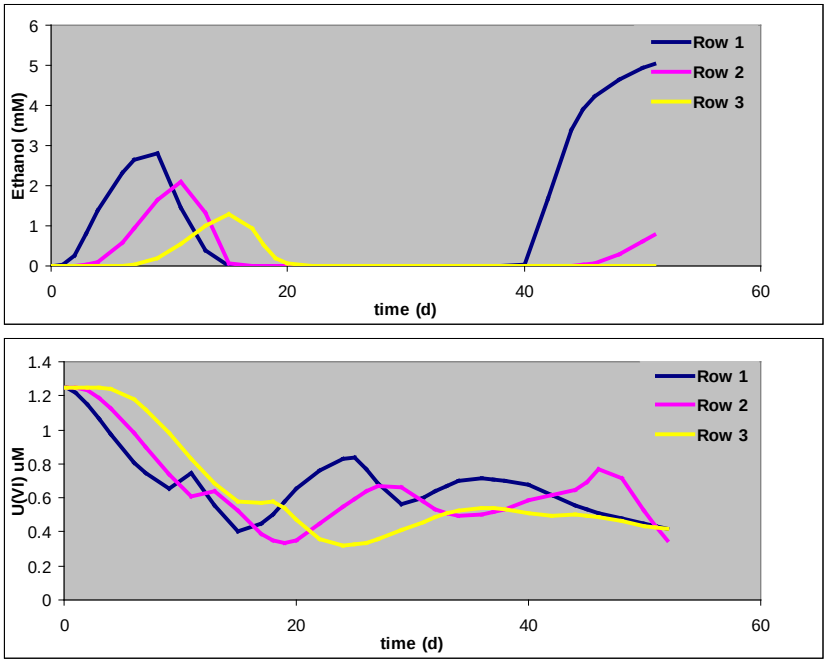


**Figure 4.4.** Ethanol electron donor simulation: ethanol (top) and U(VI) (bottom) concentrations in downgradient monitoring rows 1 (2.5 m), 2 (5.0 m), and 3 (8.5 m).

## 4.3 Two-Dimensional Baseline

### 4.3.1 Hydrologic Conditions

While the 1-D simulations allowed us to make significant progress on the biogeochemical reaction network, there are important physical processes that require a minimum of two dimensions to resolve the behaviors of interest. These include density effects and gas entrapment during water table rise and fall. A baseline 2-D variably saturated flow simulation of the 2008 Big Rusty experiment was performed to provide a basis for comparison against the hypothetical scenarios that were subsequently simulated. The 2-D baseline simulation included water table changes that reduced the saturated thickness by ~20% over the duration of the 2008 experiment (Figure 4.5).

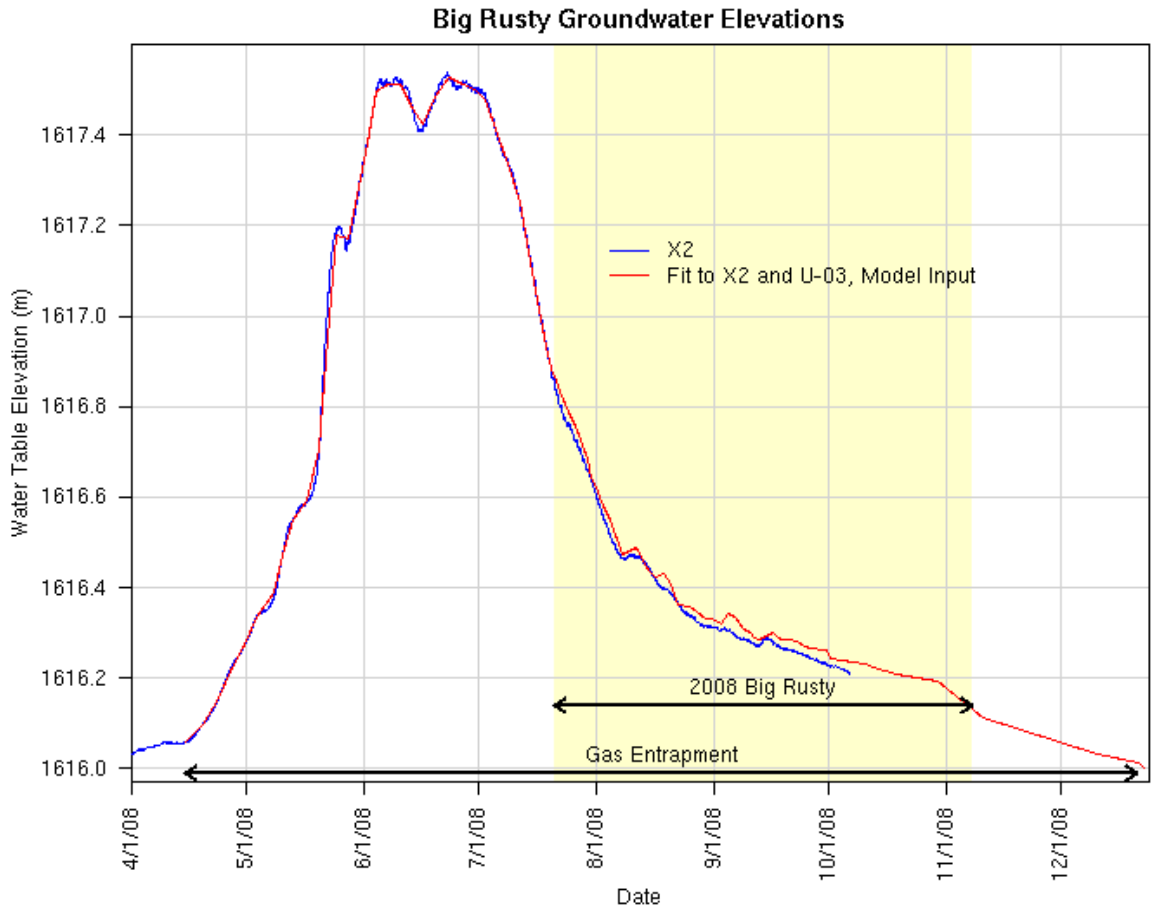


**Figure 4.5**. Rifle IFRC water table elevation during seasonal rise and fall.

The 2-D simulations generally capture the pulsed amendment release over the first 40-days of the Big Rusty field experiment. By accounting for the water table changes, these simulations are in better agreement with the observed concentrations than the 1-D simulations. As mentioned previously, we generally focus on the first part of the 2008 Big Rusty biostimulation experiment because groundwater flow direction changes and problems in the metering of the acetate evenly between the 10 injection wells resulted in significant discrepancies in injectate mass after day 38 (Figure 4.6).

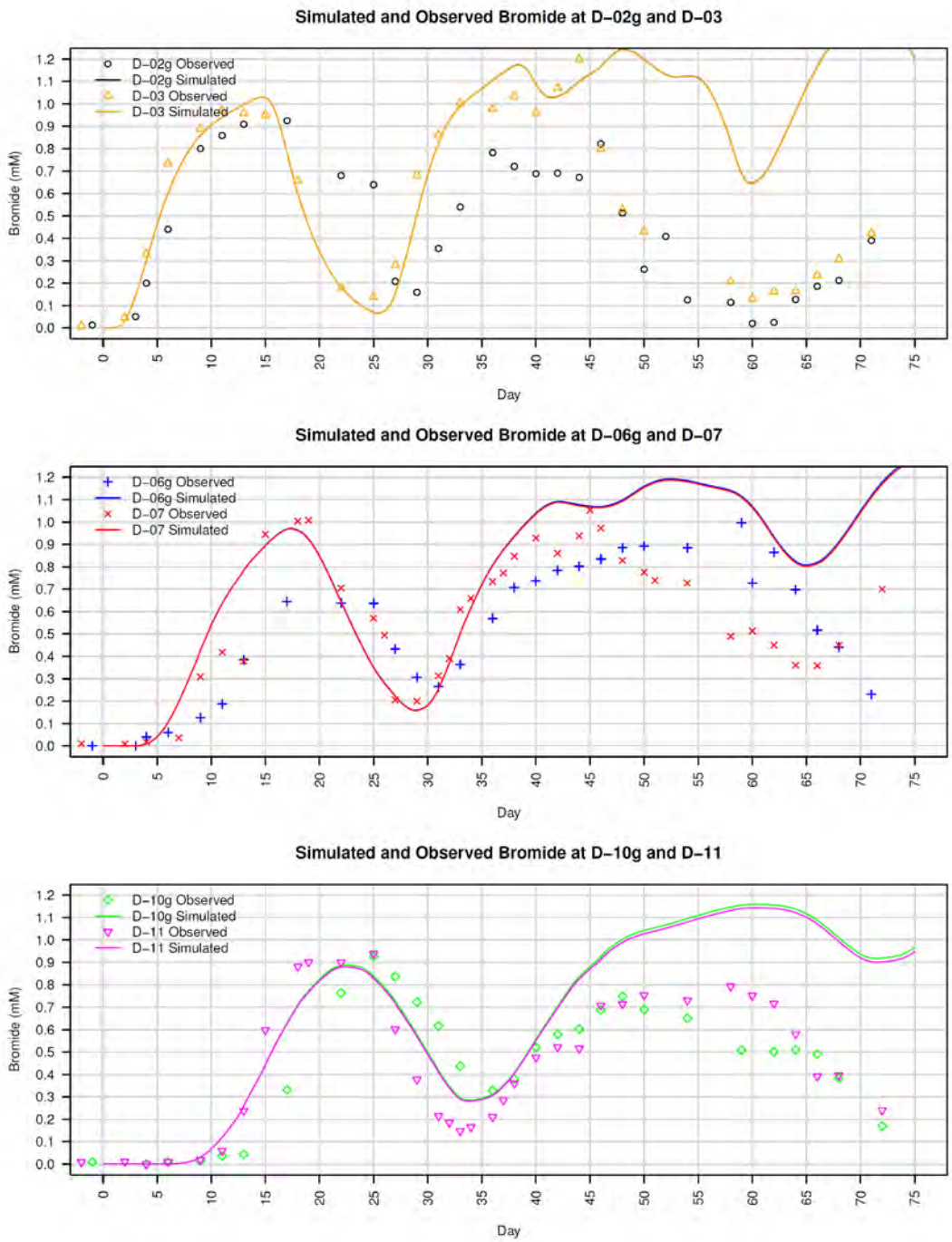


**Figure 4.6.** Comparison of simulated bromide concentrations with field observations in the downgradient monitoring well rows 2.5 m (D-02g and D-03), 5.0 m (D-06g and D-07), and 8.5 m (D-10g and D-11) downgradient from the injection gallery wells. The "g" designation for wells refers to the deepest sampling depth in the well. Note that soon after the increase in acetate concentrations on day 38 (see Table 3.10), uneven metering of amendment to the injection wells and changes in the groundwater flow direction resulted in some of the bromide not being accounted for in the downgradient monitoring wells.

The effects of the pulsed acetate injection with different concentrations can be seen in Figure 4.7. At 20 days, the initial 2-week 5 mM acetate pulse is reacting and has transported approximately 5 m downgradient from the injection wells (X=28 m). On day 30, the second acetate pulse is in the 7$^{th}$ day of injection, while the center of mass of the first pulse is approximately 12 m downgradient. On day 40, the tripling of injected acetate targeting an *in situ* 15 mM concentration has been ongoing for 2 days. The zone of enhanced acetate is expanded by approximately 5 m at 50 days with nearly complete dispersal of the first pulse. This is consistent with the ~0.5 m/d pore velocity. The front of high acetate concentrations continues to move downgradient from 60 to 100 days but oxidation is limiting the migration. The sloping water table is discernible in these results and some of the acetate is diffusing into the vadose zone. Other than the small movement into the vadose zone, the acetate is generally well-mixed in the vertical. This is true for the other reactive components and downgradient distributions are similar to the 1-D baseline results.

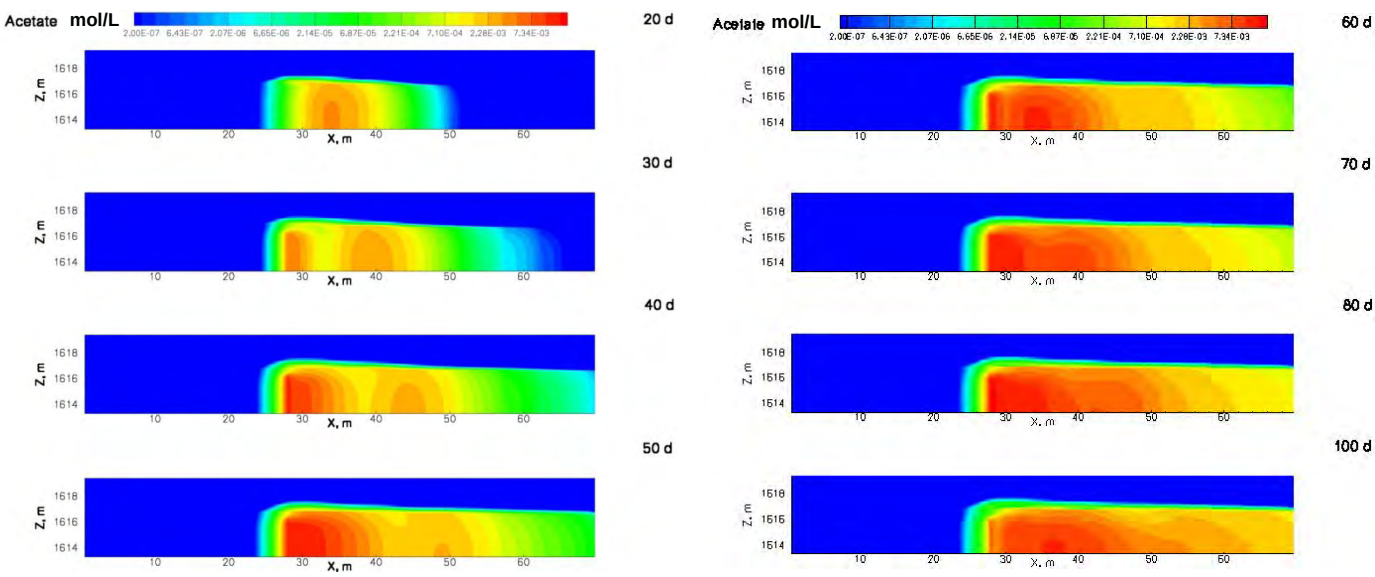


**Figure 4.7.** Simulated spatial distributions of acetate 20, 30, 40, and 50 days after start of biostimulation. Note that the injection gallery is located at X=28 m and the last row of monitoring wells is at X=36.5 m.

The lowest aqueous U(VI) concentrations are not associated with the highest acetate concentrations near the injection point but 7 m or more downgradient (Figure 4.8). This is due to the kinetics of the U(VI) TEAP reactions, whose time scales are slow relative to groundwater transport. In this case, a parcel of U(VI)-bearing groundwater is progressively depleted of U(VI) over time as it is being transported. That depletion is from the precipitation of U(IV) mineral, $UO_2$(s). Conversely, the highest concentrations of the precipitated U(IV) are found near the injection point with slightly lower concentrations downgradient (Figure 4.9). This is because the highest U(VI) and acetate concentrations are found at the injection point, which results in the highest reaction rates for this TEAP rate law.

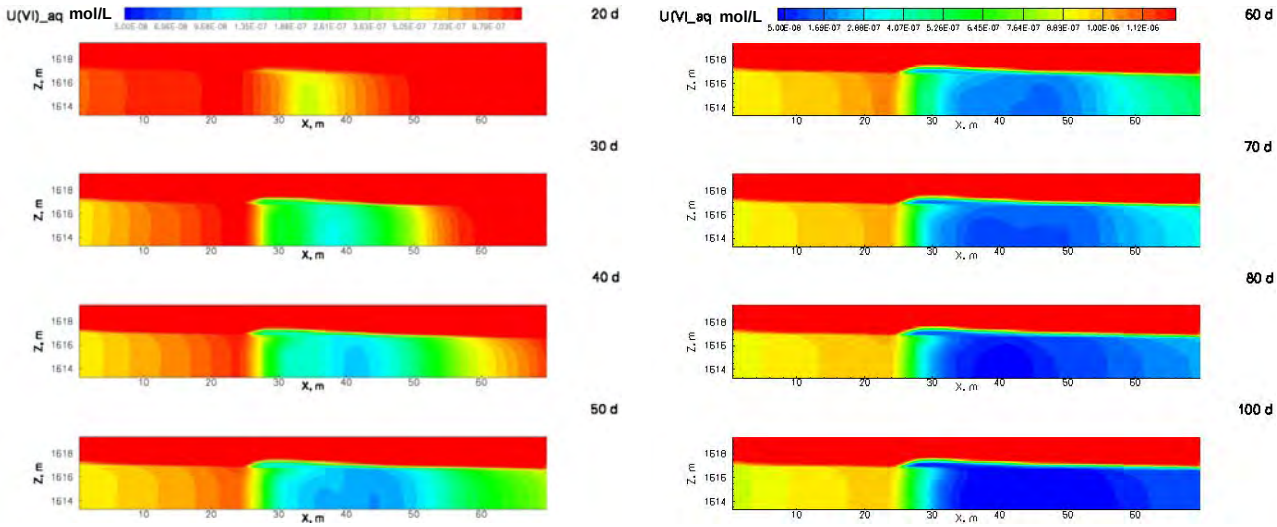


**Figure 4.8**. Simulated baseline aqueous U(VI) concentration distributions for day 20 to 100 of the biostimulation.

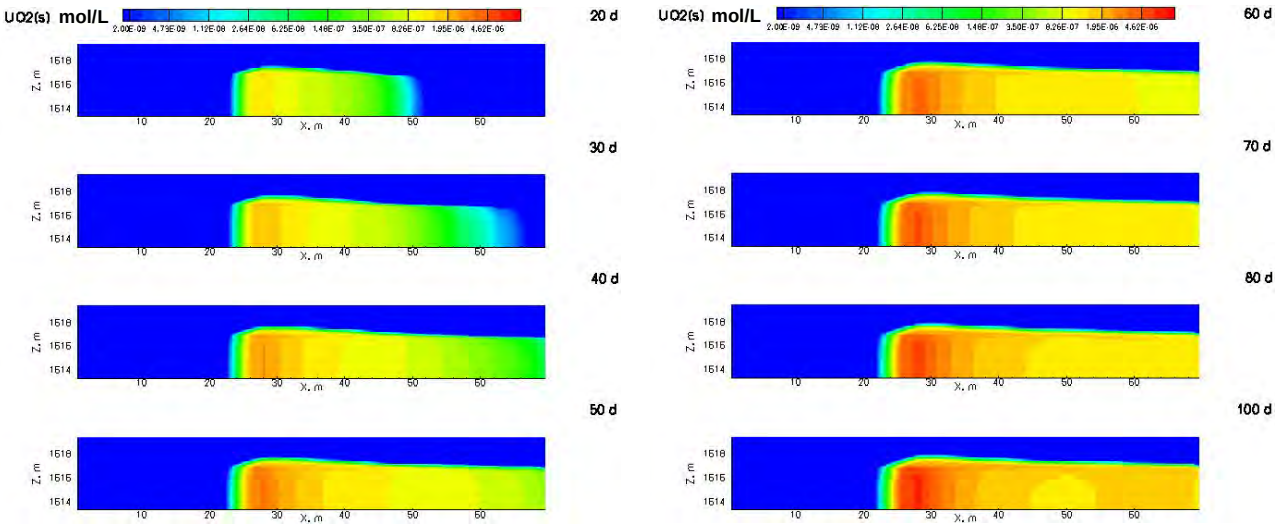


**Figure 4.9.** Simulated baseline $UO_2(s)$ concentration distributions for day 20 to 100 of the biostimulation.

The highest concentrations of aqueous Fe(II) are associated with the early 5 mM acetate biostimulation pulses prior to the dominance of sulfate reduction. In this case, it can be seen in Figure 4.10 that the peak Fe(II) concentrations are generated through 30 days of the acetate biostimulation pulses. As sulfate reduction becomes the dominant TEAP, sulfide from that reaction reacts with the Fe(II) to form iron sulfide, FeS. This results in decreased aqueous Fe(II) concentrations for the duration of the biostimulation period. The higher Fe(II) concentrations

from the early biostimulation period continue to migrate downgradient ahead of the lower Fe(II) concentrations that are associated with sulfate reduction.

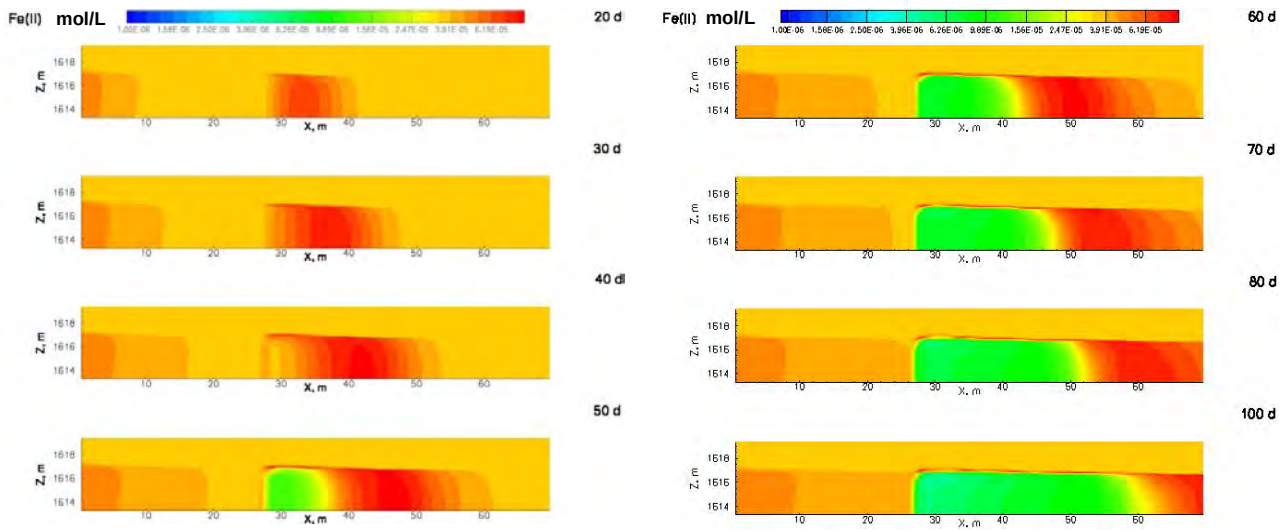


**Figure 4.10.** Simulated baseline aqueous Fe(II) concentration distributions for day 20 to 100 of the biostimulation.

In the simulation, low levels of sulfate conversion are occurring early in the biostimulation (Figure 4.11), but these changes would be imperceptible in the field given the typical variability in measured sulfate concentrations. The limited amount of sulfide generated during this time period reacts with Fe(II) to form minute amounts of FeS mineral (Figure 4.12). The dominance of the sulfate TEAP begins after ~30 days of acetate biostimulation, marked by a 1 to 2 mM decrease in sulfate concentrations near the injection point. In some respects, the decrease in previously elevated aqueous Fe(II) concentrations in Figure 4.10 is a more definitive indicator of sulfate reduction than the small amount of sulfate removal relative to the ambient ~9 mM sulfate concentrations. Similar to the biologically mediated U(VI) behavior, sulfate transported downgradient in a parcel of groundwater with acetate continues to undergo rate-limited reaction, resulting in the lowest concentrations of sulfate traveling downgradient from the injection point. This is most obvious from 50 to 100 days of the biostimulation when significant sulfate removal was occurring. Conversely, FeS begins to form near the acetate injection point and as the sulfate TEAP becomes dominant, FeS forms further downgradient. The highest FeS abundance, however, is always in the vicinity of the injection point, where the availability of Fe(II) and sulfide are the highest. As mentioned previously, the importance of the sulfate TEAP is because 1) acetate utilization can limit availablility to the FeRB responsible for U(VI) bioreduction, 2) increases in the alkalinity and pH via the bicarbonate and sulfide produced can result in U(VI) desorption, and 3) FeS can play an important role in controlling post-biostimulation uranium remobilization both as an abiotic redox control and as an electron donor for microorganisms that use dissolved oxygen as a terminal electron acceptor (e.g., oxidizers).

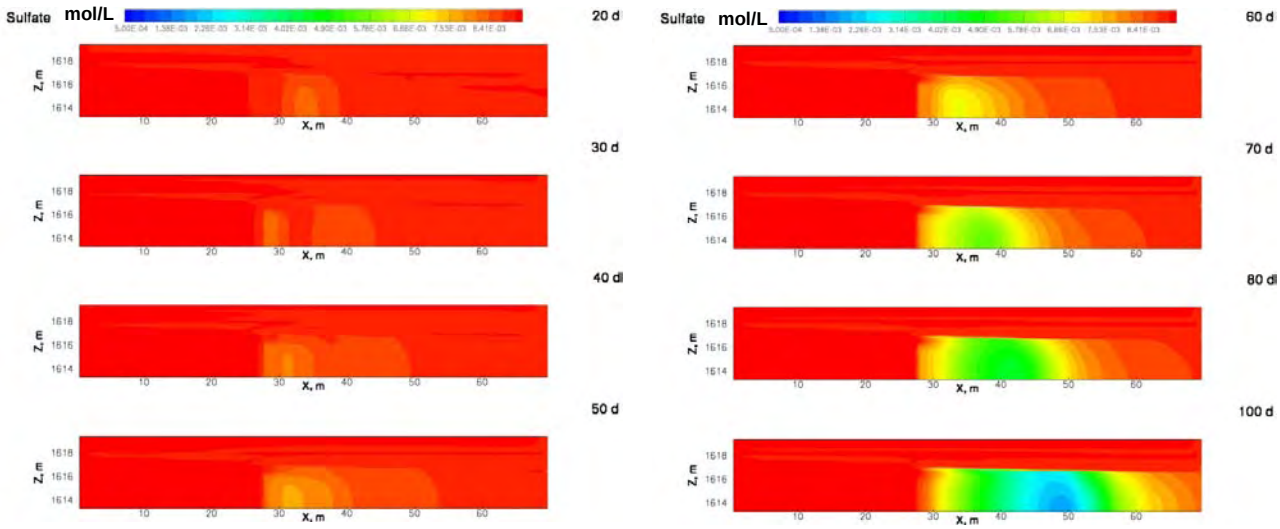


**Figure 4.11.** Simulated baseline aqueous sulfate concentration distributions for day 20 to 100 of the biostimulation.

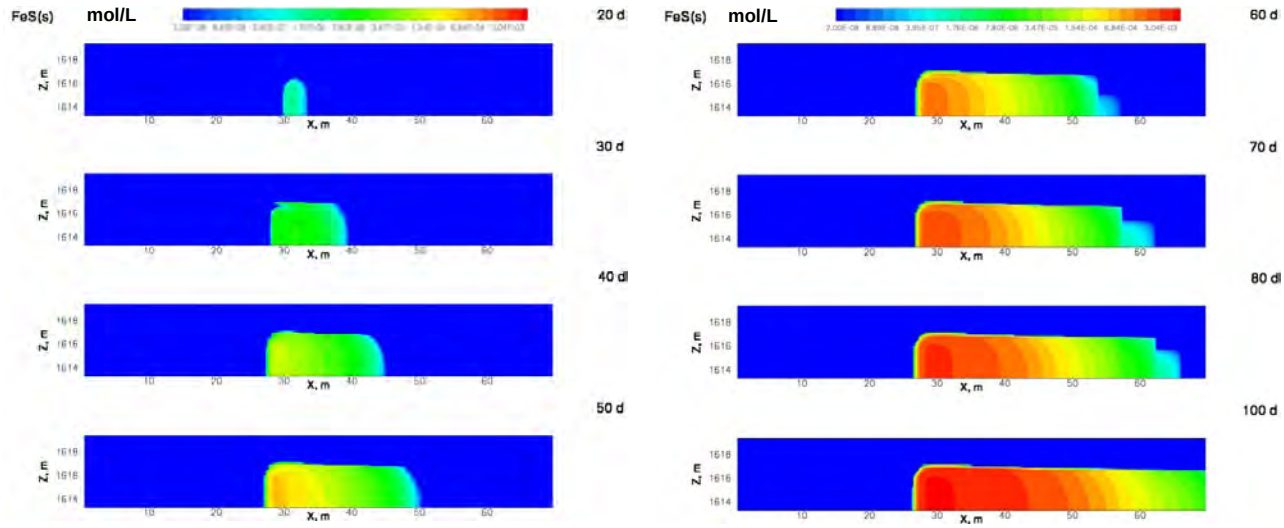


**Figure 4.12**. Simulated baseline FeS(s) concentration distributions for day 20 to 100 of the biostimulation.

### 4.3.2 Injectate Density Effects

In the 2003 Rifle field experiments, it became clear that the injectate concentrations were sufficiently high to result in density effects. In this case, the injected acetate concentrations were ~300 mM and the bromide concentrations were ~10 mM. Figure 4.13 shows the vertical distribution of acetate and bromide concentrations at locations down the centerline of the field plot from 3.7 m upgradient, B-02, to M-03, M-08, and M-13, which are 3.7, 7.3, and 14.6 m downgradient, respectively. Where acetate and bromide were detected, the acetate concentrations near the bottom of the aquifer were about 3 times higher than the shallow concentrations.

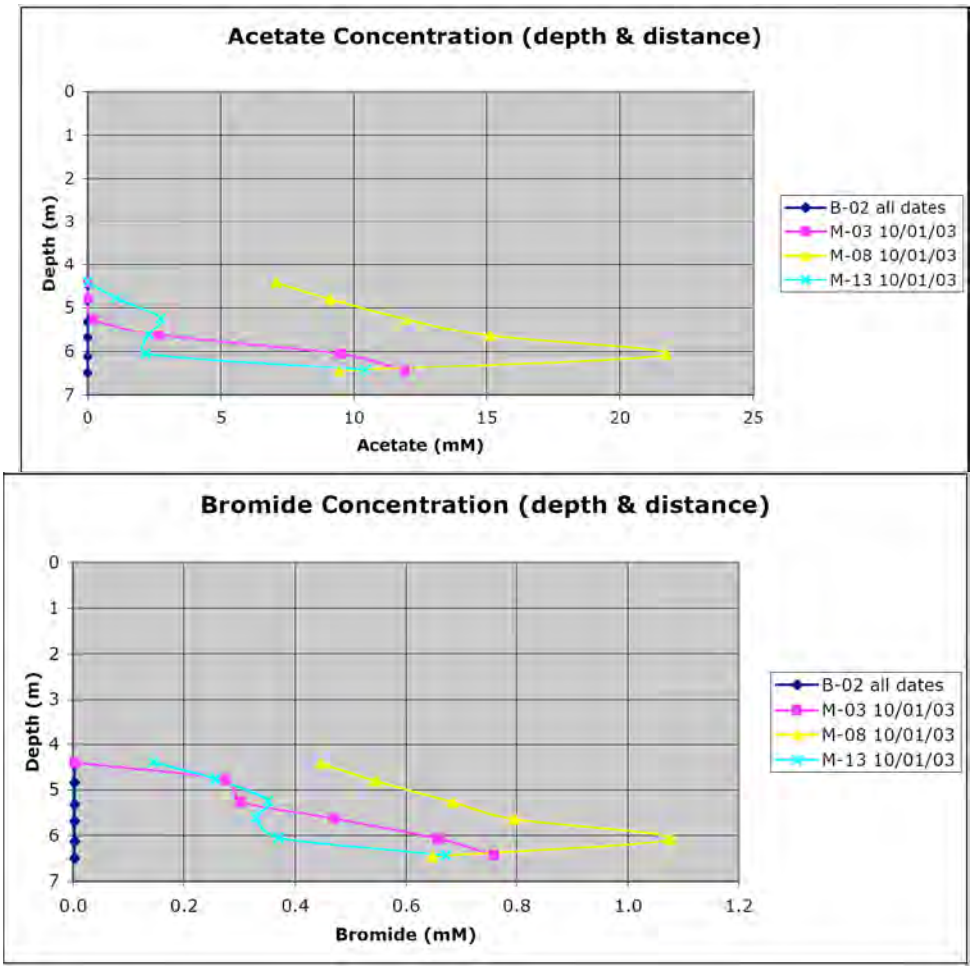


**Figure 4.13.** Acetate (top) and bromide (bottom) concentration as a function of depth on October 1, 2003.

To model this behavior, we use an equation of state that relates the fluid properties of density and viscosity to bromide and acetate concentration. This is based on 20°C data from the 2008-2009 Online CRC Handbook of Chemistry and Physics (Figure 4.14).

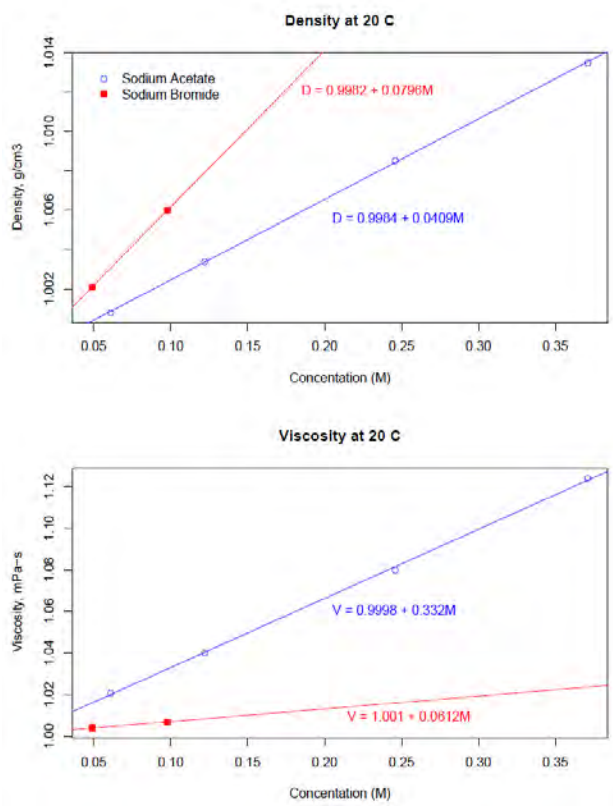


**Figure 4.14.** Density (top) and viscosity (bottom) variation with sodium acetate (blue) and sodium bromide (red) in solution.

The initial field experiments in 2002 and 2003 assumed that the injection well configuration would deliver a vertically well-mixed distribution. Note that the "injection" is actually a slow metering of a few milliliters of amendment per minute into a well at 3 depths. Observations and the 2-D simulations clearly show that immediately downgradient from the injection gallery a vertical gradient of acetate concentrations is generated (Figure 4.15).

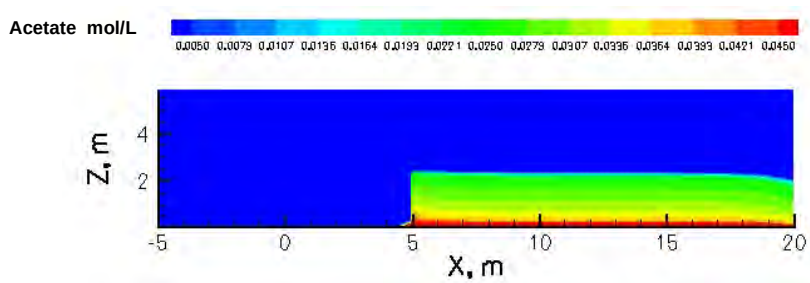


**Figure 4.15.** Simulated 2003 field experiment illustrating the potential for acetate stratification.

For this reason, subsequent large-scale experiments at the site used cross-well mixing with lower acetate concentrations and higher injection rates (Figure 4.16). Cross-well mixing between injection gallery wells (Hyndman et al., 2000) enhances mixing between injection wells without continuously modifying the natural gradient. The purpose of cross-well mixing is to spread the amendment between individual injection wells, creating a more uniformly dispersed source term along the injection gallery. It also disperses the amendment more evenly in the vertical direction, an important consideration since we know that the density contrast between groundwater and amendment resulted in higher concentrations of Br and acetate toward the bottom of the aquifer. Since the target acetate field concentrations in the 2008 Big Rusty experiment were the highest attempted at the site, we revisited the density calculations.

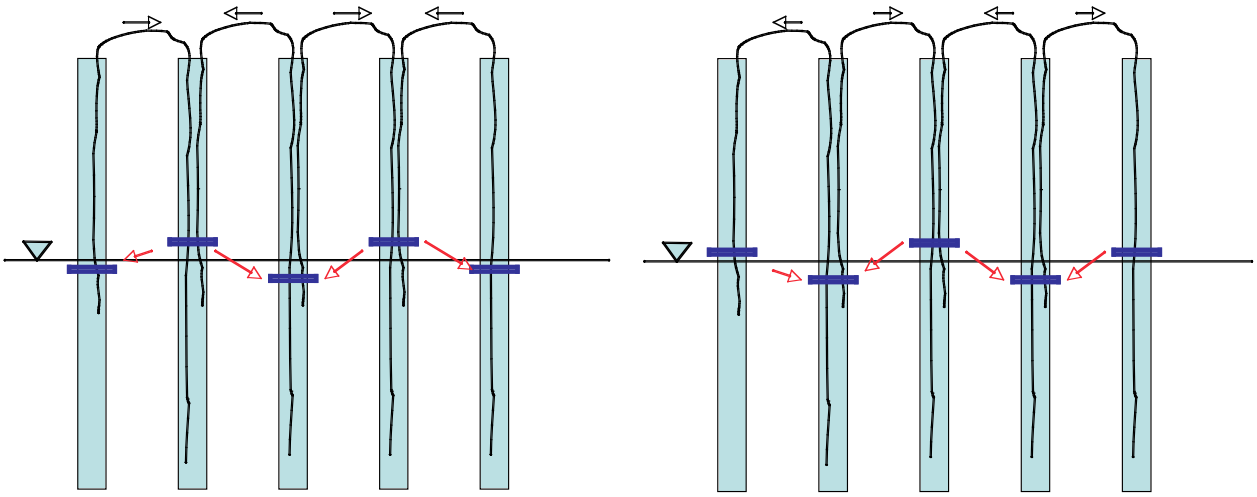

**Figure 4.16.** Cross-well mixing scheme with standard (left) and reversed (right) pumping directions. Two 2-channel peristaltic pumps are run throughout the period of injection with daily reversals. Cross-well mixing consists of two tubes, one to deep and one to shallow depths.

For the simulation of the density scenario, we use the 2008 Big Rusty biostimulation experiment baseline model parameterizations and the bromide/acetate loading schedule in Table 3.8. The variable loading allows density analyses for periods of low acetate (5 mM) amendment interrupted by a period of no amendment, followed by a prolonged period of high acetate (15 mM) amendment. We assume complete mixing in the injection wells to represent the cross-well mixing.

During the first 30 days of simulation, it is seen that the targeted 5 mM acetate concentrations in the field result in no obvious density effects (Figure 4.17). After the tripling of acetate concentrations on Day 38, there is some vertical variation in the simulated acetate concentrations for the Big Rusty experiment; however, these impacts are generally mild in comparison to the 2003 field experiment (Figure 4.15). The largest vertical variation in acetate concentration is seen on the lateral edges of individual pulses.

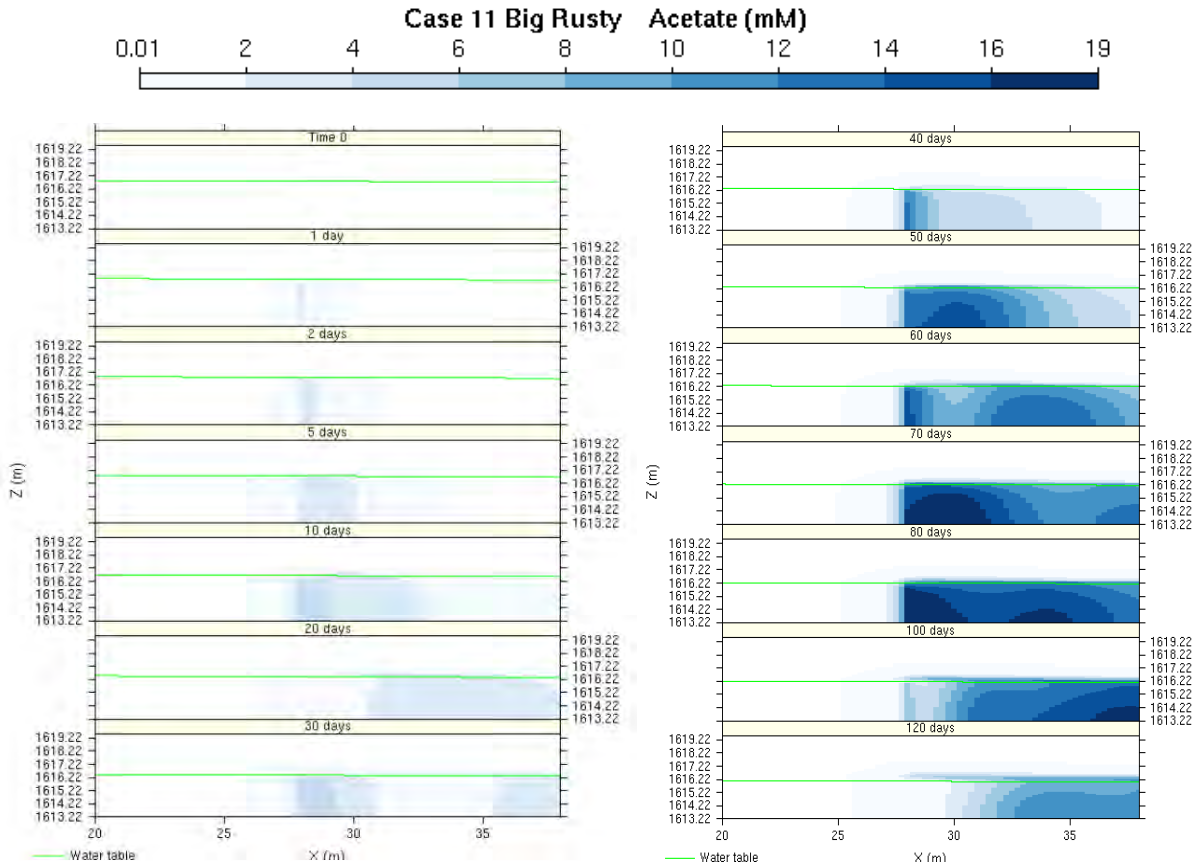


**Figure 4.17.** Simulated acetate concentrations at 0 to 120 days after the initiation of biostimulation on July 20, 2008. Note that the injection gallery is located at X=28 m and the last row of monitoring wells is at X=36.5 m.

In Figure 4.18, the vertical variation of simulated acetate at monitoring well rows 1, 2, and 3 (2.5, 5.0, and 8.5 m downgradient from the injection wells) is clearly small, even during the period where acetate concentrations were tripled (from day 38). At 30 d, the first row is experiencing acetate released at ~24 d, ~17d for row 2, and ~9 d for row 3. Because of the schedule of injections, the first and third rows are experiencing concentrations from active injection while row 2 is experiencing concentrations from the acetate interruption. A hypothetical case where the enhanced acetate injection was doubled to 300 mM was also simulated, which begins to show some vertical variation in the concentrations (Figure 4.18).

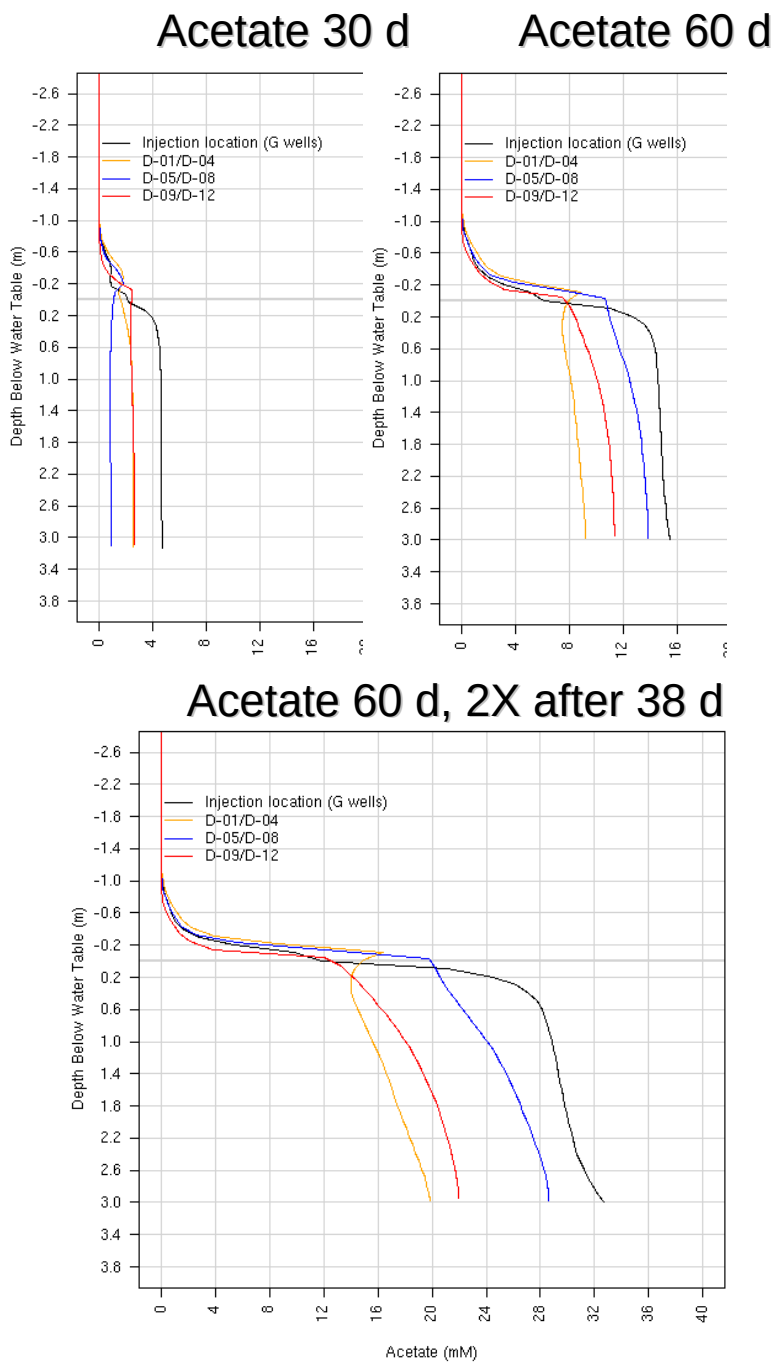


**Figure 4.18.** Simulated variation of acetate concentrations with depth after 30 and 60 days of the baseline (corresponding to times with injection of 50 and 150 mM acetate, respectively), and after 60 days that included a hypothetical 300 mM acetate injection from day 38.

### 4.3.3 Seasonal Water Table Fluctuation

Figure 4.5 shows water table elevation dynamics at well X-2 at the Rifle IFRC site from April to December 2008. Since the saturated thickness of the alluvial aquifer under baseflow conditions is ~2.5 m, the 1.5 m rise during the spring is a significant event. Clearly, concentrations of injected amendments can be affected, but increases in U(VI) and dissolved oxygen have been associated with the seasonal rise and fall of the water table in late spring (Figure 4.19).

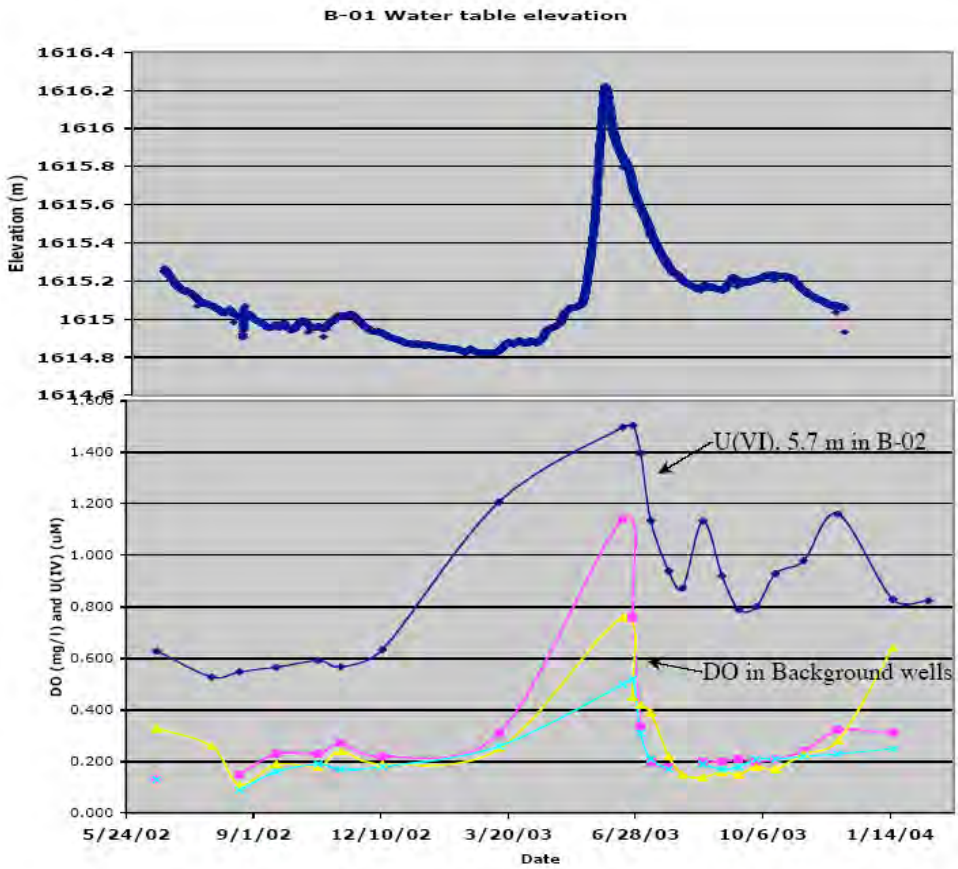


**Figure 4.19.** May 2002 to January 2004 Rifle water table elevation, U(VI) concentrations, and dissolved oxygen in upgradient wells B-01, B-02, and B-03.

The focus here is on the mechanism of gas entrapment and dissolution during the imbibition of previously unsaturated sediments when the water table rises. The conceptual process model has bubbles of pore gases being trapped as the pores fill with rising groundwater. Gas measurements just above the water table at the Rifle IFRC site show that these pore gases likely contain atmospheric levels of oxygen (~20% pO2). This is in contrast to the generally low levels of dissolved oxygen (~0.2 mg/L) in Rifle groundwater that are in equilibrium with pO2 levels 45 times smaller than atmospheric. As the gas in these bubbles equilibrates with the groundwater, oxygen dissolves into solution following Henry's Law. Initially this only affects the dissolved oxygen in the previously unsaturated sediments, but as the water table begins to recede from its peak, groundwater with elevated levels of dissolved oxygen migrates into the permanently

saturated region of the aquifer. Furthermore, diffusion and macroscopic dispersion also enhance the migration of elevated dissolved oxygen levels deeper into the aquifer. We model this aquifer-vadose zone behavior using a 2-phase (active liquid and active gas phases) approach with temperature-corrected atmospheric oxygen as the gas phase boundary condition at the ground surface (top of the vadose zone).

The impact of the entrapped gas can be seen in simulated liquid saturations that are less than 1.0 in the zone between the initial and elevated water table in June and July 2008 (Figure 4.20). During the recession of the water table the oxygen concentrations are generally increased throughout the saturated zone.

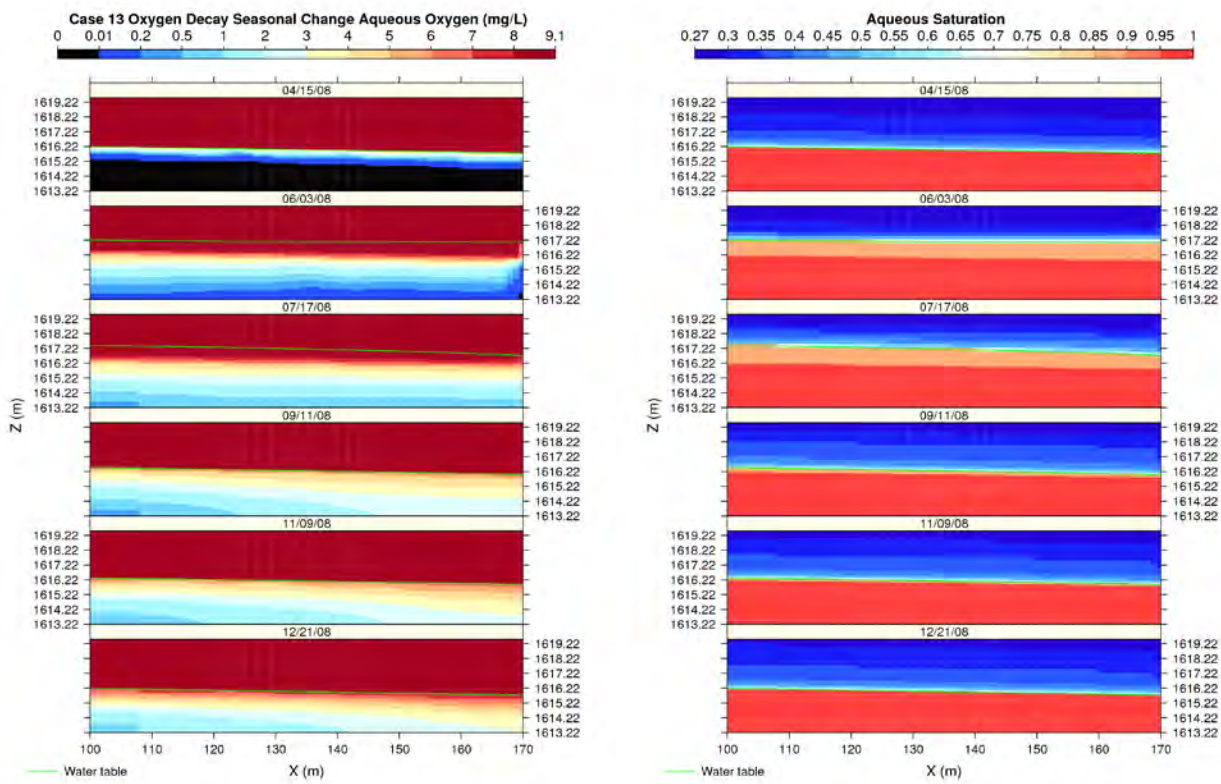


**Figure 4.20.** Simulated dissolved oxygen and aqueous saturation for six dates in 2008: April 15, June 3, July 17, September 11, November 9, and December 21. Note that the 2008 Big Rusty experimental plot lies between X=125 and X=140.

The simulated impact of the biostimulation, which began on July 20, 2008, on dissolved oxygen concentrations from gas entrapment is shown in Figure 4.21. The enhanced levels of dissolved oxygen are generally depleted in the saturated zone from the injection point downgradient to the leading edge of the acetate plume.

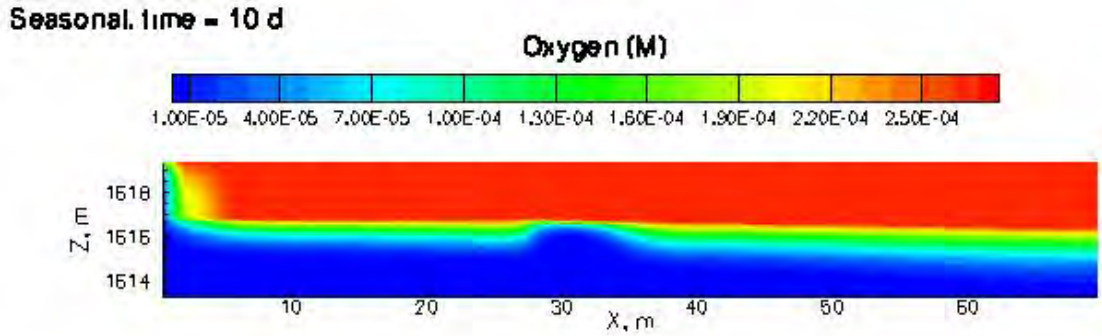


**Figure 4.21.** Simulated dissolved oxygen after 10 days from the start of biostimulation.

Slightly more acetate is consumed in the presence of the elevated dissolved oxygen concentrations near the water table and this behavior is progressive, i.e., acetate continues to be oxidized as it is transported downgradient (Figure 4.22). The impact of including the gas entrapment process is enhanced depletion of the downgradient acetate plume near the water table.

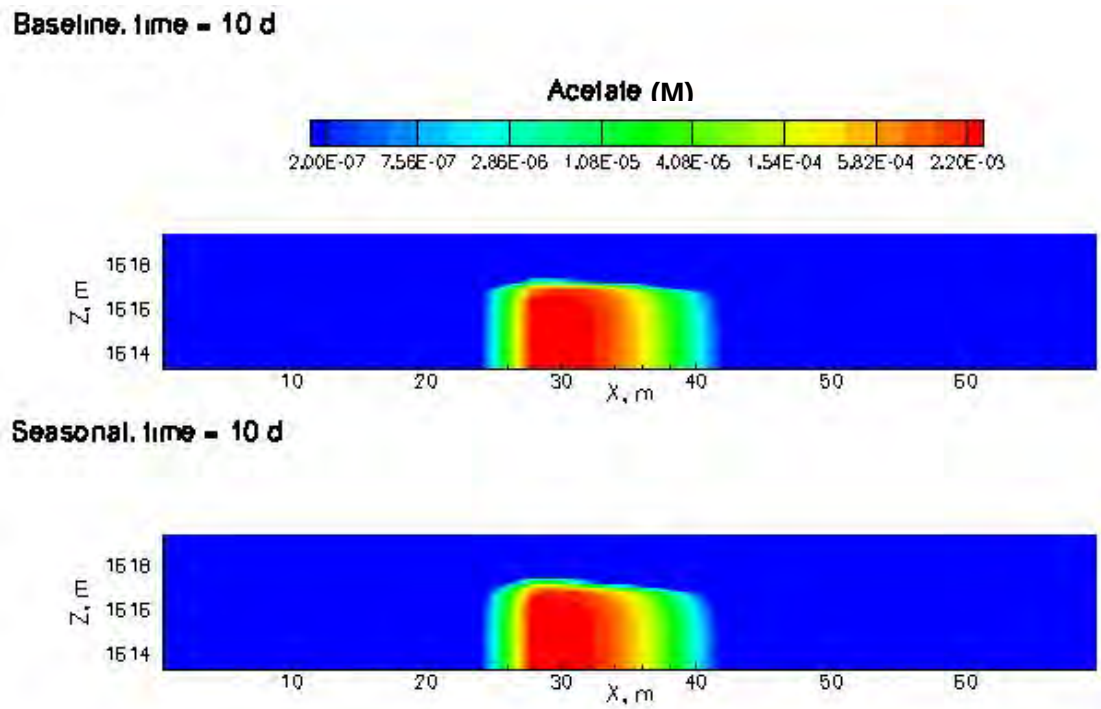


**Figure 4.22.** Comparison of simulated acetate after 10 days of biostimulation for the baseline (top) and the gas entrapment case (bottom).

The additional consumption of acetate required to remove oxygen resulting from gas entrapment processes is seen to affect the spatial distribution of the terminal electron accepting processes. Aqueous U(VI) distributions (Figure 4.23) are shaped similarly to those of the acetate. This reflects the dominance of the U(VI) TEAP reaction over the uranium surface complexation reactions.

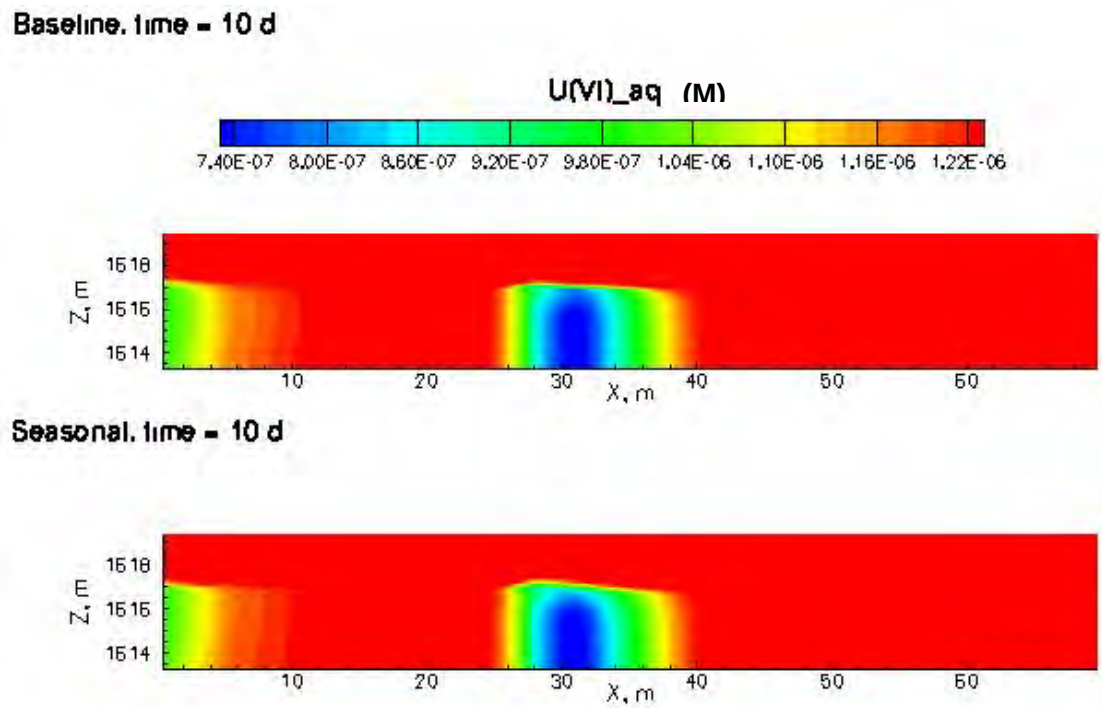


**Figure 4.23.** Comparison of simulated aqueous U(VI) after 10 days of biostimulation for the baseline (top) and the gas entrapment case (bottom)

Aqueous Fe(II) reflects the net impact from the Fe(III) TEAP, $Fe^{2+}$ surface complexation, sulfide promoted goethite dissolution, and iron sulfide mineral reactions. Although less Fe(III) oxide is reacted by the FeRB under the seasonal gas entrapment scenario, this actually leads to a slightly higher rate of the sulfide-goethite reaction. In this reaction, two moles of $Fe^{2+}$ are produced for every mole of sulfide reacted (Table 3.5). The net result is a small increase in aqueous Fe(II) (Figure 4.24). The sulfate behavior is more similar to the U(VI) in that there is slightly less sulfate conversion than the baseline with the biggest difference at the top, downgradient end of the sulfate removal plume (Figure 4.25).

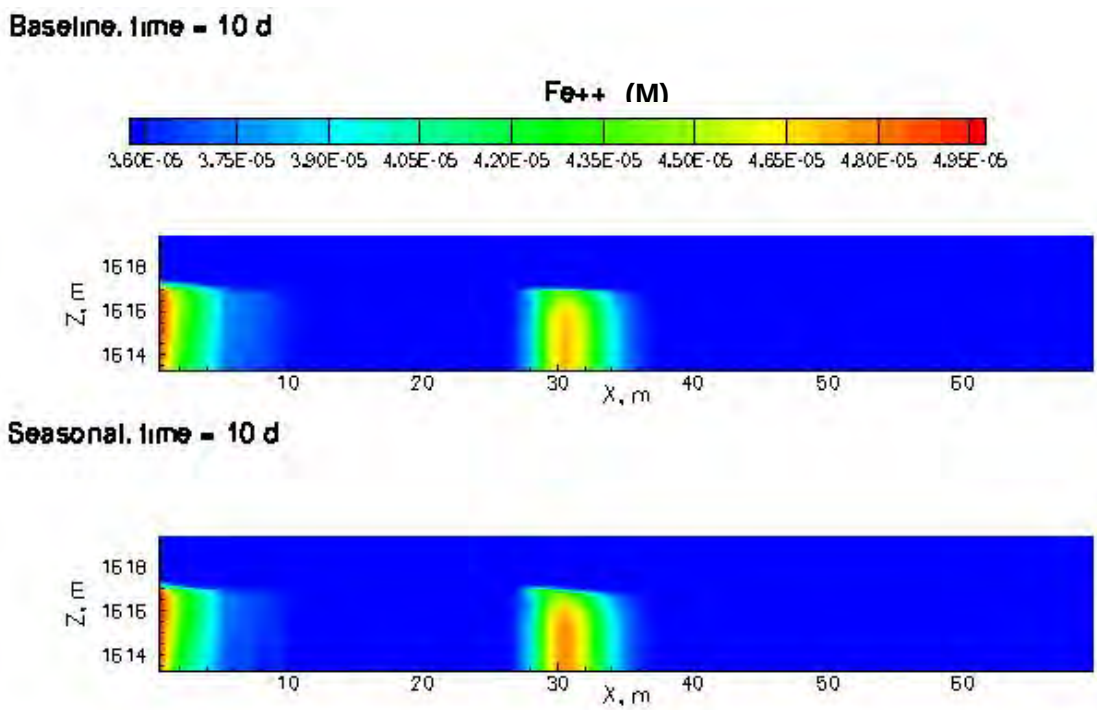


**Figure 4.24.** Comparison of simulated aqueous Fe(II) after 10 days of biostimulation for the baseline (top) and the gas entrapment case (bottom)

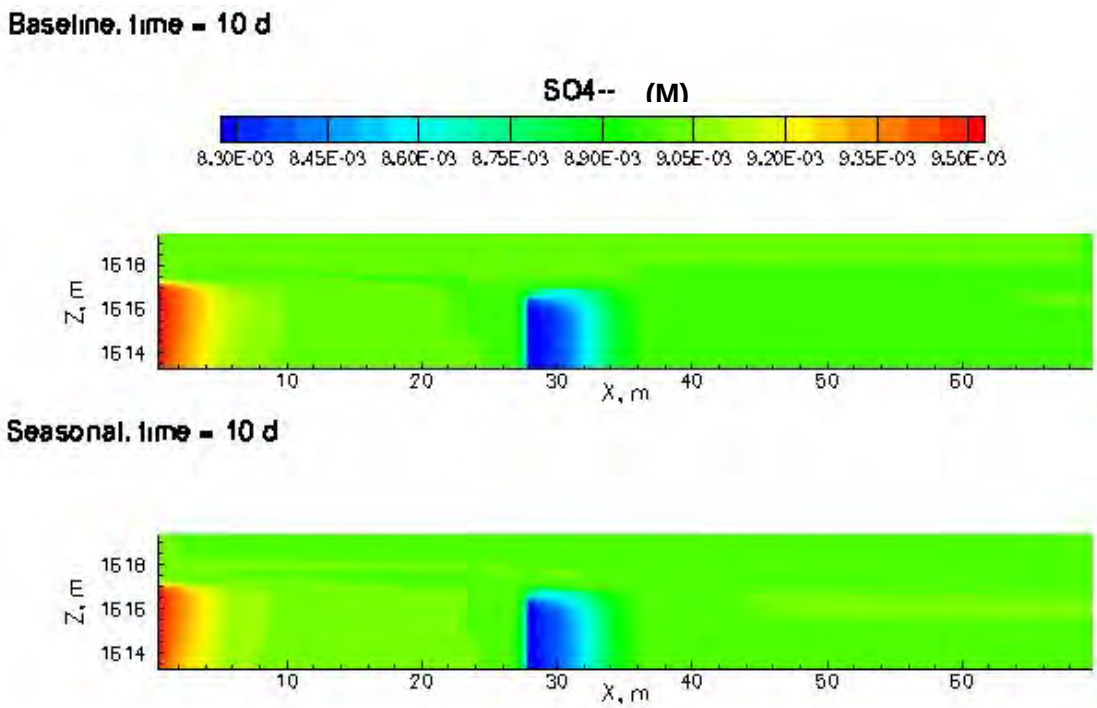


**Figure 4.25.** Simulated sulfate after 10 days of biostimulation with gas entrapment.

### 4.3.4 Flood Case Scenario

Some shallow, alluvial aquifers are periodically subject to enhanced recharge from flood events. Depending on the magnitude and duration of the flood event, the hydrologic properties of the sediments, floodwater chemistry, and geochemistry of variably saturated sediments, the impacts can include

- mobilization of vadose zone uranium,
- increase in the saturated thickness of the water table aquifer,
- alteration in groundwater flow direction, and
- increase in entrapped gas during water table rise.

**Mobilization of vadose zone uranium**. Many shallow uranium waste sites (e.g., UMTRA, DOE legacy waste sites, etc.) are the result of planned and/or unplanned contamination from surface operations and facilities (Riley and Zachara, 1992). Under most environmental conditions, uranium introduced into the unsaturated soil zone from the ground surface will tend to persist relative to the saturated zone because 1) there is less water flow moving through the unsaturated zone and less water in the pores, 2) uranium associated with the larger pores may be bypassed [it might have been originally transported and deposited under a higher flow regime during active surface operations (e.g, waste pond)], and 3) most of the uranium is associated with the solid phase through geochemical reactions. Under these conditions, the uranium-contaminated sediments in the vadose zone are a potential long-term source to the underlying groundwater. A key question is whether recharge-driven uranium transport in the vadose zone can significantly contribute to the uranium concentrations in the groundwater.

The initial recharge-driven uranium front that migrates downward through the vadose zone to the water table is relatively slow, as sorption will significantly retard the transport of the uranium front through the vadose zone. One caveat for this interpretation is that once the uranium front breaks through to the water table, which may be the case below disposal facilities, aqueous uranium is transported through the vadose zone with the velocity of the pore water. If the contribution of recharge to the groundwater flow is small, the recharge-driven flux of uranium may only be significant if relatively high concentrations of vadose zone uranium are widespread.

There are, however, other process mechanisms that could lead to leaching of uranium from the vadose zone into the groundwater. Episodic or event-based water table rise can also allow groundwater to temporarily flow through contaminated sediments that were previously unsaturated. At the Rifle IFRC site and other shallow uranium-contaminated sites, elevated uranium levels in groundwater have been associated with seasonal and episodic hydrologic events. Such observations are consistent with vadose zone uranium-contaminated sediments (Yabusaki et al., 2008). Moreover they are also consistent with a mechanism by which the highest groundwater concentrations are located near the water table, especially when the water

table is high. The magnitude of this behavior can be less obvious when sampling is based on wells with large screened depth intervals.

Potentially, the most intrusive hydrologic event is a flood. This is because it can provide high recharge downward through the vadose zone, potentially raise the water table (thereby increasing the saturated thickness), change the flow direction and drive oxygenated pore water deep into the saturated aquifer. Increase in the aquifer saturated thickness can be problematic if a treatment zone for influent contaminated groundwater has been previously established for a smaller zone. In this case, a fraction of the groundwater may be flowing over the nominal top of the treatment zone. Furthermore, it is not uncommon for higher contaminant levels to be found near the water table. Changes in flow direction can similarly result in contaminated groundwater bypassing a treatment zone.

The modeled flood scenario is designed to examine the impact of 1 foot of river water ponded on the ground surface for 1 week at the Rifle IFRC site. This simulation is an extension of the 2-D, 2-phase, variably-saturated flow with gas entrapment used to assess biostimulation in the presence of elevated dissolved oxygen during the seasonal rise and fall of the Rifle water table in the spring. In this case, the recharge through the ground surface of the ponded floodwaters was applied locally to the Big Rusty field plot. It was necessary to significantly extend the modeling domain upgradient and downgradient by moving the boundaries out to where their impact on the area of interest would be minimized. This is because we do not know *a priori* how the ponded water will affect the saturated thickness near the original boundaries.

Figure 4.26 illustrates how the ponded water boundary condition results in near-saturation of a large fraction of the vadose zone. In fact, it is the entrapped gas that prevents complete saturation of the vadose zone pore space below the recharge source. The “mounding” effect during the 7 days of active ponding (Figure 4.27) overwhelms the regional flow and drives water flow down and laterally away from the recharge source. Floodwater tracer in Figure 4.28 shows that the base of the groundwater mound is initially from vadose zone pore water that has been pushed down ahead of the infiltrating floodwater. This causes the flood water to drape over the mound and move laterally resulting in higher concentrations of floodwater around the perimeter of the mound. With the removal of the surface ponding condition, the regional flow in the saturated zone is largely restored within 3 days. However, the oxygenated water that was recharged has been driven deep into the saturated zone during the flood (Figure 4.29). This zone of dissolved oxygen, near saturation with atmospheric oxygen, persists until the regional flow can advect it out of the domain.

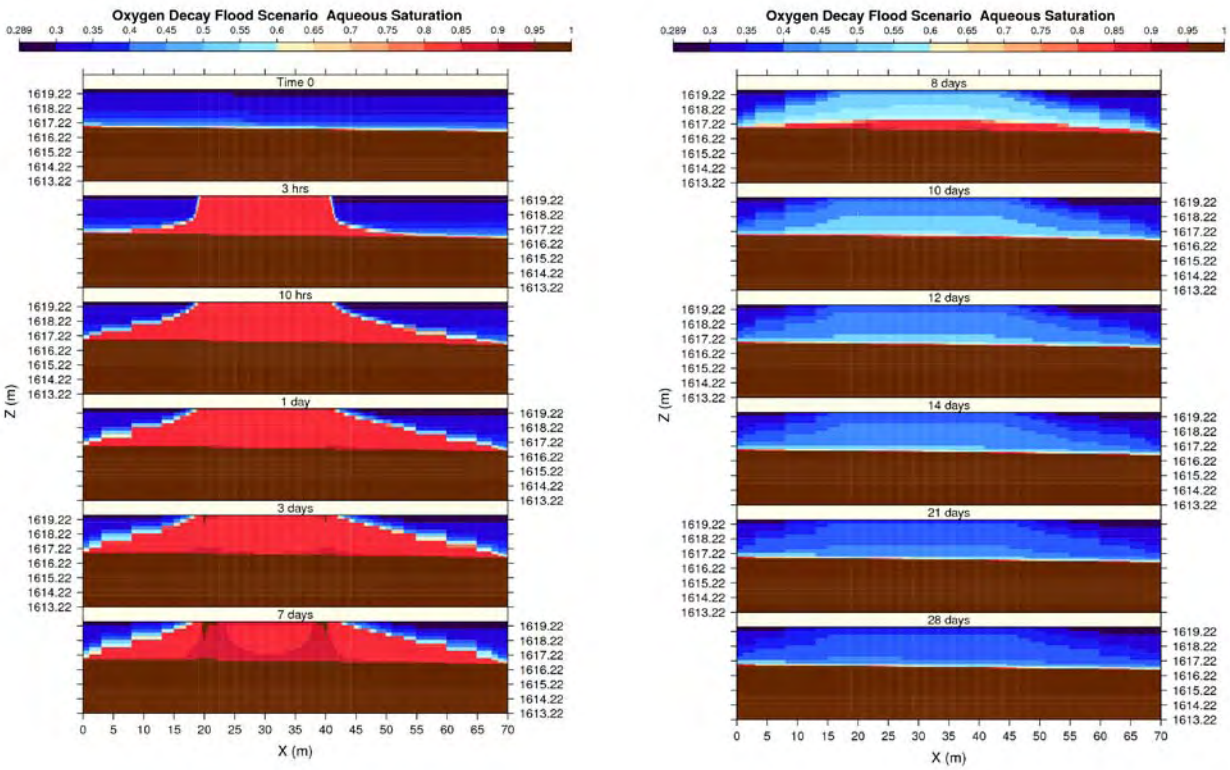


**Figure 4.26.** Simulated aqueous saturations during the 7 day flood and 21 days following the flood.

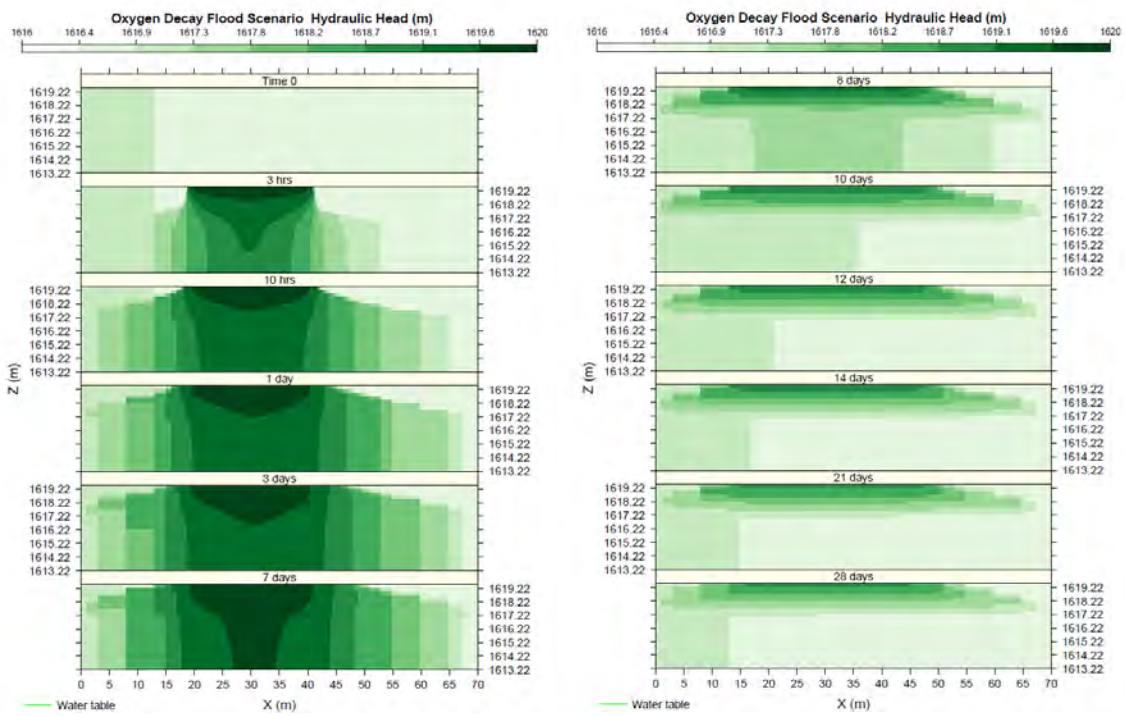


**Figure 4.27.** Simulated hydraulic head during the 7 day flood and subsequent 21 days.

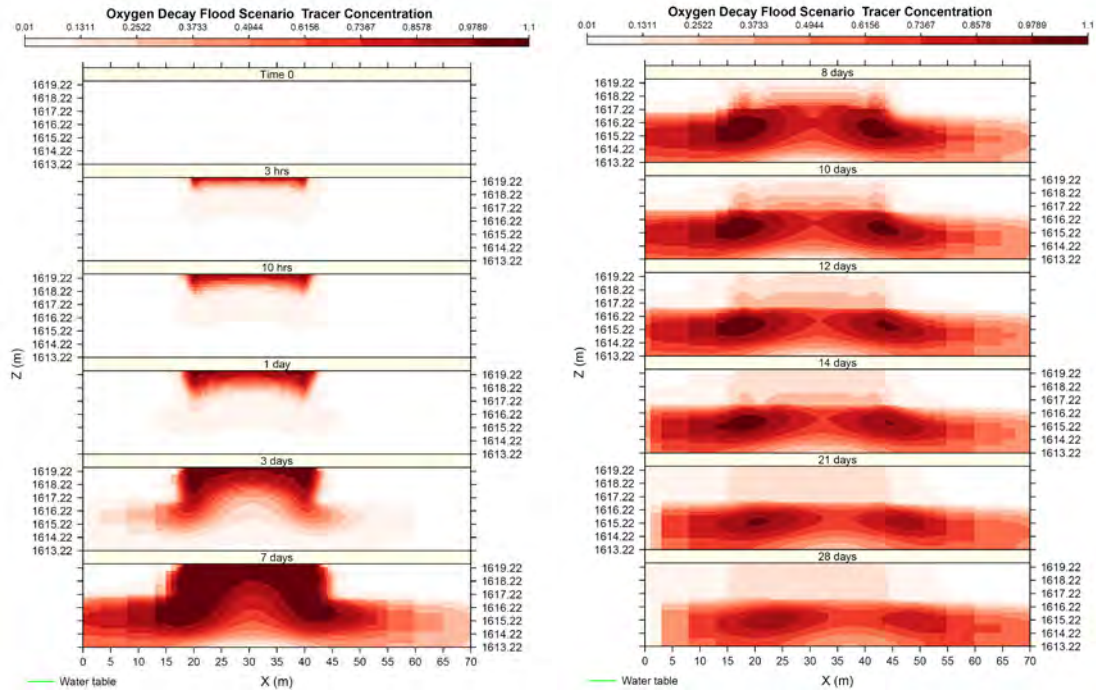


**Figure 4.28.** Simulated flood water tracer during the 7 day flood and the following 21 days.

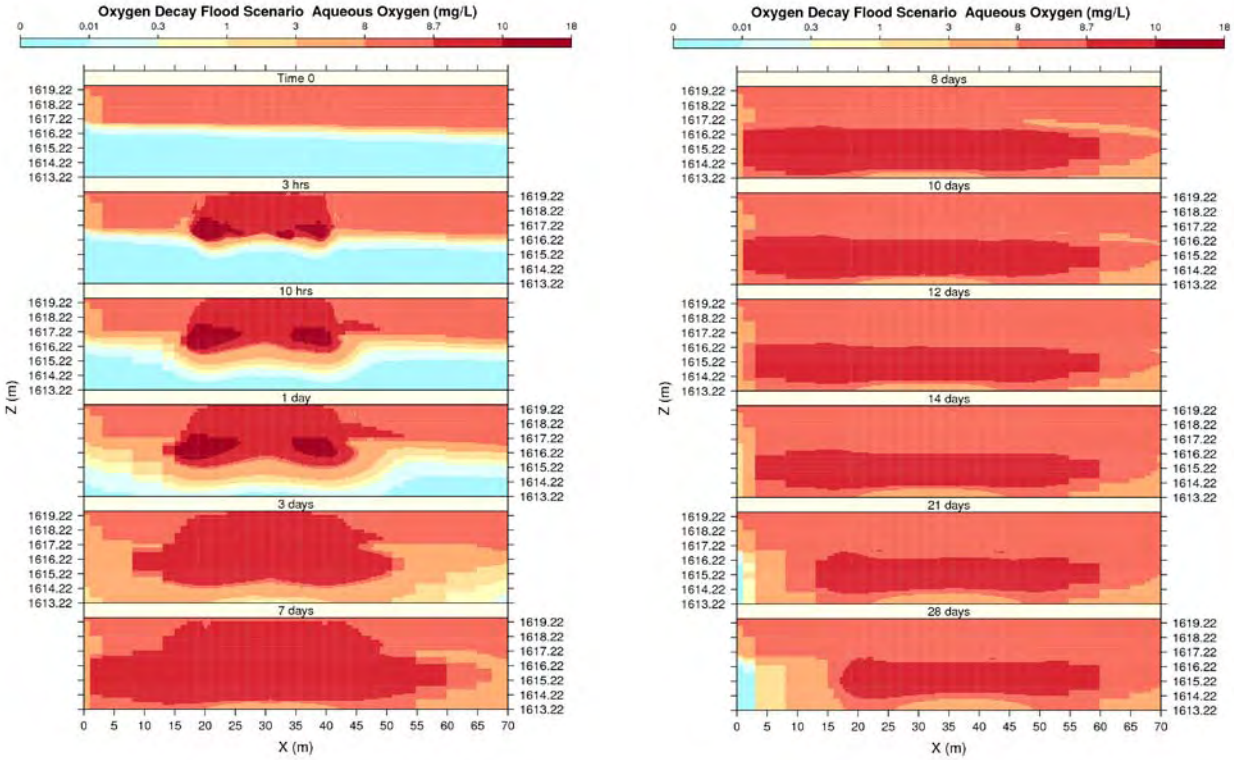


**Figure 4.29.** Simulated aqueous oxygen during the 7-day flood and the following 21 days.

In the first scenario, the biostimulation sequence from the baseline simulation was initiated at the beginning of the flood ponding event. While our interest was in the effects of elevated oxygen on biostimulation, in this scenario the principal impact of the flood event was on the distribution of acetate during active injection (Figure 4.30). After 5 days of simulated biostimulation, the acetate has been driven down towards the aquifer bottom and upgradient of the initial experimental plot. As compared to the fairly regular distribution in the baseline, the distribution of sulfide and $UO_2(s)$, which are products of the biostimulation, are seen to be heavily skewed to the bottom of the aquifer and away from the intended treatment zone location. Another consequence of flooding with dilute river water can be seen in the significant removal of U(VI) from solution in the vadose and saturated zones (Figure 4.30). This is actually a geochemical response to the low alkalinity river water resulting in enhanced uranium surface complexation.

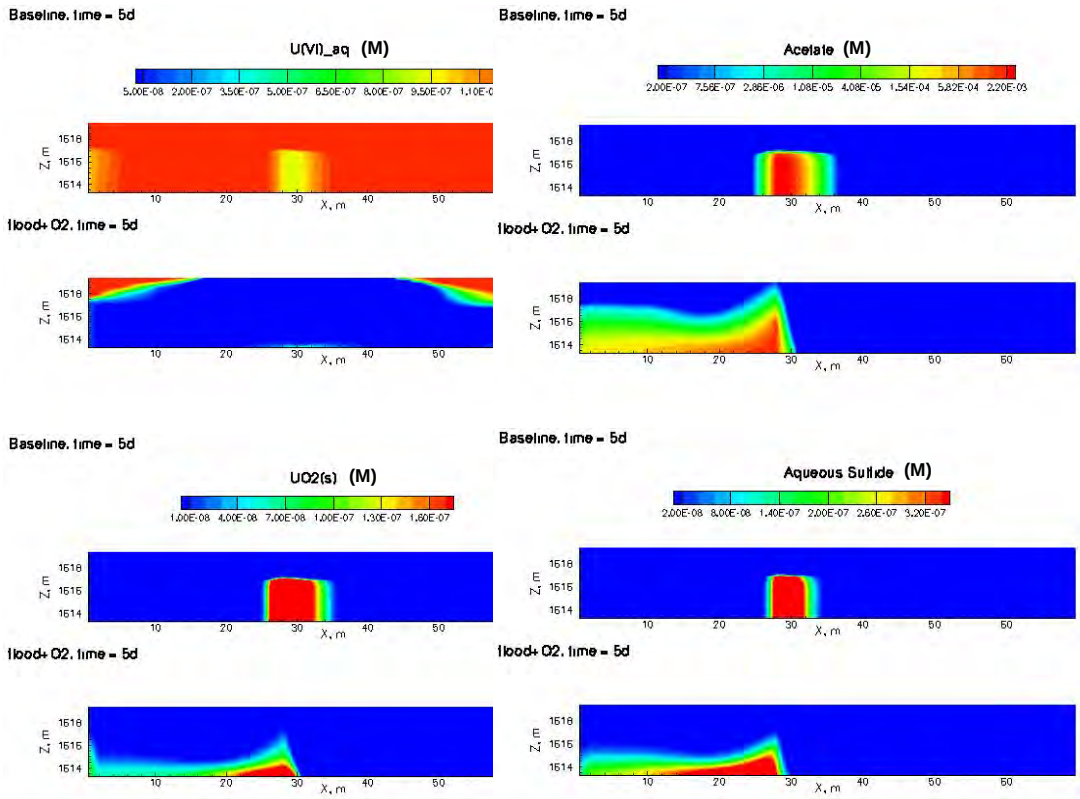


**Figure 4.30.** Comparison of baseline and flood scenario at day 5 for U(VI), acetate, $UO_2(s)$, and aqueous sulfide.

Noting that the regional flow field is largely restored a few days after the ponding condition is removed (Figure 4.27), a second flood scenario was simulated, this time beginning acetate injection 1 day after the ponding condition was removed. The comparison of the bromide tracer behavior between the baseline and this second flood scenario (Figure 4.31) indicates that 1) regional groundwater flow and transport has largely been re-established and 2) the saturated thickness of the system is larger than the baseline. In general, the additional saturated thickness

results in a more gradual concentration transition from the top of the injectate pulses up to the water table.

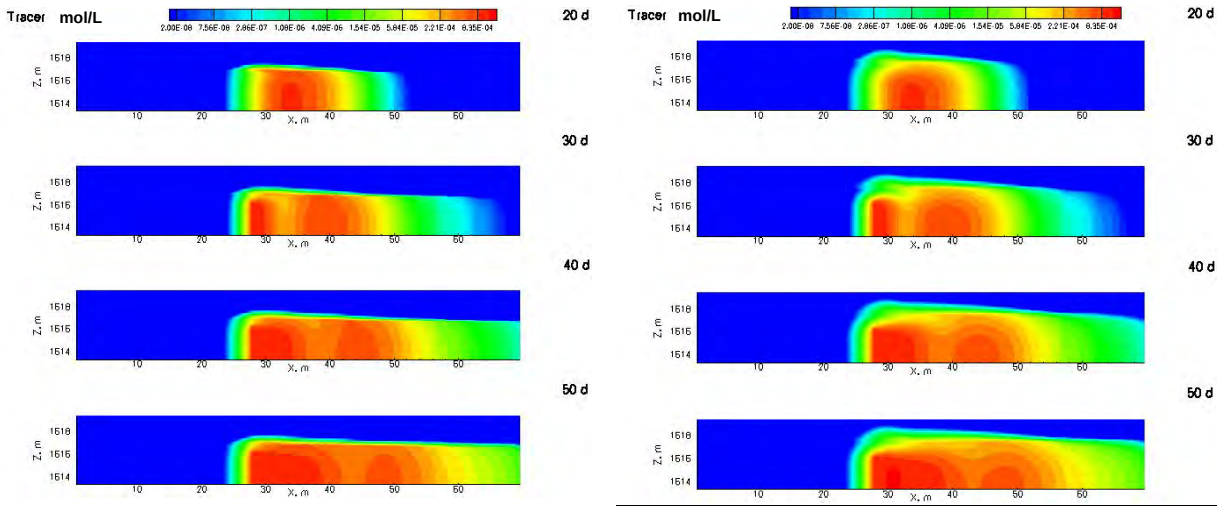


**Figure 4.31.** Comparison of injected tracer at 20, 30, 40, and 50 days after start of biostimulation for baseline (left) and flood scenario (right).

The key impact from the flood scenario is the presence of saturated dissolved oxygen levels in porewaters throughout the subsurface model domain. The oxygen TEAP is usually a slow background process dependent on natural organic carbon, which is typically more refractory compared to low molecular weight electron donors such as acetate. Figure 4.32 illustrates the clear link between the concentration of the acetate pulses and dissolved oxygen removal. Near complete removal of oxygen occurs during the period of highest (tripled) acetate concentrations (after day 38 of biostimulation). These simulations also show how the ambient water chemistry (with low dissolved oxygen) entering the model domain from the upgradient model boundary can help drive the system back to pre-flood conditions.

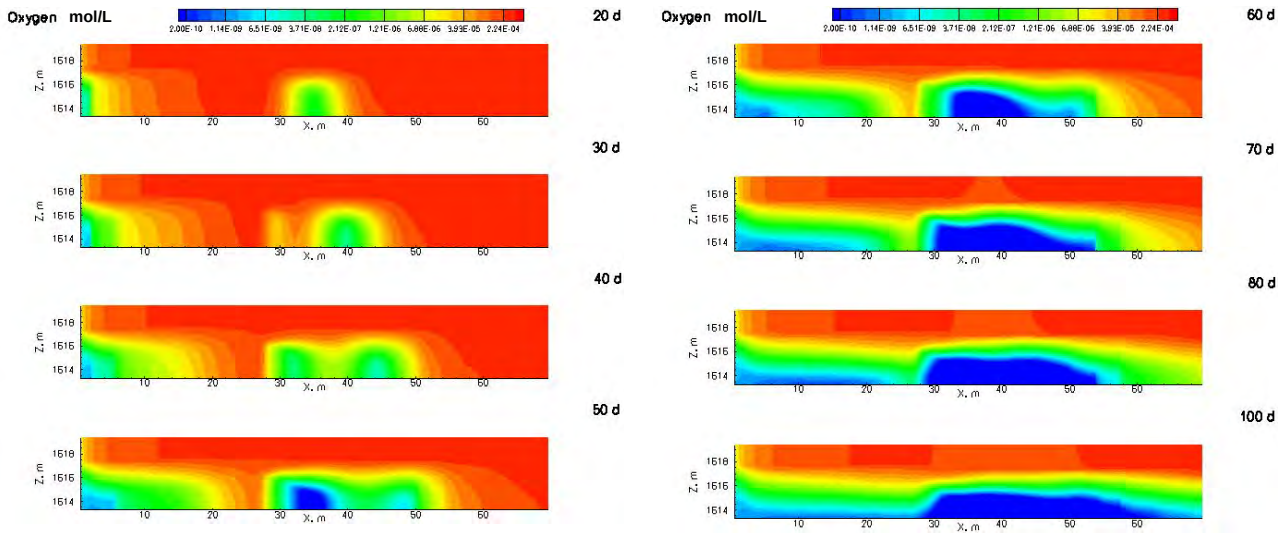


**Figure 4.32.** Simulated dissolved oxygen concentrations at 20, 30, 40, 50, 60, 70, 80, and 100 days after initiation of acetate biostimulation.

The acetate concentrations in the post-flood scenario simulation are slightly but consistently lower than the baseline concentrations. This is due to the larger saturated thickness and the presence of the dissolved oxygen TEAP, which increases acetate consumption compared to the baseline (Figure 4.33). In general, acetate consumption leads to a more noticeable separation of the initial 2-week amendment pulse than exhibited by the tracer. Over the first 50 days of the biostimulation, the initial acetate pulse has more vertical variability and migrates as a semicircular distribution of diminishing concentrations about a center of mass at the aquifer bottom.

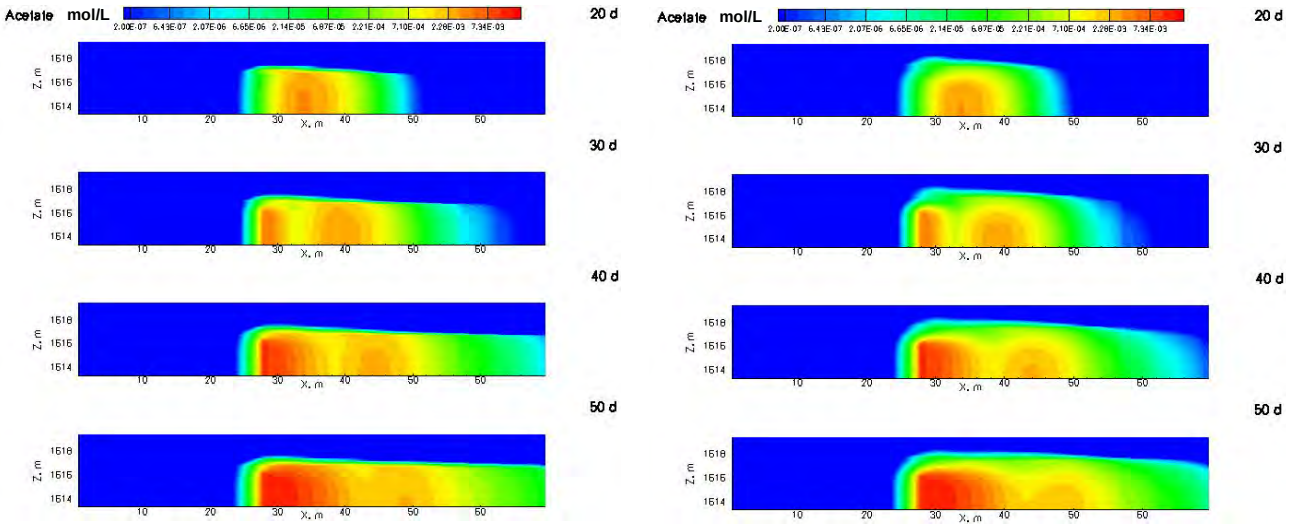


**Figure 4.33.** Comparison of simulated acetate concentrations at 20, 30, 40, and 50 days after start of biostimulation for baseline (left) and flood (right) scenarios.

The U(VI) behavior in the post-biostimulation scenario is not significantly different from the baseline. In both cases, uranium is generally distributed in one zone downgradient from the injection; i.e., the 1-week interruption in acetate is not discernible in the simulation of the U(VI) removal or the precipitation of U(IV) mineral, uraninite ($UO_2$). Slightly lower concentrations can be found in the post-flood scenario aqueous U(VI) (Figure 4.34) and $UO_2$(s) (Figure 4.35) which also have larger vertical extent because of the increased saturated aquifer thickness.

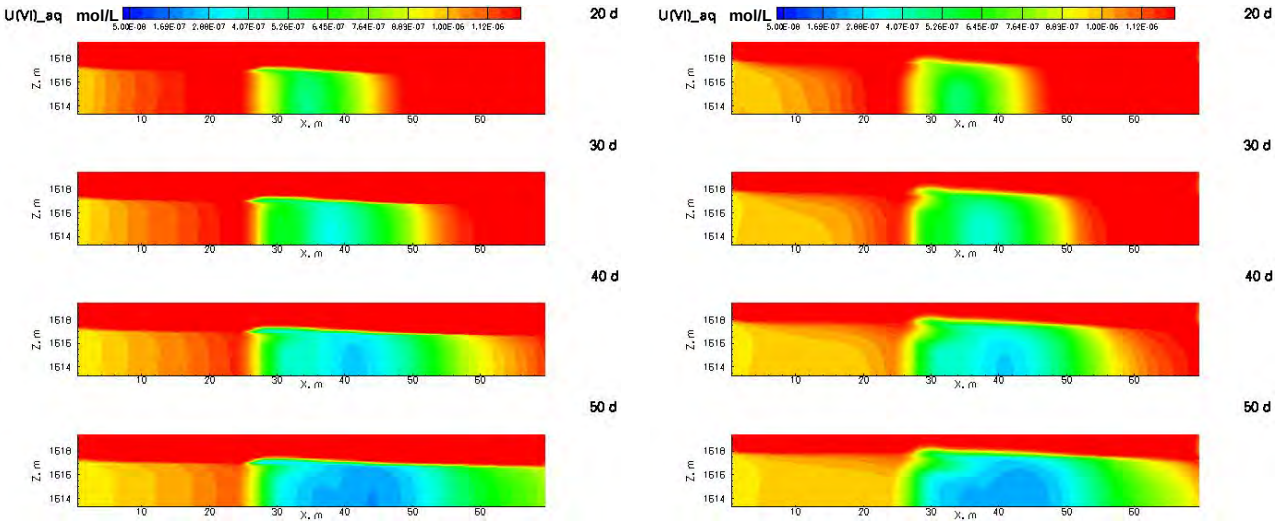


**Figure 4.34.** Comparison of simulated aqueous U(VI) concentrations at 20, 30, 40, and 50 days after start of biostimulation for baseline (left) and flood (right) scenarios.

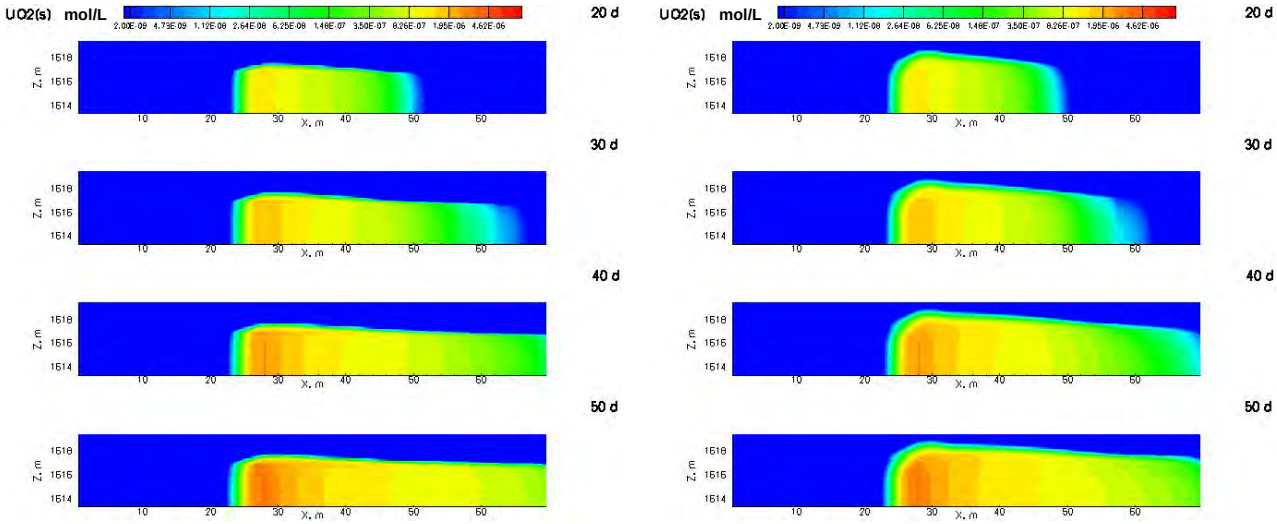


**Figure 4.35.** Comparison of simulated $UO_2$(s) concentrations at 20, 30, 40, and 50 days after start of biostimulation for baseline (left) and flood (right) scenarios.

The impact of the additional oxygen present in the system from the flood event is more evident in the behavior of the other TEAPs. Although slightly more acetate is consumed in the post-flood biostimulation scenario than the baseline, aqueous Fe(II) concentrations are slightly less (Figure 4.36) compared to the baseline.

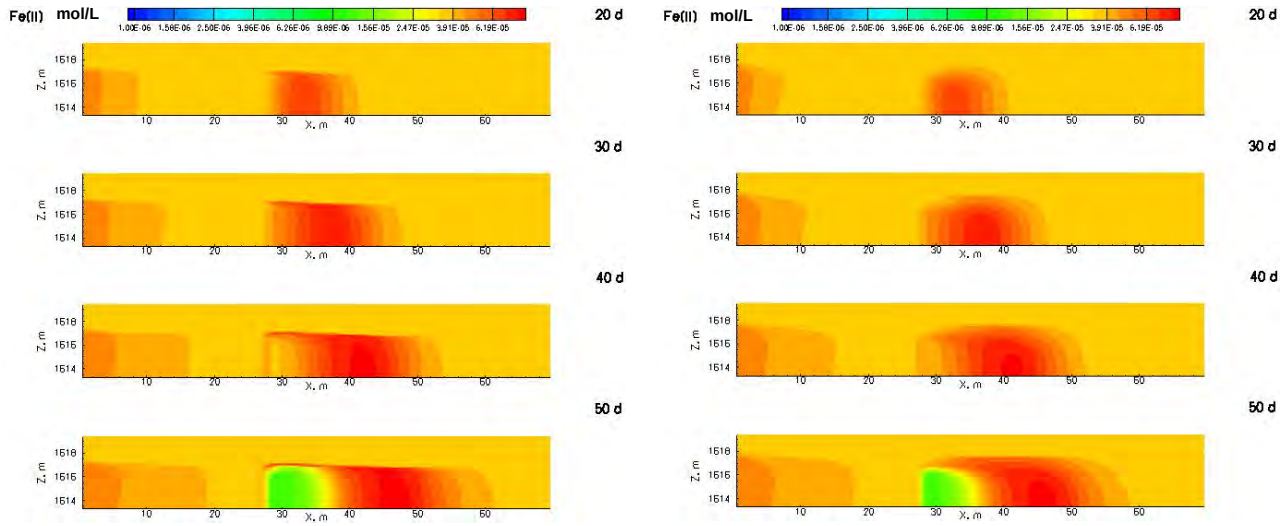


**Figure 4.36.** Comparison of simulated aqueous Fe(II) concentrations at 20, 30, 40, and 50 days after start of biostimulation for baseline (left) and flood (right) scenario.

The sulfate TEAP, which becomes dominant later in the biostimulation, also exhibits slightly less conversion at comparable times for the post-flood simulation (Figure 4.37). For the post-flood scenario under the assumption of a simultaneous oxygen TEAP, the general observation is that even under dissolved oxygen concentrations at saturation with the atmosphere, a relatively small amount of acetate can return the aquifer to suboxic levels. Under these conditions, the other TEAP reactions, including U(VI) bioreduction, can proceed similarly to the baseline case.

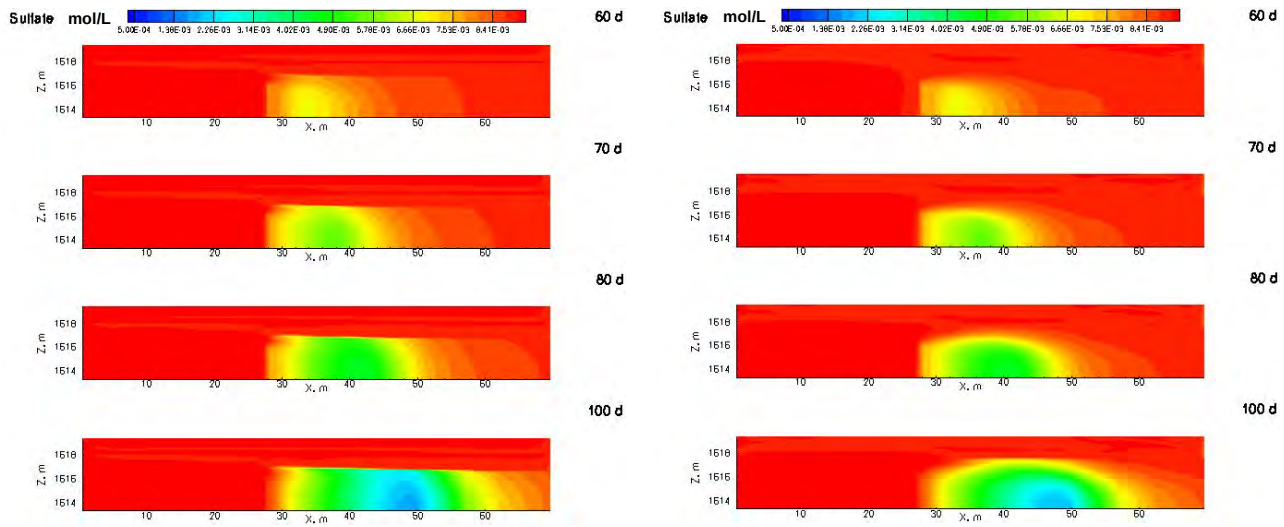


**Figure 4.37.** Comparison of simulated aqueous sulfate concentrations at 60, 70, 80, and 100 days after start of biostimulation for baseline (left) and flood (right) scenario.

# 5 Summary and Conclusions

At a number of subsurface sites including the Hanford Site and Uranium Mill Tailings Remedial Action (UMTRA) sites, uranium plumes persist in spite of decade and longer periods of continuously high groundwater flow rates. A potentially cost-effective engineering alternative is uranium bioremediation via *in situ* biostimulation of indigenous microorganisms. At the Old Rifle UMTRA site in western Colorado, the U.S. Department of Energy (DOE) has been conducting a comprehensive investigation (Integrated Field-Scale Research Challenge or IFRC) into the subsurface processes, properties, and conditions controlling uranium behavior before, during, and after amending groundwater with electron donor. In this case, the injection of acetate has been accompanied by significant microbially-mediated conversion of mobile uranium in the hexavalent oxidation state, U(VI), to the reduced oxidation state, U(IV), which is mineral-associated and thus, immobile. As a relatively new technology where the contaminant is not destroyed or extracted, the long-term performance of *in situ* uranium bioremediation is an open issue. Our understanding of uranium mobility through the systematic interplay between biology, geochemistry, and hydrology continues to benefit from ongoing DOE research. In particular, the Rifle IFRC project has developed and parameterized a detailed biogeochemical reaction model that captures observed trends in multiple component concentrations over a range of biostimulation conditions and sites (Fang et al., 2009).

The multicomponent biogeochemical reactive transport model, calibrated with data from the 2008 field experiment at the Rifle IFRC site, accounts for key terminal electron accepting processes (i.e., U(VI), Fe(III), sulfate) and abiotic reaction processes in the biostimulation field experiments. The model generally captures the observed dynamics in pH, U(VI), Fe(II), sulfate, and acetate.

The approach taken by the present study is to use the detailed understanding of uranium bioremediation developed at the Old Rifle IFRC site as a framework to evaluate hypothetical scenarios of general interest at other sites. The biogeochemical conceptual model, which is based on laboratory studies and acetate biostimulation experiments performed at the Old Rifle IFRC site since 2002, holds that Fe(III)-reducing microorganisms, stimulated by acetate, can simultaneously use Fe(III) mineral and aqueous U(VI) as terminal electron acceptors. It is this concomitant bioreduction of aqueous U(VI) to U(IV) mineral by dissimilatory metal reducing bacteria that is the bioremediation principle for uranium removal from groundwater. After about 30 days, acetate-oxidizing sulfate reducing microorganisms become enriched using sulfate as a terminal electron acceptor with Fe(III)-reducing microorganisms remaining active. The significance of the sulfate reduction phase is that 1) U(VI) groundwater concentrations increase from the low concentrations associated with the iron reduction phase, 2) there is a continuous influx of high sulfate (ca. 10 mM), which can generally maintain sulfate reducing conditions unless acetate concentrations in excess of the sulfate concentrations are used, and 3) longer-term post-biostimulation removal of uranium from groundwater is associated with long periods (~months) of active sulfate reduction during the biostimulation.

The paradox of the sulfate TEAP, i.e., higher uranium concentrations than during Fe(III) bioreduction but longer-term post-biostimulation removal, is the subject of ongoing investigation. In this case, the abiotic geochemistry before, during, and after biostimulation must be considered. At the Rifle IFRC site, uranium surface complexation is the dominant abiotic uranium attenuation process and, under site conditions, is sensitive to changes in the alkalinity, pH, and major ions that result from acetate biostimulation. Consequently, a comprehensive representation of heterogeneous and homogeneous abiotic chemical reactions in equilibrium and kinetic forms was necessary to account for the bicarbonate, U(IV), Fe(II), and sulfide products of the biologically mediated reactions.

We use the parameterized biogeochemical reaction model developed by the Rifle IFRC project as part of the simulation testbed for the targeted scenarios in the present study. The principal assumption is that extensions to the coupled-process simulation capability required to address these scenarios are valid. Since these extensions were invoked without observation at the Rifle IFRC site, the simulated results should be used to highlight potential issues for consideration in the design of *in situ* uranium bioremediation.

## 5.1 One-Dimensional Reactive Transport

### 5.1.1 Sensitivity Analyses

The 2008 biostimulation experiment at the Old Rifle IFRC site was used as the baseline for analyzing and comparing the results of the scenarios for this study. For the purpose of initially identifying the sensitivity of simulation results to model parameters, we used a one-dimensional model domain for the multicomponent biogeochemical reactive transport simulations. Hydraulic conductivity, porosity, and dispersivity were calibrated with downgradient monitoring well observations of bromide tracer that was injected along with the acetate electron donor. Initial and boundary conditions for hydrology and geochemistry were based on observations from upgradient and downgradient monitoring wells.

The deviation of aqueous uranium behavior from the observed baseline behavior was used as the indicator of sensitivity to a process model parameter. Selected parameters were individually perturbed to identify sensitivity. In this case, parameter sensitivity was manifested in three different forms: reactions, reaction rates, and rates of transport. In the current biogeochemical reaction network, geochemical adsorption and desorption of uranium is controlled by a set of equilibrium uranium complexation reactions that are affected by many factors but especially alkalinity, pH, uranium, surface site density and calcium. Reaction rates for the kinetic reactions (e.g., biologically mediated and mineral reactions) are based on rate laws that are dependent on concentrations of reactants and/or products. In the case of the U(VI) TEAP, the intrinsic rate has a direct impact on the magnitude of the aqueous uranium concentrations (i.e., higher intrinsic rate results in higher uranium removal from groundwater).

Flow rates, porosity, and dispersivity affect transport: 1) the influx of groundwater, which controls the *in situ* concentration of injected amendments; 2) the supply of chemical components in the influent groundwater, which controls the availability of reactants; and 3) the transport of the electron donor and the aqueous byproducts of TEAP reactions. For biostimulation in advection-dominant systems, the primary impact of transport on aqueous uranium concentrations is the timing of acetate arrivals at downgradient locations. The oxidation of acetate coupled to various TEAP reactions (bioreduction of Fe(III) minerals, U(VI), and sulfate) occurs during transport through the aquifer. Since the TEAP reactions are nonequilibrium, the interplay of transport rates and reaction rates will determine the location and magnitude of the mobile TEAP reactants and products. As advection decreases (e.g., lower flow rate, higher porosity), there is later arrival of TEAP reaction products together with decreased rates of uranium bioreduction. This effect is due to the increased residence time and reaction time for acetate nearer the acetate injection point. This results in more sulfate reduction nearer the acetate injection point, which is associated with decreased rates of uranium bioreduction.

### 5.1.2 Terminal Electron Accepting Processes (TEAPs)

Three TEAPs have been identified as having roles that contribute to uranium bioremediation at the Rifle IFRC site: Fe(III) mineral, aqueous U(VI), and sulfate. The conceptual model (Anderson et al., 2003; Fang et al., 2009; Vrionis et al., 2005; Yabusaki et al., 2007) is that *Geobacter* spp., the principal acetate-oxidizing dissimilatory metal-reducing bacteria associated with U(VI) bioreduction at the Rifle IFRC site, initially become enriched in the presence of acetate and bioavailable Fe(III). The sulfate-reducing bacteria exhibit a slower growth rate but after ca. 30 days of biostimulation with acetate amendment they become the principal consumer of acetate leading to enrichment in sulfate-reducing bacteria and dominance in the microbial community.

In the Rifle biostimulation experiments, significant sulfate reduction is associated with higher aqueous U(VI) concentrations and, paradoxically, longer post-biostimulation uranium removal from groundwater. A possible link of extended sulfate reduction to post-biostimulation uranium removal is through the formation of iron sulfides and elemental sulfur. These mineral phases have been identified in some studies (Boonchayaanant et al., 2009; Wersin et al., 1994) in the abiotic reduction of aqueous U(VI) to immobile U(IV) mineral. They can also act as an electron donor for microbially-mediated reduction of U(VI) to U(IV) and/or dissolved oxygen to water. The latter can be an important mechanism in maintaining reducing conditions needed for the stabilization of previously reduced and immobilized U(IV) (Abdelouas et al., 1999) although some studies have shown reduced sulfur minerals did not prevent U(IV) reoxidation in the presence of Fe(III) (Sani et al., 2005). Currently, post-biostimulation reduction of U(VI) to U(IV) has not been directly observed at the Rifle site. This is consistent with other studies (Suzuki et al., 2005) where the reduction to U(IV) has not been found in direct association with iron sulfide minerals. Another post-biostimulation uranium attenuation mechanism is U(VI) sorption on to biopolymers (Choi and Park, 2005). In laboratory experiments with Rifle

sediments and groundwater, N'Guessan et al. (2008) identified sorption to *Mollicute* species from the phylum *Firmicutes*. These small bacteria have no cell wall and became significant in the microbial community only after cessation of acetate biostimulation.

Oxygen and nitrate concentrations in the Rifle groundwater are sufficiently low that they are assumed to be negligible. At many sites, this assumption cannot be made and the presence of these oxidizers (Akob et al., 2008; Madden et al., 2009) is a concern for bioremediation technologies that rely on lowering the redox potential. Accordingly, biologically mediated reactions for the oxygen and nitrate TEAPs were incorporated in the simulation capability. Since these TEAPs and the associated acetate-oxidizing microorganisms have not been characterized at the Rifle IFRC site, hypothetical rate laws were used. For this scenario, dissolved oxygen at near saturation with atmospheric oxygen (8 mg/L, 250 uM) and nitrate (8 mg/L, 130 uM) were added to the initial and boundary condition water chemistry. Based on the reaction stoichiometry, each mole of acetate can potentially reduce 0.8 moles of DO or 3 moles of nitrate. The results, when compared to the baseline, suggest that ~0.3 mM of additional acetate would be consumed to nearly deplete the DO and nitrate. This small amount of acetate is primarily due to the relatively low concentrations of these terminal electron acceptors although the stoichiometric efficiency of bioconversion is also a factor. While this is a relatively small amount of acetate, there are potential complications that should be considered. One issue is the possible need to establish and/or maintain depleted levels of oxygen, nitrate, and nitrite prior to remediation taking place. This may include time for the microbial community to transition to the desired structure and function. Another issue is the possible need to keep oxygen, nitrate, and nitrite levels sufficiently low to maintain the stability of bioreduced (and immobilized) uranium. This may be true in the presence of a continuous influx of high DO and nitrate that would otherwise oxidize reduced phases, possibly leading to uranium remobilization.

### 5.1.3 Electron Donors

While the field studies at the Rifle IFRC site have relied exclusively on acetate biostimulation, there are other electron donors (and combinations) that have been employed at other sites (Istok et al., 2004; Wu et al., 2006). Lactate and ethanol were incorporated into this analysis by using reactions from the literature for our Fe(III) mineral, aqueous U(VI) and sulfate TEAPs and the same rate law that was used for acetate. Acetate is an intermediate oxidation byproduct of TEAP reactions for both additional electron donors, so we retained the existing TEAP reactions and rate laws and supplemented them with the necessary lactate and ethanol reactions to model the required sequence of reactions. It should be noted that there were no field experiments using these electron donors so there is no confirmation that the same microorganisms or functional groups were stimulated, which could significantly impact the rates. The simulated results for ethanol and lactate are very similar but, in comparison to the acetate baseline, there is considerably more electron donor consumption and, consequently, more bicarbonate production. In this case, these behaviors are due to the different TEAP reaction stoichiometries that are specific to these electron donors.

Modeling of slow-release glucose-based, oil-based, or polylactate electron donors was not included in modeling scenarios for this report. These electron donors may have desirable properties, depending on specific applications, and may be included in future modeling efforts. However, it is important to note that the performance of these materials when used for uranium bioreduction is still dependent on fundamental electron transfer processes resulting in reduction of U(VI) and maintenance of conditions that limit remobilization of uranium. Issues noted in this report are therefore likely to apply to these electron donors albeit with different rates and process details. This underscores the importance of site- and process-specific information to ensure that bioremediation performs as predicted.

## 5.2 Two-Dimensional Variably Saturated Flow and Reactive Transport

Two-dimensional simulations of variably saturated flow and biogeochemical reactive transport were performed in a vertical cross-section of the Rifle subsurface to evaluate several scenarios. In this case the baseline included the vadose zone above the water table and accounted for observed changes in the saturated thickness of the phreatic aquifer. In addition to incorporating the vadose zone, the two-dimensional modeling approach afforded the opportunity to investigate variable density on the migration of electron donor amendment, gas entrapment during seasonal water table fluctuation, and dissolved oxygen enhancement under a flood scenario. The two-dimensional simulation results for the baseline were generally similar to the one-dimensional results; however, the ability to address water table dynamics improved the fidelity of the simulated concentrations with the observations.

### 5.2.1 Injectate Density

Acetate and bromide are slightly denser than groundwater. In the 2003 biostimulation field experiment performed at the Rifle IFRC site, there was clear evidence that the higher density of the injected amendment led to higher acetate and bromide concentrations near the bottom of the aquifer. In the more recent 2007 and 2008 field biostimulation experiments at the Rifle IFRC site, this issue was addressed by injecting less concentrated solutions at higher rates to achieve similar *in situ* acetate concentrations. Furthermore, cross-well mixing was used to maintain horizontal and vertical uniformity in the amendment release from the 10 fully penetrating injection wells. In this scenario, the variable density simulations targeted the behavior of the denser injectate (acetate and bromide) as it migrated from the injection wells. During transport there is mixing with groundwater and the acetate is being consumed in TEAP reactions. The results of the baseline simulation showed negligible impact of injectate density on the delivery of acetate downgradient when the target *in situ* acetate concentration was ~5 mM. When the target *in situ* acetate concentration increased to ~15 mM later in the simulation, there was a small vertical gradient of acetate concentration that increased ~1 mM for each meter of depth. To identify a concentration where variable density would have a more noticeable impact, the target *in situ* acetate concentration was increased to 30 mM. This resulted in a vertical gradient over 3

mM/m depth. The impact of the higher densities was more pronounced at the leading and trailing edges of a finite amendment pulse. These results are specific to acetate but users of denser amendment solutions should proceed cautiously. It should be noted that the impact of variable injectate density effects is affected by many factors including groundwater flow rates, dispersivity, heterogeneity, and anisotropy.

### 5.2.2 Gas Entrapment

Gas entrapment occurs as unsaturated pores fill with liquid during wetting events and is part of the theory governing hysteretic pressure-saturation behavior in the vadose zone (Kaluarachchi and Parker, 1992). In this case, we are interested in the oxygen in the gas that is trapped as bubbles in pores that are becoming saturated. Above the water table in shallow alluvial subsurface systems, pore gas may contain near-atmospheric levels of oxygen. This situation nominally provides a mechanism for oxygen to partition to the aqueous phase and diffuse through the water table into the groundwater. Without an oxygen sink, this process would eventually result in the oxygenation of the saturated zone. The low dissolved oxygen (0.1 – 0.5 mg/L) in the Rifle groundwater is assumed to be the result of microbial activity. Under these conditions, the relatively thin layer of elevated oxygen (1-2 mg/L) near the water table would be the result of a dynamic balance of groundwater flow rate, oxygen diffusion at the water table, and microbial reduction.

The seasonal (spring to summer) hydrograph describing water table rise and fall at the Rifle IFRC site is associated with elevated oxygen levels near the water table. In this case, the water table can rise and fall over 1 m, which is large relative to the ~2.4 m saturated aquifer thickness under baseflow conditions. The simulation results illustrated how the rise of the suboxic groundwater into the vadose zone resulted in a small fraction of the submerged pore space being occupied by entrapped gas. The entrapped gas initially contains atmospheric levels of oxygen. The oxygen in the entrapped gas partitions to the liquid phase based on Henry's Law leading to dissolved gas concentrations 8-9 mg/L in the newly saturated zone above the previous water table. As the water table continues to rise, this zone of enhanced dissolved oxygen increases vertically while the bulk of the original saturated zone remains low in dissolved oxygen. As the water table falls in the summer, enhanced dissolved oxygen descends into the top of the original saturated zone. For a given site, the magnitude of enhanced oxygenation due to changes in water table elevation will depend on many factors. These include sediment texture, vadose zone soil gas composition, and the magnitude, frequency, and duration of water table fluctuations. Some concerns of the elevated oxygen near the water table include 1) the possible reoxidation and remobilization of reduced uranium, 2) loss of treatment capacity precisely where elevated groundwater uranium concentrations are commonly found (i.e., near the water table), 3) the need for additional electron donor to achieve anaerobic conditions, and 4) key microorganisms during bioremediation are not very tolerant of high oxygen levels.

### 5.2.3 Flood Events

Seasonal and episodic flood events can be an issue for uranium bioremediation in shallow alluvial aquifers. If recharge from surface flooding is sufficiently high, the deployment and efficacy of *in situ* uranium bioremediation could be disrupted. To examine the impact of such events, we simulated a flood at the Rifle IFRC site by ponding 0.3 m of Colorado River water for 1 week over a 20 m wide section of the site. For the Rifle sediments, this boundary condition introduced a large volume of water that saturated the vadose zone beneath the ponded floodwater and displaced most of the saturated zone pore volume in the 70 m long domain in just a few days. The displacement of U(VI)-bearing porewaters and the introduction of low alkalinity river water, which significantly enhanced uranium adsorption, temporarily resulted in locally lower U(VI) concentrations. Since the bulk of uranium is associated with the solid phases under these geochemical conditions, U(VI) concentrations eventually rebounded as re-equilibration with solid phase uranium and ambient water chemistry occurred. During flood conditions, a mound of groundwater fed by the high recharge increased the saturated thickness, and significantly altered the groundwater flow magnitude and direction. If biostimulation began on the first day of the flood, as was simulated in one scenario, the delivery of acetate was driven downward and upgradient away from the intended treatment zone.

Another complication from flooding is the potential for oxygen- and/or nitrate-laden water to enter the saturated zone. While the general issue is similar to the enhanced oxygenation of groundwater induced by water table fluctuation and gas entrapment, the magnitude and extent is much larger. After 7 days of flood conditions, simulated dissolved oxygen levels, approximating equilibrium with atmospheric oxygen, were present throughout the saturated zone. After the ponded boundary condition was removed, these oxygen levels persisted, even though the regional groundwater flow field was quickly re-established. A scenario where acetate biostimulation was begun 1 day after the ponded boundary condition was removed, illustrated that flow and transport were very similar to the baseline condition, indicating a rapid recovery of the hydrologic system to pre-flood conditions. Similar to the one-dimensional simulations, the additional oxygen in the system led to slight increases in acetate consumption, and minor decreases in rates of microbial reduction of U(VI) and other terminal electron acceptors. In general, the simulated bioreduction of oxygen via acetate biostimulation was able to locally create suboxic conditions, albeit with a front that moved downgradient slower than advection by groundwater. This was due to limitations imposed by the injected acetate mass and reaction kinetics. With the engineered oxygen bioreduction and the influx of the ambient suboxic groundwater at the upgradient boundary, the saturated aquifer was restored to suboxic conditions in about 100 days. There was also a small but noticeable depth-dependent distribution of TEAP reaction products near the top of the water table aquifer due to the presence of dissolved oxygen near the top of the increased-thickness saturated zone.

For the conditions assumed, the flood-induced presence of highly oxygenated groundwater did not have a large overall impact on the subsequent biostimulation of the aquifer. Based on the earlier analysis, floodwaters with 8 mg/L nitrate would have even less of an impact. If, however,

the flood event followed the biostimulation, it is possible that the oxygenated water could reoxidize and remobilize bioreduced uranium. While there have been laboratory studies that have identified such behaviors (Abdelouas et al., 1999; Komlos et al., 2007), these conditions have not been replicated in the field. The post-biostimulation oxidation of bioreduced phases in the Rifle aquifer is the subject of ongoing investigation ranging from microorganisms that oxidize FeS while reducing oxygen, to kinetically-limited uraninite oxidation and dissolution.

## 5.3 Closing Comments and Next Steps for Reactive Transport Modeling of Uranium Bioremediation

The value of modeling presented here lies not so much in its predictive ability, although that is important, but in the integration of processes in such a way that process interactions can be understood. Ideally, this will make it possible to avoid unintended consequences of a particular bioremediation design. In the past, there has been reticence to use numerical models for newly developed *in situ* remediation approaches largely to avoid contention about the model itself. However, the use of such models to gain insight into bioremediation is crucial to the assessment of likely uranium bioremediation outcomes. We have provided a modeling framework that successfully links the dominant processes and provides an overall picture of parameter sensitivities.

However, further model development is needed, especially for additional parameters and processes controlling long-term behavior of a bioremediated uranium plume. Specific areas for improvement include:

- Slow-release amendments (including a range of alternate electron donors)
- Reoxidation rates for reduced phases (including uraninite)
- Post-biostimulation sorption by *Mollicutes* or other microbes living on dead biomass
- Rate-limited process controls on long-term uranium immobilization

Long-term predictions based on numerical models are inherently uncertain. Reduction of uncertainty in these areas will help to reduce overall model uncertainty. Ultimately, long-term predictions will be tested by long-term monitoring of actual bioremediation projects, enabling further model improvement.

The future experimental research and numerical modeling being carried out at the Rifle IFRC site and other uranium-contaminated aquifers will add to the pool of data available for future development of these models and will increase the process accuracy of these tools. In the future, combined microbial and abiotic geochemical processes will likely be built in to reactive transport models with baseline data for a wide range of electron donors and initial microbial community

compositions. Fundamental rate data controlling reoxidation of U(IV) will also be included, enabling accurate assessment of long-term behavior of bioreduced alluvial aquifers.

# 6 References


Abdelouas, A., Lutze, W. and Nuttall, H.E., 1999. Oxidative dissolution of uraninite precipitated on Navajo sandstone. Journal of Contaminant Hydrology, 36(3-4): 353-375.

Akob, D.M. et al., 2008. Functional diversity and electron donor dependence of microbial populations capable of U(VI) reduction in radionuclide-contaminated subsurface sediments. Applied and Environmental Microbiology, 74(10): 3159-3170.

Anderson, R.T. et al., 2003. Stimulating the in situ activity of Geobacter species to remove uranium from the groundwater of a uranium-contaminated aquifer. Applied and Environmental Microbiology, 69(10): 5884-5891.

Bargar, J. et al., 2009a. Mechanisms of Biogenic Uraninite Corrosion in Groundwater at the Rifle IFRC site, Abstract H33L-07., AGU, Fall Meet. . Eos Trans., San Francisco, CA.

Bargar, J.R., Bernier-Latmani, R., Giammar, D.E. and Tebo, B.M., 2008. Biogenic Uraninite Nanoparticles and Their Importance for Uranium Remediation. Elements, 4(6): 407-412.

Bargar, J.R. et al., 2009b. Corrosion of Biogenic Uraninite: Molecular- and Intermediate-scale Measurements, Paper No. 64-8, Geological Society of America GSA Annual Meeting GSA Abstracts with Programs Portland, OR.

Bear, J. and Bahmat, Y., 1991. Introduction to Modeling of Transport Phenomena in Porous Meda. Theory and Applications of Transport in Porous Media, 4. Kluwer Academic Publishers, Dordrecht, The Netherlands.

Bernhard, G. et al., 2001. Uranyl(VI) carbonate complex formation: Validation of the Ca2UO2(CO3)(3)(aq.) species. Radiochimica Acta, 89(8): 511-518.

Boonchayaanant, B., Gu, B., Wang, W., Ortiz, M.E. and Criddle, C.S., 2009. Can microbially-generated hydrogen sulfide account for the rates of U(VI) reduction by a sulfate-reducing bacterium? Biodegradation, 21(1): 81-95.

Brooks, R.H. and Corey, A.T., 1966. Properties of porous media affecting fluid flow. Proc. ASCE Journal of Irrigation and Drainage Division, 93(2): 61-88.

Brooks, S.C. et al., 2003. Inhihition of bacterial U(VI) reduction by calcium. Environmental Science & Technology, 37(9): 1850-1858.

Canfield, D.E., 1989. Reactive Iron in Marine-Sediments. Geochimica Et Cosmochimica Acta, 53(3): 619-632.

Choi, J. and Park, J.W., 2005. Competitive adsorption of heavy metals and uranium on soil constituents and microorganism. Geosciences Journal, 9(1): 53-61.

Curtis, G.P., Fox, P., Kohler, M. and Davis, J.A., 2004. Comparison of in situ uranium K-D values with a laboratory determined surface complexation model. Applied Geochemistry, 19(10): 1643-1653.

Davis, J.A., Coston, J.A., Kent, D.B. and Fuller, C.C., 1998. Application of the surface complexation concept to complex mineral assemblages. Environmental Science & Technology, 32(19): 2820-2828.

Davis, J.A. et al., 2006. Processes affecting transport of uranium in a suboxic aquifer. Physics and Chemistry of the Earth, 31(10-14): 548-555.

Davis, J.A. and Kent, D.B., 1990. Surface Complexation Modeling in Aqueous Geochemistry. Reviews in Mineralogy, 23: 177-260.

Davis, J.A., Meece, D.E., Kohler, M. and Curtis, G.P., 2004. Approaches to surface complexation modeling of uranium(VI) adsorption on aquifer sediments. Geochimica Et Cosmochimica Acta, 68(18): 3621-3641.

DOE, 1999. Final site observational work plan for the UMTRA project Old Rifle site GJO-99-88-TAR, Grand Junction, Colo.

Englert, A., Hubbard, S.S., Williams, K.H., Li, L. and Steefel, C.I., 2009. Feedbacks Between Hydrological Heterogeneity and Bioremediation Induced Biogeochemical Transformations. Environmental Science & Technology, 43(14): 5197-5204.

EPA, 1998. U.S. Environmental Protection Agency Soil Cleanup Criteria in 40 CFR Part 192.

EPA, 2000. U.S. Environmental Protection Agency National Primary Drinking Water Regulations; Radionuclides; Final Rule in 40 CFR Parts 9, 141, and 142

Fang, Y., Yabusaki, S.B., Morrison, S.J., Amonette, J.P. and Long, P.E., 2009. Multicomponent reactive transport modeling of uranium bioremediation field experiments. Geochimica Et Cosmochimica Acta, 73(20): 6029-6051.

Finneran, K.T., Anderson, R.T., Nevin, K.P. and Lovley, D.R., 2002. Potential for Bioremediation of uranium-contaminated aquifers with microbial U(VI) reduction. Soil & Sediment Contamination, 11(3): 339-357.

Fox, P.M., Davis, J.A. and Zachara, J.M., 2006. The effect of calcium on aqueous uranium(VI) speciation and adsorption to ferrihydrite and quartz. Geochimica Et Cosmochimica Acta, 70(6): 1379-1387.

Gorby, Y.A. and Lovley, D.R., 1992. Enzymatic Uranium Precipitation. Environmental Science & Technology, 26(1): 205-207.

Guillaumont, R. et al., 2003. Chemical Thermodynamics 5. Update on the Chemical Thermodynamics of Uranium, Neptunium, Plutonium, Americium, and Technetium. Nuclear Energy Agency. Elsevier, Amsterdam.

Holmes, D.E., Finneran, K.T., O'Neil, R.A. and Lovley, D.R., 2002. Enrichment of members of the family Geobacteraceae associated with stimulation of dissimilatory metal reduction in uranium-contaminated aquifer sediments. Applied and Environmental Microbiology, 68(5): 2300-2306.

Hunter, K.S., Wang, Y.F. and Van Cappellen, P., 1998. Kinetic modeling of microbially-driven redox chemistry of subsurface environments: coupling transport, microbial metabolism and geochemistry. Journal of Hydrology, 209(1-4): 53-80.

Hyndman, D.W. et al., 2000. Hydraulic characterization and design of a full-scale biocurtain. Ground Water, 38(3): 462-474.

Istok, J.D. et al., 2004. In situ bioreduction of technetium and uranium in a nitrate-contaminated aquifer. Environmental Science & Technology, 38(2): 468-475.

Jeon, B.H., Dempsey, B.A., Burgos, W.D., Barnett, M.O. and Roden, E.E., 2005. Chemical reduction of U(VI) by Fe(II) at the solid-water interface using natural and synthetic Fe(III) oxides. Environmental Science & Technology, 39(15): 5642-5649.

Kaluarachchi, J.J. and Parker, J.C., 1992. Multiphase flow with a simplified model for oil entrapment. Transport in Porous Media, 7(1): 1-14.

Komlos, J., Kukkadapu, R.K., Zachara, J.M. and Jaffe, P.R., 2007. Biostimulation of iron reduction and subsequent oxidation of sediment containing Fe-silicates and Fe-oxides: Effect of redox cycling on Fe(III) bioreduction. Water Research, 41(13): 2996-3004.

Komlos, J., Mishra, B., Lanzirotti, A., Myneni, S.C.B. and Jaffe, P.R., 2008a. Real-time speciation of uranium during active bioremediation and U(IV) reoxidation. Journal of Environmental Engineering-Asce, 134(2): 78-86.

Komlos, J., Peacock, A., Kukkadapu, R.K. and Jaffe, P.R., 2008b. Long-term dynamics of uranium reduction/reoxidation under low sulfate conditions. Geochimica Et Cosmochimica Acta, 72(15): 3603-3615.

Land, C.S., 1968. Calculation of imbibition relative permeability for two and three-phase flow from rock properties. Society of Petroleum Engineers Journal, 8(2): 149-&.

Li, L., Steefel, C.I., Williams, K.H., Wilkins, M.J. and Hubbard, S.S., 2009. Mineral Transformation and Biomass Accumulation Associated With Uranium Bioremediation at Rifle, Colorado. Environmental Science & Technology, 43(14): 5429-5435.

Liger, E., Charlet, L. and Van Cappellen, P., 1999. Surface catalysis of uranium(VI) reduction by iron(II). Geochimica Et Cosmochimica Acta, 63(19-20): 2939-2955.

Liu, C.X., Kota, S., Zachara, J.M., Fredrickson, J.K. and Brinkman, C.K., 2001. Kinetic analysis of the bacterial reduction of goethite. Environmental Science & Technology, 35(12): 2482-2490.

Long, P.E., Yabusaki, S.B., Meyer, P.D., Murray, C.J. and N'Guessan, A.L., 2008. Technical Basis for Assessing Uranium Bioremediation Performance. NUREG/CR-6973, U.S. Nuclear Regulatory Commission.

Lovley, D.R., Phillips, E.J.P., Gorby, Y.A. and Landa, E.R., 1991. Microbial Reduction of Uranium. Abstracts of Papers of the American Chemical Society, 202: 8-Geoc.

Lovley, D.R., Roden, E.E., Phillips, E.J.P. and Woodward, J.C., 1993. Enzymatic Iron and Uranium Reduction by Sulfate-Reducing Bacteria. Marine Geology, 113(1-2): 41-53.

Madden, A.S. et al., 2009. Donor-dependent Extent of Uranium Reduction for Bioremediation of Contaminated Sediment Microcosms. Journal of Environmental Quality, 38(1): 53-60.

Mahadevan, R. et al., 2006. Characterization of metabolism in the Fe(III)-reducing organism Geobacter sulfurreducens by constraint-based modeling. Applied and Environmental Microbiology, 72(2): 1558-1568.

Moon, H.S., Komlos, J. and Jaffe, P.R., 2007. Uranium reoxidation in previously bioreduced sediment by dissolved oxygen and nitrate. Environmental Science & Technology, 41(13): 4587-4592.

Moon, H.S., Komlos, J. and Jaffé, P.R., 2009. Biogenic U(IV) oxidation by dissolved oxygen and nitrate in sediment after prolonged U(VI)/Fe(III)/SO42- reduction. Journal of Contaminant Hydrology, 105(1-2): 18-27.

Moyes, L.N. et al., 2000. Uranium uptake from aqueous solution by interaction with goethite, lepidocrocite, muscovite, and mackinawite: An X-ray absorption spectroscopy study. Environmental Science & Technology, 34(6): 1062-1068.

N'Guessan, A.L., Vrionis, H.A., Resch, C.T., Long, P.E. and Lovley, D.R., 2008. Sustained removal of uranium from contaminated groundwater following stimulation of dissimilatory metal reduction. Environmental Science & Technology, 42(8): 2999-3004.

Ortiz-Bernad, I., Anderson, R.T., Vrionis, H.A. and Lovley, D.R., 2004. Resistance of solid-phase U(VI) to microbial reduction during in situ bioremediation of uranium-contaminated groundwater. Applied and Environmental Microbiology, 70(12): 7558-7560.

Pabalan, R.T., Bertetti, F.P., Prikryl, J.D. and Turner, D.R., 1996. Uranium(VI) sorption onto selected mineral surfaces: Key geochemical parameters. Abstracts of Papers of the American Chemical Society, 211: 55-Geoc.

Pyzik, A.J. and Sommer, S.E., 1981. Sedimentary Iron Monosulfides - Kinetics and Mechanism of Formation. Geochimica Et Cosmochimica Acta, 45(5): 687-698.

Regenspurg, S., Schild, D., Schafer, T., Huber, F. and Malmstrom, M.E., 2009. Removal of uranium(VI) from the aqueous phase by iron(II) minerals in presence of bicarbonate. Applied Geochemistry, 24(9): 1617-1625.

Riley, R.G. and Zachara, J.M., 1992. Chemical contaminants on DOE lands and selection of contaminant mixtures for subsurface research. DOE/ER-0547T, U.S. Department of Energy, Washington, D.C.

Rittmann, B.E. and McCarty, P.L., 2001. Environmental biotechnology : principles and applications. McGraw-Hill series in water resources and environmental engineering. McGraw-Hill, Boston, xiv, 754 p. pp.

Roden, E.E. and Zachara, J.M., 1996. Microbial reduction of crystalline iron(III) oxides: Influence of oxide surface area and potential for cell growth. Environmental Science & Technology, 30(5): 1618-1628.

Sani, R.K., Peyton, B.M., Dohnalkova, A. and Amonette, J.E., 2005. Reoxidation of reduced uranium with iron(III) (hydr)oxides under sulfate-reducing conditions. Environmental Science & Technology, 39(7): 2059-2066.

Scott, T.B., Allen, G.C., Heard, P.J. and Randell, M.G., 2005. Reduction of U(VI) to U(IV) on the surface of magnetite. Geochimica Et Cosmochimica Acta, 69(24): 5639-5646.

Senko, J.M., Istok, J.D., Suflita, J.M. and Krumholz, L.R., 2002. In-situ evidence for uranium immobilization and remobilization. Environmental Science & Technology, 36(7): 1491-1496.

Shelobolina, E.S., Vrionis, H.A., Findlay, R.H. and Lovley, D.R., 2008. Geobacter uraniireducens sp nov., isolated from subsurface sediment undergoing uranium bioremediation. International Journal of Systematic and Evolutionary Microbiology, 58: 1075-1078.

Suzuki, Y., Kelly, S.D., Kemner, K.M. and Banfield, J.F., 2005. Direct microbial reduction and subsequent preservation of uranium in natural near-surface sediment. Applied and Environmental Microbiology, 71(4): 1790-1797.

Urrutia, M.M., Roden, E.E. and Zachara, J.M., 1999. Influence of aqueous and solid-phase Fe(II) complexants on microbial reduction of crystalline iron(III) oxides. Environmental Science & Technology, 33(22): 4022-4028.

Vrionis, H.A. et al., 2005. Microbiological and geochemical heterogeneity in an in situ uranium bioremediation field site. Applied and Environmental Microbiology, 71(10): 6308-6318.

Waite, T.D., Davis, J.A., Fenton, B.R. and Payne, T.E., 2000. Approaches to modelling uranium(VI) adsorption on natural mineral assemblages. Radiochimica Acta, 88(9-11): 687-693.

Wan, J.M. et al., 2005. Reoxidation of bioreduced uranium under reducing conditions. Environmental Science & Technology, 39(16): 6162-6169.

Wersin, P. et al., 1994. Interaction between aqueous uranium(VI) and sulfide minerals - spectroscopic evidence for sorption and reduction. Geochimica Et Cosmochimica Acta, 58(13): 2829-2843.

White, M.D. and Oostrom, M., 2006. STOMP Subsurface Transport Over Multiple Phases Version 4.0 User's Guide, PNNL-15782, Pacific Northwest National Laboratory, Richland, Washington.

Wu, W.M. et al., 2006. Pilot-scale in situ bioremedation of uranium in a highly contaminated aquifer. 2. Reduction of U(VI) and geochemical control of U(VI) bioavailability. Environmental Science & Technology, 40(12): 3986-3995.

Yabusaki, S.B. et al., 2007. Uranium Removal from Groundwater via In Situ Biostimulation: Field-Scale Modeling of Transport and Biological Processes. Journal of Contaminant Hydrology, 93(1-4): 216-235.

Yabusaki, S.B., Fang, Y.L. and Waichler, S.R., 2008. Building conceptual models of field-scale uranium reactive transport in a dynamic vadose zone-aquifer-river system. Water Resources Research, 44(12): 24.

Zheng, Z.P., Tokunaga, T.K. and Wan, J.M., 2003. Influence of calcium carbonate on U(VI) sorption to soils. Environmental Science and Technology, 37: 5603-5608.

Zopfi, J., Bttcher, M.E. and Jorgensen, B.B., 2008. Biogeochemistry of sulfur and iron in Thioploca-colonized surface sediments in the upwelling area off central chile. Geochimica Et Cosmochimica Acta, 72(3): 827-843.

# Appendix A

This appendix contains all simulation results for the sensitivity analyses.

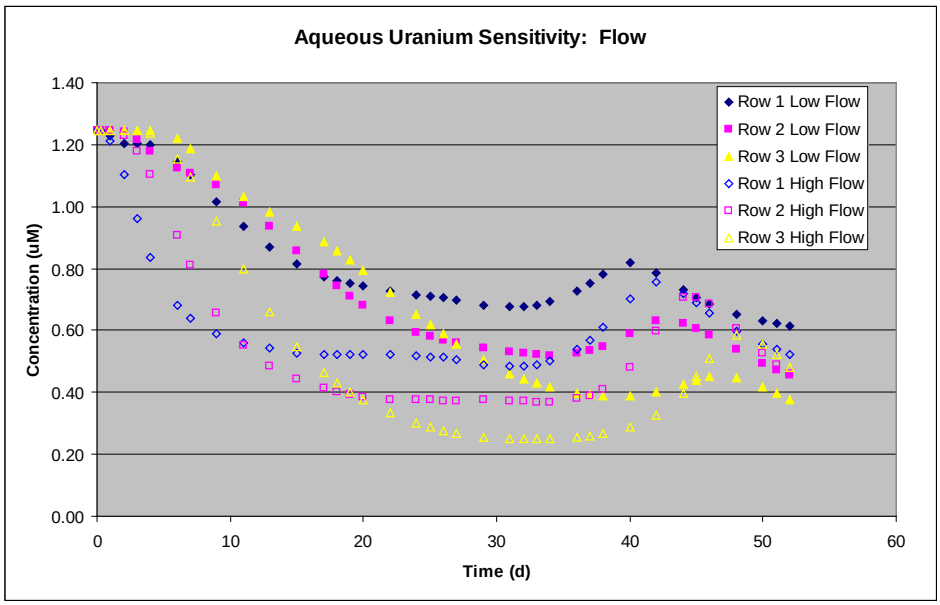


**Figure A.1**. Time-dependent aqueous uranium sensitivity to flow rate at 2.5 m (row 1), 5.0 m (row 2), and 8.5 m (row 3).

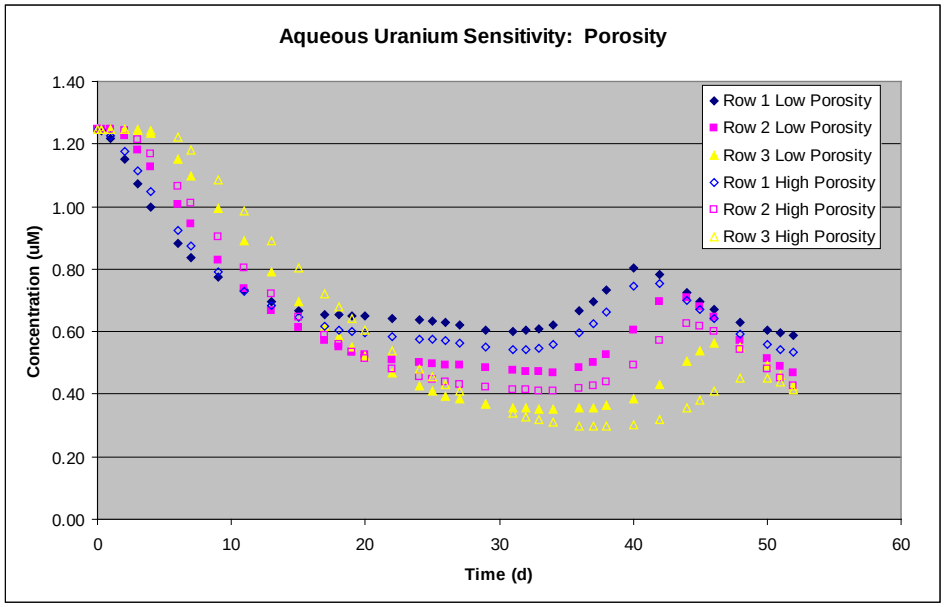


**Figure A.2**. Time-dependent aqueous uranium sensitivity to porosity at 2.5 m (row 1), 5.0 m (row 2), and 8.5 m (row 3).

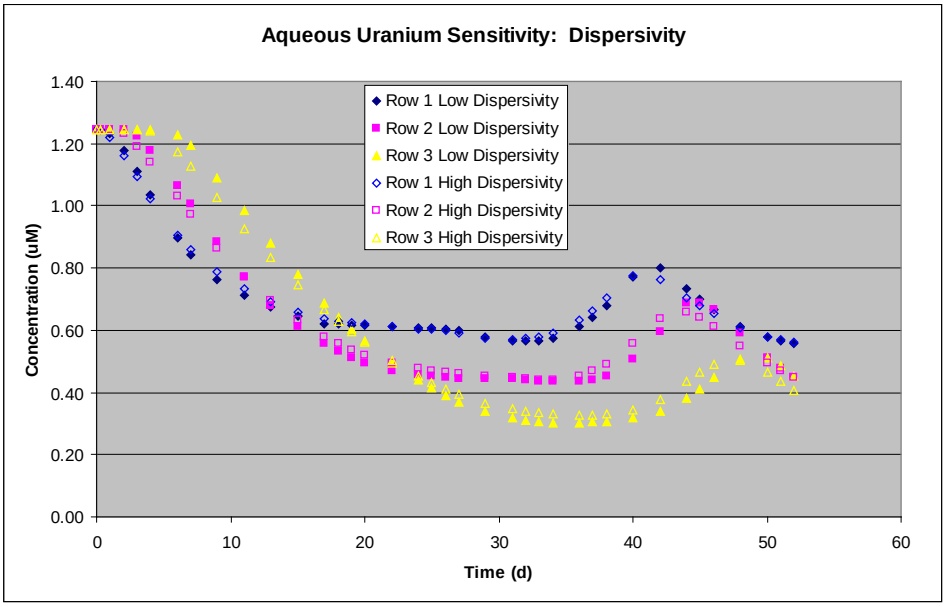


**Figure A.3**. Time-dependent aqueous uranium sensitivity to dispersivity at 2.5 m (row 1), 5.0 m (row 2), and 8.5 m (row 3)

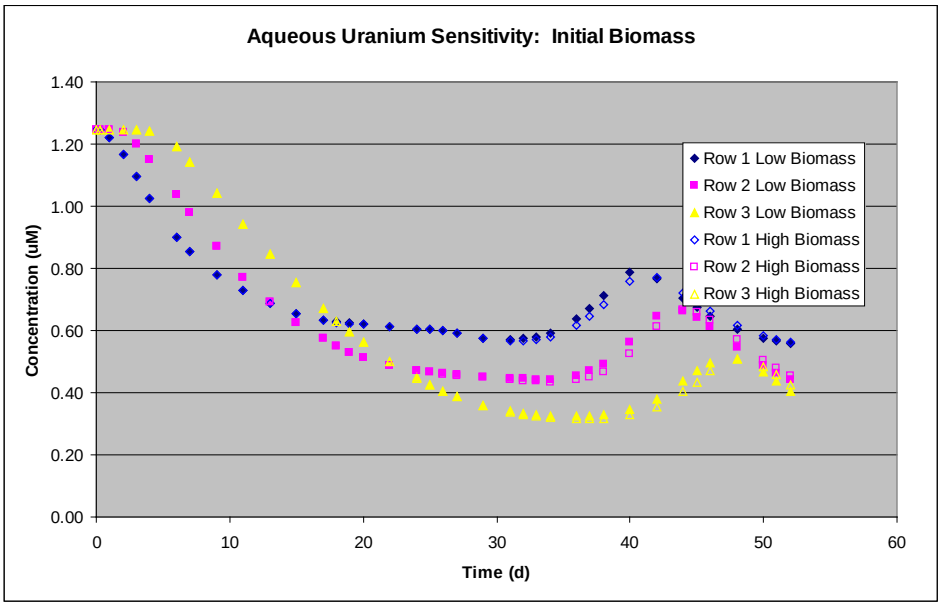


**Figure A.4**. Time-dependent aqueous uranium sensitivity to initial SRB biomass at 2.5 m (row 1), 5.0 m (row 2), and 8.5 m (row 3).

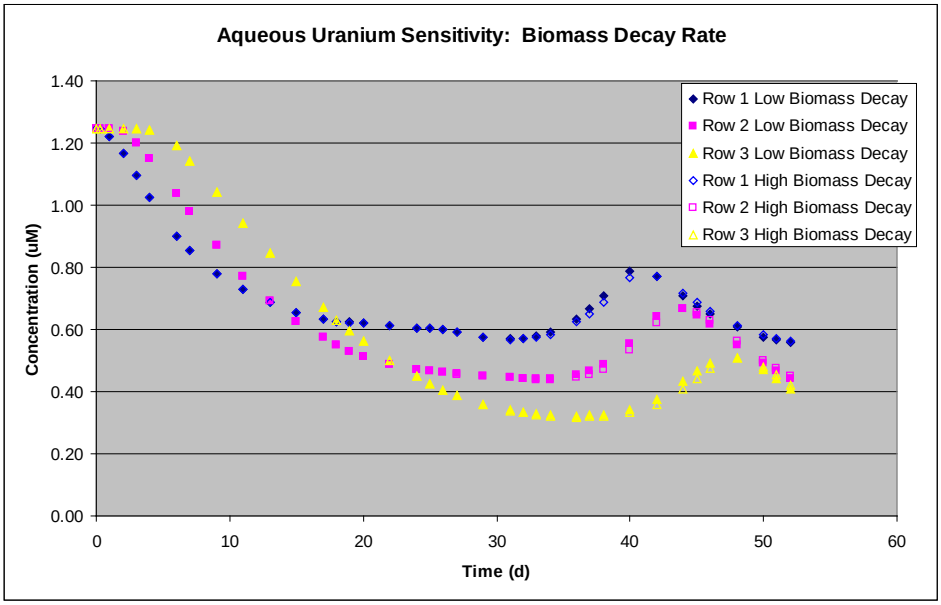


**Figure A.5**. Time-dependent aqueous uranium sensitivity to initial SRB biomass decay at 2.5 m (row 1), 5.0 m (row 2), and 8.5 m (row 3).

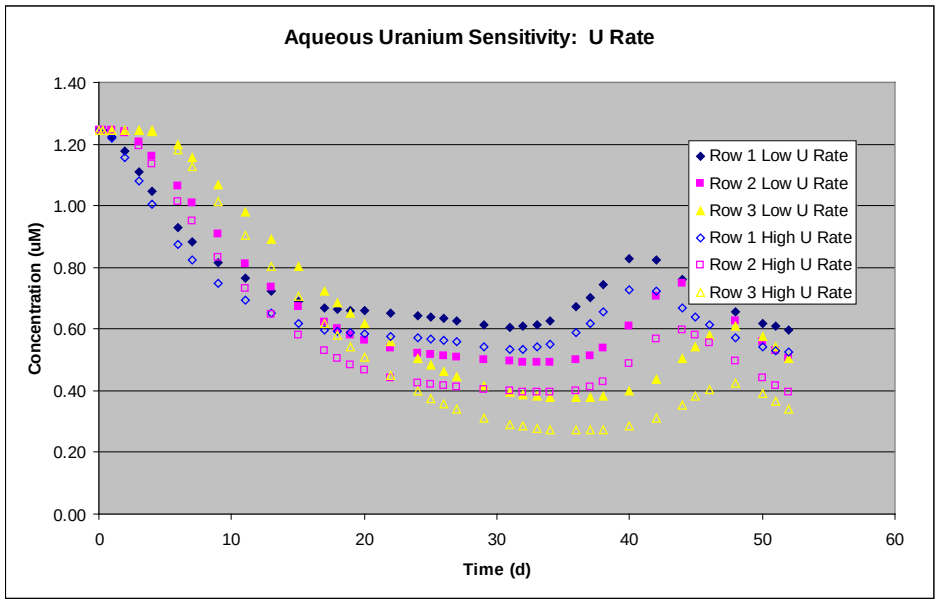


**Figure A.6**. Time-dependent aqueous uranium sensitivity to uranium bioreduction rate at 2.5 m (row 1), 5.0 m (row 2), and 8.5 m (row 3).

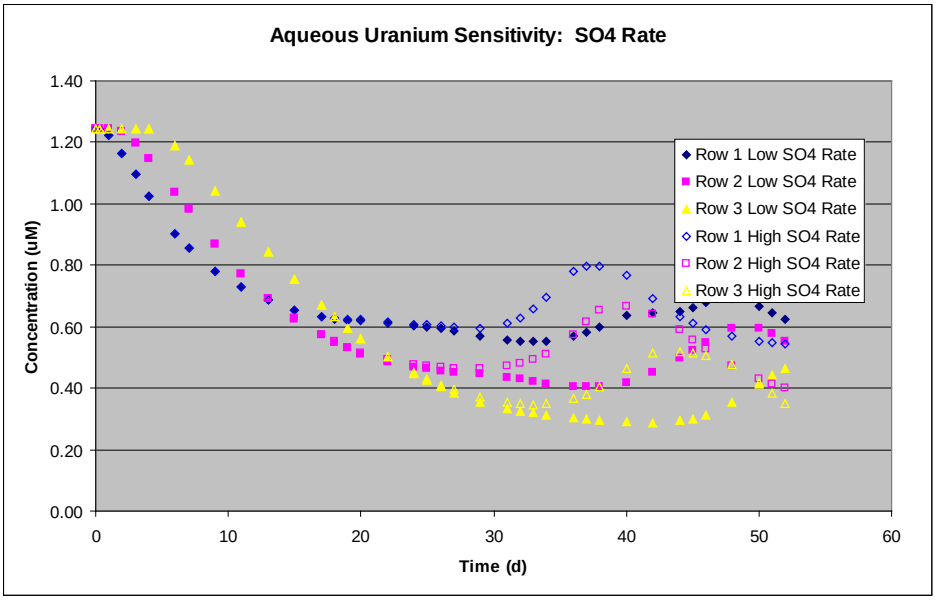


**Figure A.7**. Time-dependent aqueous uranium sensitivity to sulfate bioreduction rate at 2.5 m (row 1), 5.0 m (row 2), and 8.5 m (row 3).

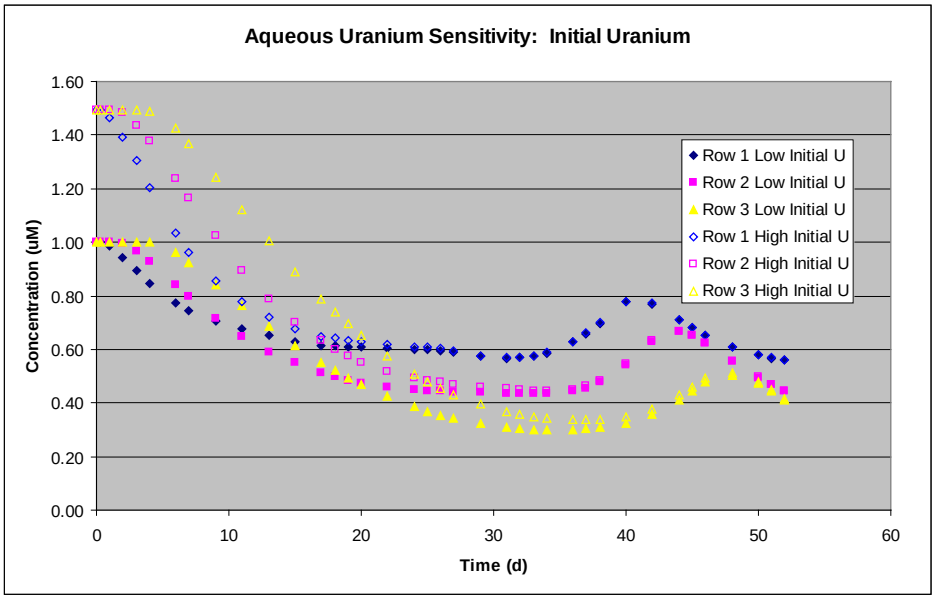


**Figure A.8**. Time-dependent aqueous uranium sensitivity to initial aqueous uranium concentration at 2.5 m (row 1), 5.0 m (row 2), and 8.5 m (row 3).

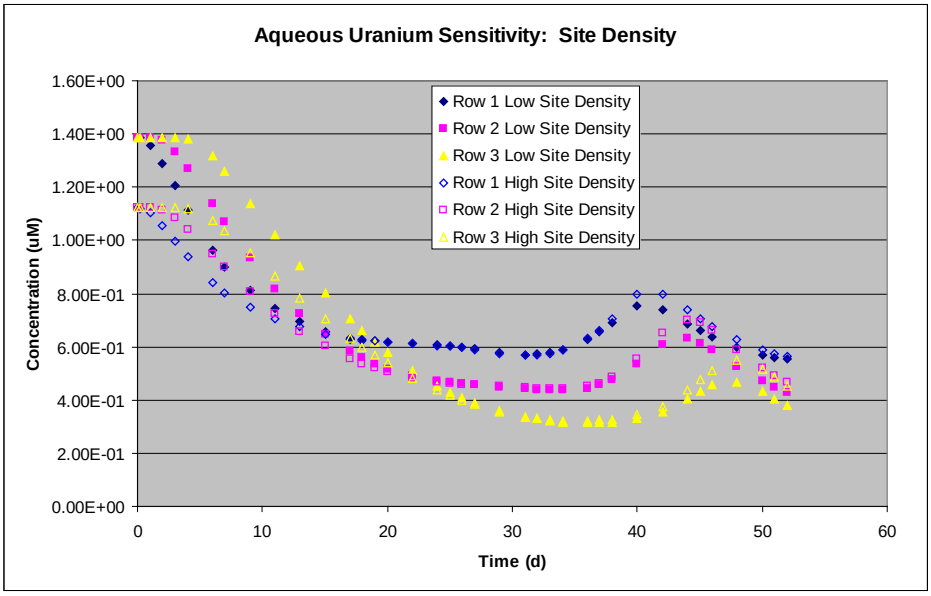


**Figure A.9**. Time-dependent aqueous uranium sensitivity to uranium surface complexation site density at 2.5 m (row 1), 5.0 m (row 2), and 8.5 m (row 3).

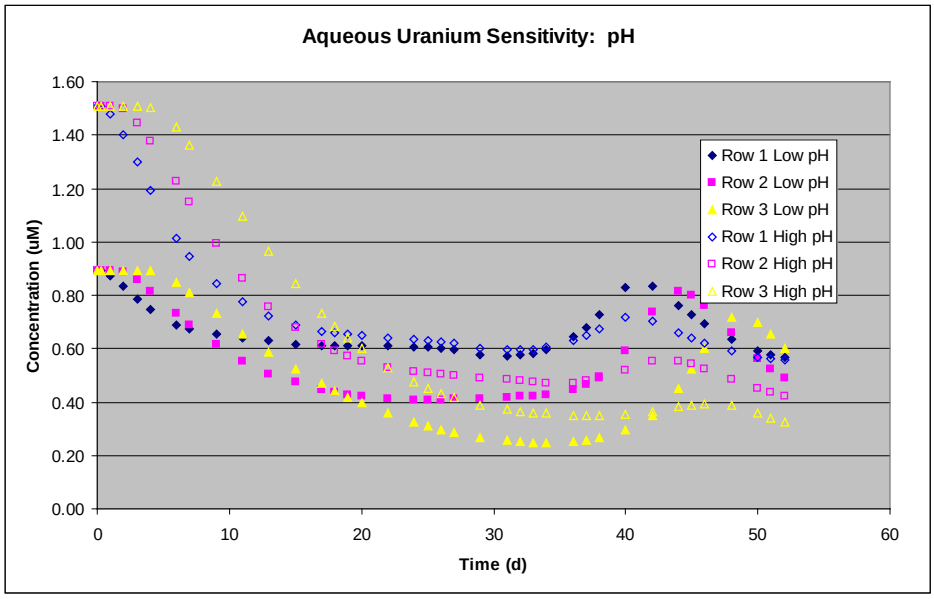


**Figure A.10**. Time-dependent aqueous uranium sensitivity to pH at 2.5 m (row 1), 5.0 m (row 2), and 8.5 m (row 3).